INTERNATIONAL JOURNAL OF TRANSPORTATION RESEARCH & TECHNOLOGY

Volume 1, Issue 1

December 2024

transporttech.org

NATIONAL AVIATION ACADEMY

e-ISSN: 3079-6075

National Aviation Academy

International Journal of Transportation Research and Technology

e-ISSN: 3079-6075

DOI: 10.71108/transporttech.vm01is01

Publisher: National Aviation Academy (NAA)
Licence holder: Academician Arif Pashayev (Rector, NAA)
Address: Baku, Mardakan ave., 30, AZ1045, Azerbaijan
TransportTech is published with the contribution of “National Aviation Academy”
Web: https://transporttech.org
Submission: OJS-TransportTech
e-mail: transporttech@naa.edu.az

Editorial Board

Editorial Office

Journal Secretary
Gulgun Garibli
National Aviation Academy, Azerbaijan
gulgun.garibli@naa.edu.az

Layout Editor
Gulgun Garibli
National Aviation Academy, Azerbaijan
gulgun.garibli@naa.edu.az

Proof Editor
Gunel Valiyeva
National Aviation Academy, Azerbaijan
gvaliyeva@naa.edu.az

Production Editor
Gulgun Garibli
National Aviation Academy, Azerbaijan
gulgun.garibli@naa.edu.az

Technical Editor
Aida Tagiyeva
National Aviation Academy, Azerbaijan
atagiyeva@naa.edu.az

Contents

Research Articles

National Aviation Academy

International Journal of Transportation Research and Technology

e-ISSN: 3079-6075

DOI: 10.71108/transporttech.vm01is01.01

Research Article

Multifaceted Euclidean Manipulators of Spacecraft Docking System

Rasim Alizade, Kanan Azimov*, Javad Samadzade

National Aviation Academy, Baku, Azerbaijan

Timescale of article

Received: 02 September 2024
Accepted: 05 November 2024
Published: 03 December 2024

Corresponding author

Kanan Azimov
konon145@mail.ru

Keywords

Spacecraft docking system; Euclidean manipulators; Structural synthesis; Constructive synthesis; Mobility; Docking unit, Degrees of Freedom, Revolute joint, Sphere in cylindrical slot

Cite this article as:

Alizade, R., Azimov, K. & Samadzade, J. (2024). Multifaceted Euclidean Manipulators of Spacecraft Docking System. *International Journal of Transportation Research and Technology*, 1(1), 5-16.
DOI: 10.71108/transporttech.vm01is01.01

Abstract

The new spacecraft docking system with new Euclidean support-guide legs provide free relative motion of spacecraft and its docking unit are proposed. For the first time, Euclidean hexagonal and octagonal manipulators of docking system are applied. Structural and constructive synthesis of hexagonal and octagonal Euclidean parallel robot manipulators of spacecraft docking system are described. Information on previously and currently used manipulators of docking system and station is presented. Manipulators of these type include “pin-cone” type manipulators and androgynous peripheral manipulators. Systems of links for new Euclidean interface manipulators of docking system and station is designed by using graph theory and theory of structural synthesis.

1. Introduction

In scientific literature there are various descriptions of cylindrical parallel mechanisms of extension, retraction and motion of spacecraft docking system (Syromyatnikov, 1984). The first spacecraft docking devices were pin-cone type devices. The transition of astronauts from one spacecraft to another is made through open space. Devices of 'pin-cone' type carried out precise connection of spars between two spacecraft, and also carried out multiple docking and undocking of spacecraft (Afanasyev, 2003).

The docking process began with the bar head hitting the receiving cone, into which the pin of the docking mechanism entered, which in turn entered to the guide pin holes. Once the bar head entered the receiving cone, the latches went into the slots and clamped down. In the event of a successful coupling, the docking mechanism drive was engaged to tighten and levelling was carried out by a lever mechanism. During undocking, the bar was extended and held in the forward position, springs of the shock absorber were compressed and under the action of springs, the bar head moved forward and separated the spacecraft (Golubev & Yaskevich, 2020; Syromyatnikov, n.d.; Yaskevich, 2007).

In a subsequent device on the principle of 'pin-cone' was to ensure the tightness of the tunnel by means of locks of rigid connection and transition of astronauts through it. These mechanisms were not only androgynous, but could also perform androgynous coupling, which later became the basis for the creation of androgynous peripheral units. The docking process started with coupling and then the actuator of the docking spar locks was engaged. With the closing of the spar locks, the docking mechanism rod unhooking process took place. The docking mechanism actuator allowed the latches to tip forward under spring action, and pulled the head out of guide pin hole and retracted the bar. During undocking, spring pushers were used to disengage the spar joint (Bolotnik & Shmatkov, 2007; Efimenko, 1984; Akimenko et al., 1975).

Further androgynous-peripheral docking devices were developed, which belonged to the 'androgynous type' devices. Androgynous type of docking mechanism is located at the periphery of the docking spar, for this reason such a docking devices is called a peripheral docking devices. Androgynous-peripheral docking devices consist of two units: active and passive. Docking devices that fulfil the functions of both active and passive units are called androgynous docking devices. The most important reason for creation of docking device of new type was liberation of the central part from a pin and a receiving cone. An important element of this mechanism was a ring with three guide petals. The coupling was carried out by latches when the end faces of the rings of both units were aligned. Then the docking spars were aligned with pins and guide pin holes, and the rigid connection that formed the tunnel was provided by locks with active and passive hooks. Undocking was accomplished by unhooking the latches and pushing back the active unit using springs (Mount & Mikhalkin, 1974; Efimenko, 1995; Yaskevich, 2018).

The next modification of androgynous-peripheral docking devices differed from the previous one in the design of guiding petals. The petals were located not outside but inside the docking ring, which led to a reduction in the internal diameter of the transition tunnel (IDSS, 2016). The use of androgynous-peripheral docking devices freed cosmonauts from the work involved in freeing the transition tunnel from the docking mechanisms ("Androgynous Peripheral Attach System", n.d.).

Kinematic structures with different structural parameters of Euclidean docking robot manipulators with three, four and five legs were described (Alizade, 2019). The other one as hexagonal interface Euclidean manipulators of passive and active docking units were represented (Alizade & Samadzade, 2021). In order to reduce the number of links in the four active planes of the support-guide legs, new octagonal Euclidean interface docking units with joints "sphere in cylindrical slot" are created (Alizade et al., 2022). The main advantage of Euclidean parallel robot manipulators is the usage of 4DoF kinematic pair "sphere in cylindrical slot" and RR pairs in each leg (Alizade et al., 2024, June). Euclidean octagonal parallel robot manipulator has four legs insread of six that is benefit of octagonal manipulator and significantly reduces the weight of the structure (Alizade et al., 2024, May).

Using the Euclidean system instead of Cartesian gives the possibility of modelling four kinematic chains instead of six, which is an important advantage. Using the 4DoF kinematic pair "sphere in cylindrical slot" reduces the number of links, which reduces the weight of the structure.

The capture latch system is improved by adding a new mechanism which allows the latches to release quickly enough in the event of failed coupling that helps to prevent structural damage.

For the first time, the vector spaces R2 and R3 are combined and the new Euclidean hexagonal manipulator with three closed kinematic circuits 5R create flat five-link mechanism is received. The connecting coupler point of

this mechanism is connected to the 4DoF kinematic pair "sphere-in-cylindrical slot".

2. Structural synthesis of Euclidean hexagonal and octagonal parallel manipulators

Let the octagonal junction generates the motion (RRRPPP) in space with general constraint $d = 0$. Parallel manipulator can be obtained by taking an appropriate structural group ($M = 0$) and adding the reqired number of actuators (M). According to the formula of F. Freudenstain and R.I. Alizade (IDSS, 2016):

$$M = \sum_{i=1}^{j} f_i - \lambda L \tag{1}$$

where: M – mobility of manipulator;
λ – mobility number of independent close loops of manipulator;
L - number of independent loops;
f_i – the DoF of kinematic pairs;
j – the number of joints.

The number of independent loops L is equaled:

$$L = c - B \tag{2}$$

The kinematic chains on moving platform equal:

$$c = c_l + c_b + c_j \tag{3}$$

where c_l –the total number of legs;
c_b –the total number of branches;
c_j –the total number of jointing up of mobile platforms.
Structural groups for Euclidean hexagonal and octagonal parallel manipulators (Fig. 1) have the following form:

1. Hexagonal manipulator

$0 = \sum_{i=1}^{j} f_i - \lambda(c - B)$

$\sum_{i=1}^{j} f_i = \lambda(c - B)$

$\lambda = 6;\ c_l = 6; B = 1$

$\sum_{i=1}^{j} f_i = 6 \cdot (6 - 1)$

$\sum_{i=1}^{j} f_i = 30$

$j_i = \frac{\sum_{i=1}^{j} f_i}{c_l} = \frac{30}{6} = (5, 5, 5, 5, 5, 5)$

2. Octagonal manipulator

$0 = \sum_{i=1}^{j} f_i - \lambda(c - B)$

$\sum_{i=1}^{j} f_i = \lambda(c - B)$

$\lambda = 6;\ c_l = 4; B = 1$

$\sum_{i=1}^{j} f_i = 6 \cdot (4 - 1)$

$\sum_{i=1}^{j} f_i = 18$

$j_i = \frac{\sum_{i=1}^{j} f_i}{c_l} = \frac{18}{4} = (4, 4, 5, 5)$

	Hexagonal	Octagonal
Class	6	4
Type	6	4
Kind	0	0
Order	6	4
	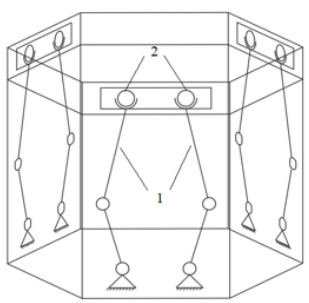	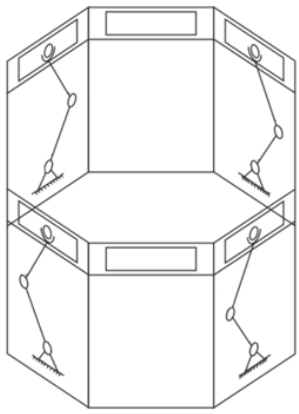

Fig. 1. Structural groups for Euclidean manipulators

Definitions for structural classification:

- Class of a structural group with the single-platforms equal to the number of platform's joints (J_B).
- Type of a structural group expressed by number of joints on each of the mobile platforms (j_B).
- Kind of a structural group expressed by number of branches (c_B) and platforms connection joints (c_j) .
- Order of a structural group expressed by the number of legs (c_l).

3. Structural synthesis of Euclidean interface manipulator

Existing spatial mechanisms move in vector space R3. Consider the new layout of spacecraft and space station docking mechanism by designing Euclidean four legs manipulator in vector space R3. From this point of view, a octagonal manipulator is considered, which support chains (legs) are at four active planes. The support chains (Fig. 2(b)) are represented as flat dyads with two links and two rotating pairs are connected to the octagonal junction by means of 4DoF of kinematic pair "sphere-in-cylindrical slot".

Table 1. New 6DoF parallel robot manipulators of spacecraft

Structural bonding	Illustration						
	Motion of platform	Angle between Euclidean planes	λ_l	c_l	$\sum f_i$	m_p	M
1	2	3	4	5	6	7	8
$\overline{R}\overline{R}-\boxed{S_{ts}S_{ts}S_{ts}}-\overline{R}\overline{R}$ $\overline{R}\overline{R}$	$R_x, R_y, R_z, P_x, P_y, P_z$	120°	6	6	36	6	6
1	2	3	4	5	6	8	9
1	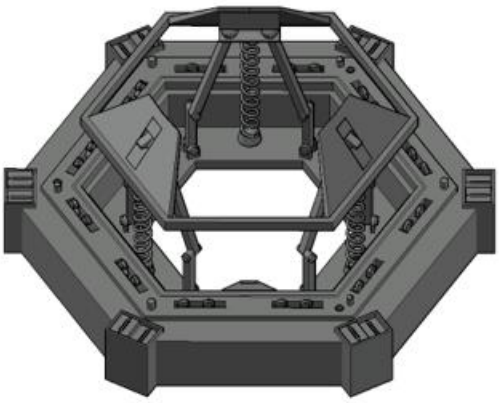						
1	2	3	4	5	6	7	8
$\overline{R}\overline{R}$ $\overline{R}\overline{R}-\boxed{S_{ts}S_{ts}S_{ts}S_{ts}}-\overline{R}\overline{R}$ $R\overline{R}$	$R_x, R_y, R_z, P_x, P_y, P_z$	90°	6	4	24	6	6
2	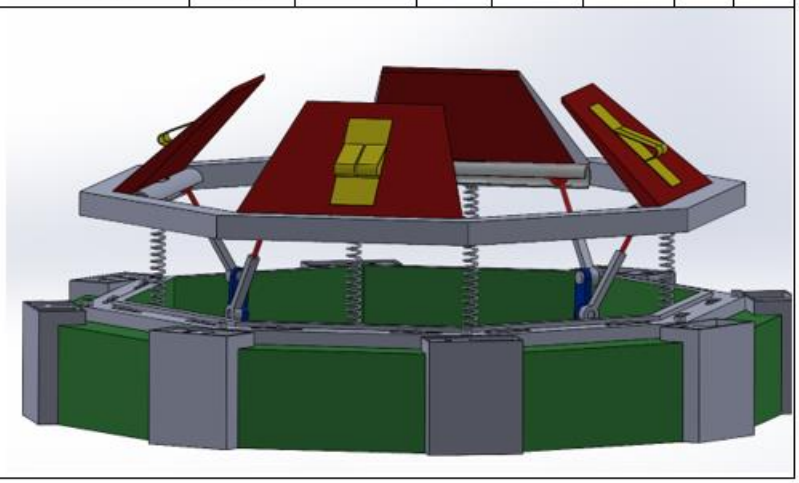						

Using four active faces of the docking unit by means of supporting kinematic chains, a new Euclidean manipulator of the form 4RRScs is obtained (Table 1).

Euclidean docking manipulator with $\lambda = 6;\ L = 3;\ \mathrm{M} = 6\ ;\ c_l = 4$ is represented (Fig. 2(a)).

Using the formula (1) and input data, the mobility of docking manipulator is equal: $6 = \sum_{i=1}^{j} f_i - 6 \cdot 3;\ \sum_{i=1}^{j} f_i = 24.$

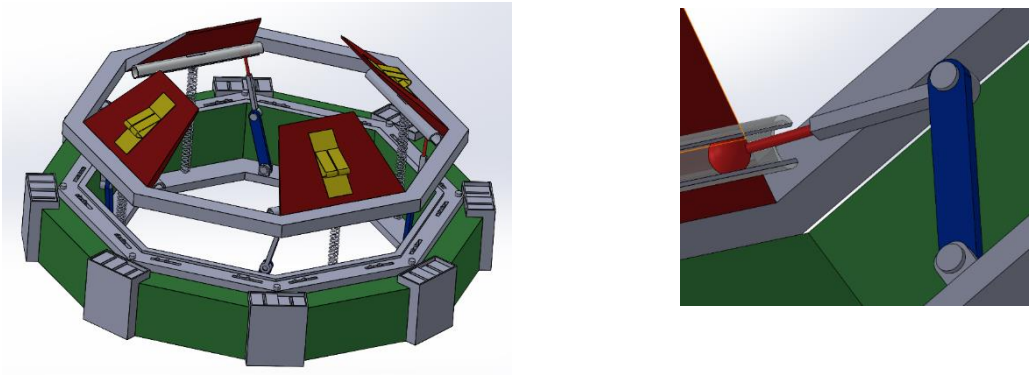

a) Constructive structure b) Constructive leg

Fig. 2. New design of octagonal spacecraft docking manipulator

The advantage is the combination of planar structures with spatial ones is applied. The platform itself, which connects to the space station platform, makes six movements in space, both translational and rotational.

The manipulators developed so far use Cartesian system while the proposed manipulator uses Euclidean system. The manipulators used so far have six legs. The proposed Euclidean hexagonal manipulator also has six legs and the octahedral manipulator has four legs. It is the use of the Euclidean system that makes it possible to model a manipulator with four legs. Despite the reduction of the support chains, the manipulator is able to perform the same movements as the current manipulators. This feature is an advantage of the newly proposed Euclidean spacecraft and station docking manipulators.

4. A hexagonal Euclidean manipulator with the form 3(5R)Scs

The present docking manipulators are controlled by a spatial parallel structure manipulator with six degrees of freedom. All these structures, along with those previously proposed in this paper, are spatial mechanisms that are in vector R3 space. A new modification of the hexagonal Euclidean manipulator for docking spacecraft and stations is proposed, which differs from the previously proposed ones. The difference consists in that here two vector spaces R2 and R3 are combined. By combining of these vector spaces has led to a new design of manipulator of docking system and stations. The proposed manipulator is a hexagonal joint with six degrees of freedom, whose support chains are on three alternating active planes. Legs of the proposed hexagonal Euclidean manipulator are three closed kinematic circuits 5R create flat five-link mechanism with two degrees of freedom M=2, the connecting coupler point of which is connected to the hinge "sphere-in-cylindrical slot". Using three active faces of the docking unit by means of legs, a new Euclidean hexagonal manipulator of the form 3(5R)Scs is obtained (Fig.3).

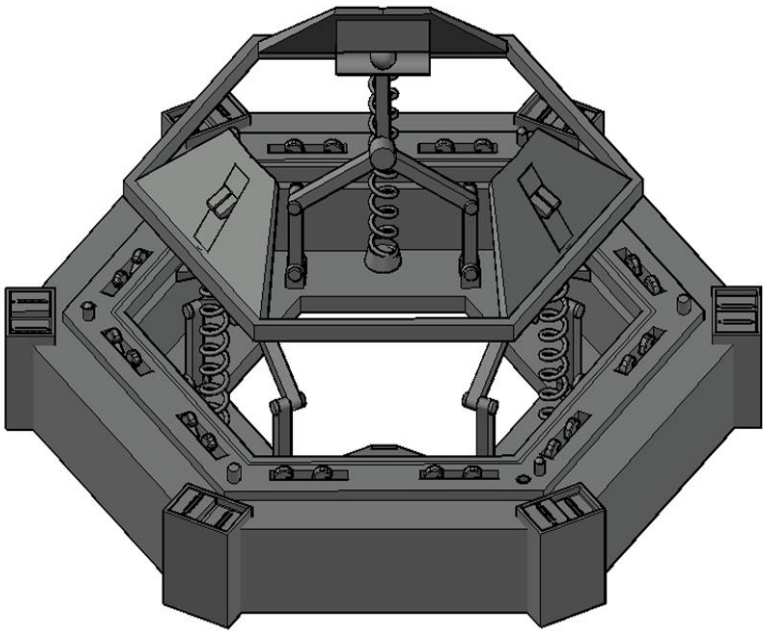

Fig. 3. Design of a hexagonal Euclidean manipulator 3(5R)Scs with six DoF

For the purpose of determining the number of mobility of this manipulator, structural synthesis is performed. This manipulator also differs from previously proposed manipulators in that this one contains mixed independent loops with variable general constraint.

Mobility equation for manipulators which contain mixed independent loops with variable general constraint can be calculated as

$$M = \sum_i^j f_i - \sum_{k=1}^L \lambda_k + q - j_p \tag{4}$$

Where: M – mobility of manipulator;

λ_k – the dimension of the active motion space;

L – the number of independent loops;

f_i – the degree of freedom of kinetic pairs;

j – the number of joints;

q – the excessive over closing constraints;

j_p – the number of passive degree of freedom in kinematic pairs.

The number of independent loops of the hexagonal Euclidean manipulator is five, three of which are in the vector space R2, and the remaining two are in the vector space R3. As a consequence, the dimension of the active motion space is defined as follows

$$\sum_{k=1}^5 \lambda_k = 3 \cdot 3 + 6 \cdot 2 = 21$$

The sum of degree of freedom of kinetic pairs is defined as

$$\sum f_i = 5 \cdot 3 + 4 \cdot 3 = 27$$

Due to the absence of the excessive over closing constraints and the number of passive degree of freedom in kinematic pairs, the mobility of this manipulator is equal

$$M = 27 - 21 - 0 - 0 = 6$$

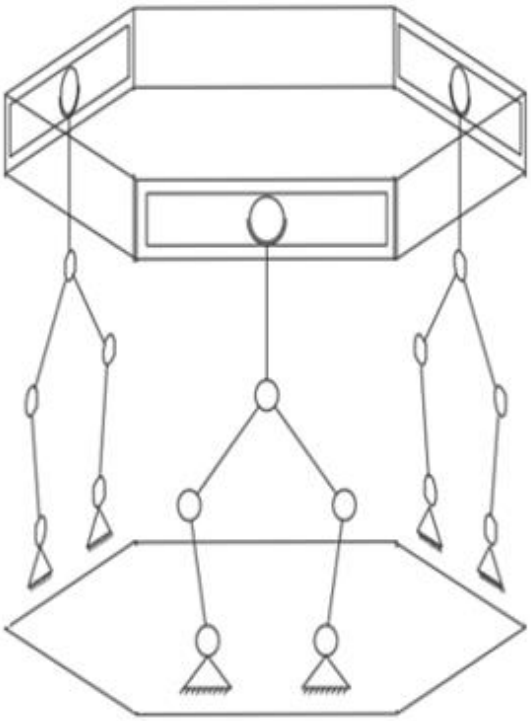

Fig. 4. The structural form of a hexagonal Euclidean manipulator 3(5R)Scs

The structural form of the proposed hexagonal Euclidean manipulator 3(5R)Scs is shown in Fig. 4.

5. Constructive synthesis of Euclidean interface manipulator

Coupling or initial contact is an important part of the docking process. For its implementation, the spacecraft manipulators have a system called the soft capture system.

A soft capture system is a system used during the initial contact between two spacecraft in order to align them. The soft capture system of the hexagonal Euclidean manipulator is a hexagonal joint with three guide petals 5 and three capture latches 1 located on each of them. The soft capture system is used during docking, after the direct approach of the two spacecraft. By means of six legs, the soft capture system extends its full length and is guided directly to the passive manipulator.

The initial contact is made by means of the capture latches entering the corresponding strikers 2 on the passive hexagonal docking system 3. After that, sensors 4 installed in the soft capture system signal that the connection between the spacecraft is held by the latches and it is necessary to start the alignment of the spacecraft. After the completion of the alignment of the two spacecraft, the hard capture system is applied. After successful hard capturing, the capture latches are released and the soft capture system is retracted.

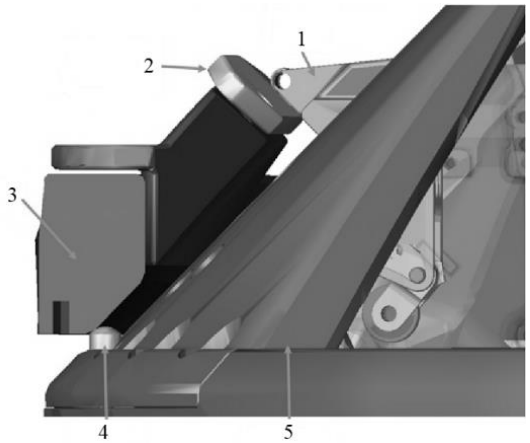

Fig. 5. Capture latch system

Fig. 5 represents such elements as 1 – capture latch; 2 – striker; 3 – passive docking system; 4 – sensor ; 5 – guide petals.

The soft capture system of the hexagonal Euclidean manipulator differs from previous versions. The capture latches in this system are enhanced and have a number of improvements that were not previously available. In the improved version, the latches are capable to release under significantly higher loads, and is also equipped with a mechanism for automatic secondary release, allowing the latches to release quickly enough so that in the event of a failed coupling, the two spacecraft can disengage without damage to the docking mechanisms.

The main elements of the device of capture latch (Fig. 6) are motor 1, latch pawl 3 and automatic secondary release mechanism 4. The latch pawl is used for latching, responsive to the load from the striker 2, located on the passive manipulator to realise the capture of the two docking systems. This mechanism also includes a spring that provides the force required to extend the secondary release mechanism. The lever mechanism system transmits torque from the motor to the latch pawl, thereby holding the catch in the desired position. The principle of operation of the automatic secondary release mechanism is as follows. In a first step, the capture latch is in a position to capture and hold the locking plate located on the passive space docking vehicle. In the event of a failed coupling, the latch is released and releases the striker by means of a motor drive system. A secondary release mechanism allows the striker to be unlocked in the event of failure of the capture latch system. This mechanism is actuated by the actuating mechanism, releasing in turn the spring pusher. When the mechanism is actuated, docking cannot be realised by means of the latches.

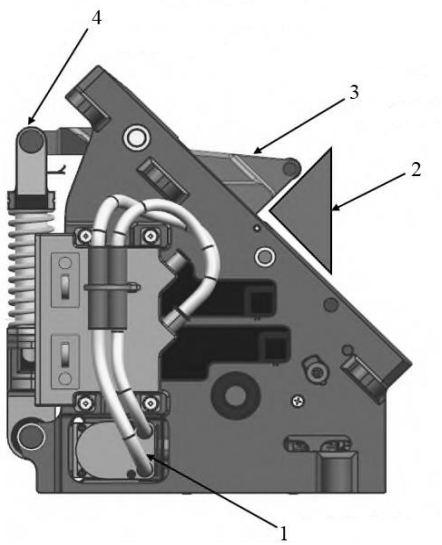

Fig. 6. Device of capture latch

Fig. 6 represents such elements as 1 – motor; 2 – striker; 3 - latch pawl; 4 - automatic secondary release mechanism.

Once the soft capture system is complete, the hard capture system is used to seal and complete the docking process. The hard capture system of a hexagonal Euclidean manipulator includes locks, guide pins, guide pin sockets, and strikers. Each lock includes two hooks, one of which is passive and one of which is active. Two locks are located on each plane of the hexagonal Euclidean manipulator and hence twenty-four hooks are mounted on one docking spar, twelve of which are active and the remaining twelve of which are passive.

When the hard capture systems of the active and passive hexagonal Euclidean manipulator are in close proximity, the locking system is actuated, thereby actuating the hooks. After that, the active hooks engage the passive hooks on the opposite docking manipulator, thereby, along with the sealing, ensuring a tight docking between the two spacecraft. The opening and closing of the hooks by the closed tether is ensured by means of a main motor mounted on one of the locks. In addition to the main motor, there is also an additional motor for redundant opening of the active and passive hooks. The additional cable link has been replaced in this case by pirobolts, due to the large number of gap-sensitive moving parts.

This mechanism has a small number of moving elements and is completely independent of the cable drive. The locks are also fitted with special sensors to monitor hook engagement and tightening. Spar locks must have

sufficient reliability and strength to prevent component failure. To prevent or minimise the risk of possible spontaneous opening and depressurisation of the joint, the locks of the hard capture system shall generate a pre-tightening force that exceeds all external forces as well as internal loads tensile to the joint.

6. Constructive synthesis of Euclidean interface manipulator

The docking of active and passive Euclidean manipulators of spacecraft and station (Fig. 7) is a rather complex process, which consists of several stages. This paper provides a detailed description of these stages.

The initial stage of docking of active and passive Euclidean manipulator of spacecraft and station docking begins directly with their approach. After reaching a certain proximity of the two spacecraft, the speed of the active spacecraft is reduced to a certain level. The active spacecraft then moves along the centre axis towards the passive spacecraft. This continues until the distance between the two spacecraft is sufficient to perform docking.

In a second step, the hexagonal junction 2 of the active hexagonal Euclidean manipulator (Fig. 7(a)) performs what is referred to as a "Lunge", wherein the hexagonal junction 2 approaches and enters the passive manipulator (Fig.7(b)) using the six legs 1 to reproduce the first contact.

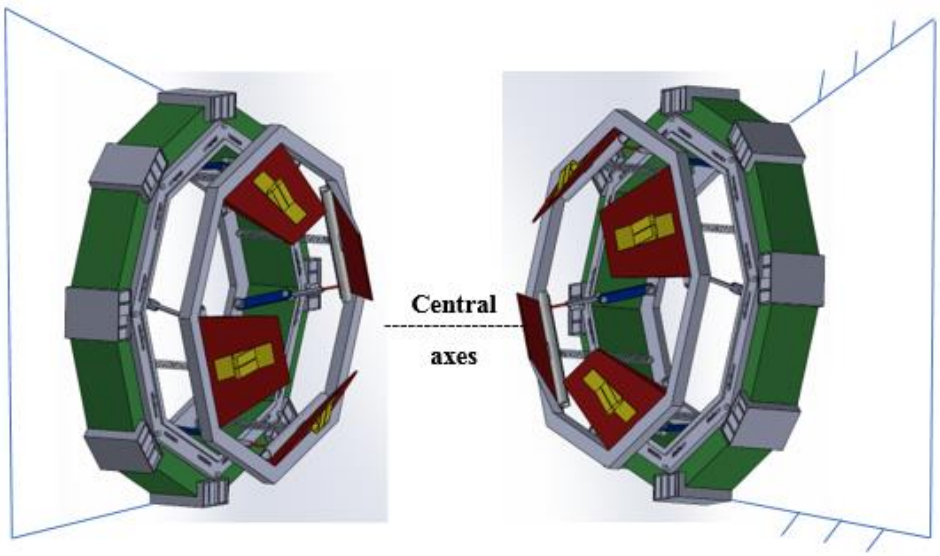

a) Active docking manipulator b) Passive docking manipulator

Fig. 7. Docking of Euclidean manipulators of spacecraft and station docking

The first contact is reproduced by means of the guide petals 3 of the active Euclidean manipulator. If the "Lunge" is successful, the latches 11 which are arranged on the guide petals 3 of the active manipulator extend and strike the mechanical latch striker 8 which is arranged on the passive Euclidean manipulator. In the next stage, the job of the active hexagonal junction 2 now is to attenuate the relative motion between the two vehicles and to align the active and passive hard capture system 10. For this purpose, all six legs 1 of the hexagonal Euclidean manipulator are brought to an equal position for the same length. In this position, the hexagonal junction 2 will be parallel to the hard capture system 10 relative to the centre axis.

These legs 1 then begin to retract to bring the active and passive hard capture systems 10 together, and the guide pins 6 of the active and passive systems enter their corresponding guide pin hole 7, thereby forming tunnels. When the two tunnels are next to each other, a set of twelve structural locks 14 are actuated. Each lock 14 comprises an active and a passive hook, where the active hooks 4 engage the corresponding passive hooks 5 on the opposite unit.

The structural hooks close the remaining gap between the tunnels, compressing the elastomeric seal and creating a tight connection. Once the hard grip is complete, a power and data plugs 9 engage, allowing energy and data to be transferred between the docked spacecraft.

The docking process is completed that the area between the hatch on the spacecraft and the hatch on the space

station called the vestibule needs to be pressurized. Once this is done and leak checks are performed the hatchways can be opened up and astronauts can move between the visiting spacecraft and the space station.

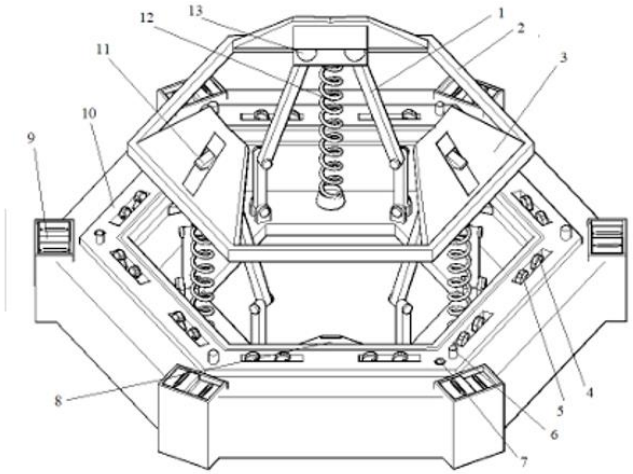

Fig. 8. New design of hexagonal spacecraft docking manipulator

Fig. 8 represents constructive elements of octagonal Euclidean parallel robot manipulator of spacecraft docking system such as 1 – legs; 2 – octagonal junction; 3 – guide petals; 4 - active hook; 5 - passive hook; 6 - guide pin; 7 – guide pin hole; 8 – striker; 9 - latch a power and data plug; 10 - hard capture system; 11 – latch; 12 – spring cable; 13 - hinge (sphere in cylindrical slot).

7. Conclusion

- Based on the analysis it becomes clear that androgynous-peripheral docking manipulators have a number of advantages over the pin-cone design, the main of which is to free astronauts from the complicated work of disassembling the transition tunnel after docking.
- The new manipulator 6RRScs was presented as a hexagonal structure with support chains (legs) on three active planes.
- The soft and hard capture systems of new types of Euclidean manipulators is described.
- The improved version of capture latch system of the Euclidean manipulator is proposed. All improvements of capture latch system is described.
- The developed scheme of the docking mechanism, clearly shows the arrangement of dyads on three active planes, which are connected to the docking element by 4DoF kinematic pairs "sphere-in-cylindrical slot".
- By arranging the support chains on four active planes, it is possible to free up the docking space that is occupied in current designs. The support chains are presented as four flat dyads, which consist of two links with a rotating pair. The connection of the dyads to the octagonal docking element is realised by means of 4DoF of kinematic pair "sphere-in-cylindrical slot".
- Reducing the number of links in the four active planes of the docking manipulator by means of use of a new kinematic pair "sphere-in-cylindrical slot". The new 6DoF octagonal manipulator 4RRScs with four legs on four active planes is presented.
- The structural and cotructive synthesis of the hexagonal and octagonal manipulators are described.
- By combining vector spaces R2 and R3, a new modification of the hexagonal Euclidean manipulator with three closed kinematic circuits 5R create flat five-link mechanism with two degrees of freedom, the connecting coupler point of which is connected to the hinge "sphere-in-cylindrical slot" is obtained.
- For the purpose of determining the number of mobility of the hexagonal Euclidean manipulator 3(5R)Scs, structural synthesis is performed and by using formula for manipulators which contain mixed independent loops with variable general constraint, the number of mobility is calculated.
- Structural form the hexagonal Euclidean manipulator 3(5R)Scs was presented.

- A hard capture system was also presented, with twelwe locks, containing one active and one passive hook each, located on six faces of the docking spar. The spar locks are one of the most critical mechanisms in docking as they are the ones that provide the tightness of the joint.
- The additional cable link has been replaced pirobolts because this one has a smaller number of moving elements and also because of its independence of the cable drive.
- The description of the docking process of the active and passive Euclidean manipulator for docking spacecraft and stations provides an opportunity to review all elements of the Euclidean manipulator design and get their purpose.

References

Afanasyev, I. (2003). Другой корабль [Another spacecraft]. *Новости космонавтики* [News of Cosmonautics], 13(5), 65–71.

Akimenko, A. I., Lebedev, A. I., Okhotsimskiy, D. E., Syromyatnikov, V. S., et al. (1975). *Моделирование на ЭВМ динамики стыковки космических кораблей «Союз» и «Аполлон»* [Computer modeling of the docking dynamics of the "Soyuz" and "Apollo" spacecraft] [Preprint]. Institute of Problems of Mechanics, USSR Academy of Sciences.

Alizade, R. (2019). Structural Synthesis of Robot Manipulators by Using Screw with Variable Pitch. *Universal journal of Mechanical Engineering*, 7(2), 50-63. https://doi.org/10.13189/ujme.2019.070203

Alizade, R. I., Azimov, K. S. & Samadzade, J. A. (2022). Structural synthesis of Euclidean parallel robot manipulators of spacecraft docking system. In *Proceedings of the International Symposium on Electric Aviation and Autonomous Systems, Slovenia, SARES ISEAS 2022* (pp. 109–114). Springer.

Alizade, R. I., Azimov, K. S. & Samadzade, J. A. (2024, May 22-24). Structural and constructive synthesis of octagonal Euclidean parallel robot manipulators of spacecraft docking system. In R. Mukhtarov (chair), *ISUDEF'24 International Symposium on Unmanned Systems: AI, Design and Efficiency* [Symposium]. Azerbaijan.

Alizade, R. I., Azimov, K. S. & Samadzade, J. A. (2024, June 26-28). Structural and constructive synthesis of hexagonal Euclidean parallel robot manipulators of spacecraft docking system. *Abstract book of the MMT Symposium, Portugal*, (pp. 101-102).

Alizade, R. I. & Samadzade, J. A. (2021), A hexagonal Interface Spacecraft Docking System. *Robotics and Automation Engineering Journal*, 5(2), 1-3. https://juniperpublishers.com/raej/pdf/RAEJ.MS.ID.555659.pdf

Androgynous Peripheral Attach System. (n.d.). In *Wikiwand*. https://www.wikiwand.com/en/Androgynous_Peripheral_Attach_System

Bolotnik, N. N. & Shmatkov, A. M. (2007). Об управлении ударным воздействием космических аппаратов при стыковке [On the control of impact forces during spacecraft docking]. *Известия РАН. Теория и системы управления* [Proceedings of the RAS. Theory and Control Systems], (4), 129–136.

Efimenko, G. G. (1984). Математическая модель взаимодействия направляющих элементов стыковочного устройства типа штырь-конус [Mathematical model of the interaction of guide elements in the pin-cone type docking unit]. *Научно-технический сборник* [Scientific and Technical Collection], (8).

Efimenko, G. G. (1995). Особенности математической модели процесса стыковки космических аппаратов с использованием андрогинного периферийного агрегата [Features of the mathematical model of the spacecraft docking process using an androgynous peripheral unit]. *Космонавтика и ракетостроение* [Cosmonautics and Rocket Engineering], (5), 59–66.

Golubev, Y. F. & Yaskevich, A. V. (2020). Компьютерные модели контактного взаимодействия стыковочных агрегатов космических аппаратов [Computer models of contact interaction of spacecraft docking units]. *Keldysh Institute Preprints*. (4). http://doi.org/10.20948/prepr-2020-4

International Docking System Standard (IDSS). (2016). *Interface Definition Document Revision E*. https://www.internationaldockingstandard.com/download/IDSS_IDD_Revision_E_TAGGED.pdf

Mount, G. O. & Mikhalkin, B. (1974). *Six degree of freedom Fortran program "ASTP docking dynamics" user guide*. Space Division, Rockwell International.

Syromyatnikov, V. S. (1984). *Стыковочные устройства космических аппаратов* [Docking devices of spacecraft]. *Машиностроение* [Mechanical Engineering].

Syromyatnikov, V. S. (n.d.). *Снова* АПАС [Again APDU]. WikiReading. https://biography.wikireading.ru/217627

Yaskevich, A. V. (2007). Комбинированные уравнения движения для описания динамики стыковки космических аппаратов с помощью системы «штырь-конус» [Combined motion equations for describing the dynamics of spacecraft docking using the "pin-cone" system]. *Известия РАН. Космические исследования* [Proceedings of the RAS. Space Research], 45(4), 325–336.

Yaskevich, A. V. (2018). Алгоритмы определения параметров контакта при моделировании стыковки и причаливания космических аппаратов [Algorithms for determining contact parameters in modeling the docking and berthing of spacecraft]. *Космическая техника и технологии* [Space Technology and Techniques], (3), 90–102.

National Aviation Academy

International Journal of Transportation Research and Technology

e-ISSN: 3079-6075

DOI: 10.71108/transporttech.vm01is01.02

Research Article

6-DOF Nonlinear Dynamic Modeling and Control of Autonomous Underwater Vehicle

Burak Berkay Kaya*, **Chingiz Hajiyev**

Istanbul Technical University, Istanbul, Türkiye

Timescale of article

Received: 23 August 2024
Accepted: 15 November 2024
Published: 24 December 2024

Corresponding author

Burak Berkay Kaya
kayaburak@itu.edu.tr

Keywords

Dynamic model, 6-DOF, AUV, Feedback linearization, Nonlinear Dynamic inversion

Cite this article as:

Kaya, B. & Hajiyev, Ch. (2024). 6-DOF Nonlinear Dynamic Modeling and Control of Autonomous Underwater Vehicle. *International Journal of Transportation Research and Technology*, 1(1), 17-29.
DOI: 10.71108/transporttech.vm01is01.02

Abstract

During the design process of an autonomous underwater vehicle (AUV), establishing a dynamic model of the system plays a crucial role. Controller (autopilot) is designed based on the dynamic model of the system before the field tests. The controller must reliably manage the system based on the states of the AUV. This study provides a comprehensive guide for the design process of the 6-DOF nonlinear dynamic model and controller of an AUV. Control method used in this study is the nonlinear dynamic inversion method, based on feedback linearization, to establish robust control strategies with a focus on pitch and yaw control. Numerous studies have been conducted in the field of underwater vehicles; however, this research combines both 6-DoF modeling and controller design. Furthermore, it implements the feedback linearization control approach specifically for AUVs. In this study, the nonlinear dynamic model of the AUV is developed and the nonlinear dynamic inversion method is effectively applied to achieve desired control over pitch angle, depth, yaw angle and yaw angular rate.

1. Introduction

A great deal of effort has gone into developing accurate dynamic models for underwater vehicles in the previous years. To understand the complexity of underwater vehicle dynamics, studies by Fossen (2011) and (1994) investigate the hydrodynamics, hydrostatics and control surface effects that are necessary to develop correct 6-DOF simulation models. These seminal works are a significant step toward understanding the complexity of underwater vehicle motion and lay the foundation for future research.

Effective control of underwater vehicles is critical for accurate navigation in difficult underwater conditions. AUVs have been made more stable and maneuverable using a variety of control tactics, ranging from basic PID controllers to more complicated nonlinear control approaches. A detailed study of the feedback linearization approach is presented by Slotine and Li (1991) and Stevens et al. (2016). This control approach is effective in translating underwater vehicles' inherently nonlinear dynamics into a more manageable and controllable form. Feedback linearization simplifies control design and allows for more precise control of AUVs, particularly in the pitch and yaw planes, by converting nonlinear underwater vehicle dynamic equations into linear equations (Zhou & Eustice, 2014).

The pitch controller can be built using a dual-loop methodology (Dougherty & Woolweaver, 1990). The inner loop controls pitch, while the outer loop controls depth. The depth controller generates a reference pitch angle, which serves as the input for the pitch angle controller (Hong et al., 2010). The pitch angle controller determines the elevator deflection required to meet the reference pitch angle. The yaw plane controller can be built around a framework in which the outer loop regulates the yaw angle and the inner loop controls the yaw rate.

There are various controller design strategies accessible, each with its own set of benefits and considerations. One study looks into the usage of sliding mode control (SMC) to construct a pitch controller (Edwards & Spurgeon, 1998). Different controllers' performances are compared by Shetty et al. (2021). The linear quadratic regulator (LQR) is studied by Joshi (2016). This study employs a distinct controller design: the feedback linearization method. For mathematical convenience, the nonlinear system can be divided into three mostly independent linearized subsystems: speed, steering and depth, as specified by Abkowitz (1964). The feedback linearization approach is a powerful control strategy that converts nonlinear dynamics into a controllable form and simplifies control planning.

This study investigates 6-degrees-of-freedom (6-DOF) nonlinear dynamic modeling, with a focus on the complex motion of underwater vehicles. The model precisely calculates forces and moments, demonstrating how propeller-induced thrust, hydrostatics, hydrodynamics, added mass and control surfaces all interact.

Gaining precise control over depth and yaw is one of the most important things we can do to overcome the challenges of the underwater environment. The feedback linearization method is used to develop the controller for the yaw and pitch plane channels.

This study provides a comprehensive guideline by bringing together all these steps. It explores 6-degrees-of-freedom (6-DOF) nonlinear dynamic modeling, with a focus on the complex motion of underwater vehicles. The model precisely calculates forces and moments, demonstrating how propeller-induced thrust, hydrostatics, hydrodynamics, added mass and control surfaces all interact. Gaining precise control over depth and yaw is one of the most important things we can do to overcome the challenges of the underwater environment. The feedback linearization based nonlinear dynamic inversion method is used to develop the controller for the yaw and pitch plane channels.

A nonlinear dynamic model has been developed for REMUS (Remote Environmental Monitoring UnitS), an autonomous underwater vehicle used for search, recovery and mapping missions. REMUS is an open-source AUV, with its physical and hydrodynamic parameters readily available in the literature. Consequently, the methods employed in this study are applied to REMUS but can be extended to any AUV or underwater vehicle, provided its parameters are accessible.

2. Mathematical Models of AUV Kinematics and Dynamics

Linear systems have proportional and understandable relationships between variables. However, nonlinear systems become increasingly difficult, necessitating the use of specialized modeling approaches (Slotine & Li, 1991).

To construct a nonlinear dynamic model of a system, the forces and moments acting on the system must be defined. There are four distinct forces and moments acting on this AUV system. These include hydrostatic, hydrodynamic, propeller thrust and fin forces and moments (Prestero, 2001).

2.1. Hydrostatic Force and Moment

The underwater vehicle is subjected to hydrostatic force and moment due to its weight and buoyancy. This force and moment can be found in the body fixed axis with Eq. 1-3 (Prestero, 2001).

$$f_G = J_1^{-1}\begin{bmatrix}0\\0\\W\end{bmatrix} \quad f_B = J_1^{-1}\begin{bmatrix}0\\0\\B\end{bmatrix} \tag{1}$$

$$F_{HS} = f_G - f_B \tag{2}$$

$$M_{HS} = r_{GB}\ x\ f_G \tag{3}$$

f_G –Gravity Force

f_B –Buoyancy Force

J_1 –Transformation Matrix from Body to Earth Frame (defined in *Eq* 4)

W –Weight

B –Buoyancy

F_{HS} –Hydrostatic Force

M_{HS} –Hydrostatic Moment

r_{GB} –Distance between CG (Center of Gravity) and CB (Center of Buoyancy)

$$J_1 = \begin{bmatrix} cos\psi\ cos\theta & -sin\psi\ cos\phi + cos\psi\ sin\theta\ sin\phi & sin\psi\ sin\phi + cos\psi\ sin\theta\ cos\phi \\ sin\psi\ cos\theta & cos\psi\ cos\phi + sin\psi\ sin\theta\ sin\phi & -cos\psi\ sin\phi + sin\psi\ sin\theta\ cos\phi \\ -sin\theta & cos\theta\ sin\phi & cos\theta\ cos\phi \end{bmatrix} \tag{4}$$

Here, r_{GB} vector is defined. Center of the forces and moments is used as the center of buoyancy (CB) point in this study. It is defined in Eq. 5.

$$r_{GB} = x_{CG} - x_{CB} \tag{5}$$

2.2. Hydrodynamics Force and Moment

The AUV is subjected to several impacts as it moves through the water, resulting in a force and moment on the vehicle. These are referred to as hydrodynamic forces and moments. Hydrodynamic parameters are obtained through CFD (Computational Fluid Dynamics) analyses, which are conducted under various conditions such as different speeds and rates of the system. As a result of these CFD analyses, a set of hydrodynamic force and moment parameters is generated. The forces and moments arising from hydrodynamic effects on the system are then expressed using this set of equations.

The hydrodynamic force and moment can be expressed as Eq. 6-11 (Prestero, 2001).

$$X_{HD} = X_{u|u|}u|u| + X_{\dot{u}}\dot{u} + X_{wq}wq + X_{qq}qq + X_{vr}vr + X_{rr}rr \tag{6}$$

$$Y_{HD} = Y_{v|v|}v|v| + Y_{r|r|}r|r| + Y_{\dot{v}}\dot{v} + Y_{\dot{r}}\dot{r} + Y_{ur}ur + Y_{wp}wp + Y_{pq}pq + Y_{uv}uv \tag{7}$$

$$Z_{HD} = Z_{w|w|}w|w| + Z_{q|q|}q|q| + Z_{\dot{w}}\dot{w} + Z_{\dot{q}}\dot{q} + Z_{uq}uq + Z_{vp}vp + Z_{rp}rp + Z_{uw}uw \tag{8}$$

$$K_{HD} = K_{p|p|}p|p| + K_{\dot{p}}\dot{p} \tag{9}$$

$$M_{HD} = M_{w|w|}w|w| + M_{q|q|}q|q| + M_{\dot{w}}\dot{w} + M_{\dot{q}}\dot{q} + M_{uq}uq + M_{vp}vp + M_{rp}rp + M_{uw}uw \tag{10}$$

$$N_{HD} = N_{v|v|}v|v| + N_{r|r|}r|r| + N_{\dot{v}}\dot{v} + N_{\dot{r}}\dot{r} + N_{ur}ur + N_{wp}wp + N_{pq}pq + N_{uv}uv \tag{11}$$

X_{HD}, Y_{HD}, Z_{HD} –Hydrodynamic Force Components

K_{HD}, M_{HD}, N_{HD} –Hydrodynamic Moment Components

u, v, w –Linear Velocities

p, q, r −Rates

$\dot{u}, \dot{v}, \dot{w}$ −Linear Velocity Derivatives

$\dot{p}, \dot{q}, \dot{r}$ −Rate Derivatives

Hydrodynamic coefficients in the equations are defined by Prestero (2001) for the REMUS AUV.

2.3. Propeller Force and Moment

Because there is no more shared thrust model data, the easiest way to develop this model is to match the propeller thrust to the vehicle's axial drag. The equation is provided in Eq. 12 (Prestero, 2001).

$$X_{prop} = -X_{u|u|}u|u| \tag{12}$$

X_{prop} −Propeller Thrust Force

X_{uu} −Hydrodynamic Coefficient

2.4. Fin Force and Moment

Fins refer to the control surfaces on an underwater vehicle. The force and moment generated by the fins are referred to as fin force and moment. The equations are presented in Eq. 13-16 (Prestero, 2001).

$$Y_{fin} = Y_{uu\delta_r}u^2\delta_r \tag{13}$$

$$Z_{fin} = Z_{uu\delta_s}u^2\delta_s \tag{14}$$

$$M_{fin} = M_{uu\delta_s}u^2\delta_s \tag{15}$$

$$N_{fin} = N_{uu\delta_r}u^2\delta_r \tag{16}$$

Y_{fin}, Z_{fin} −Fin Force Components

M_{fin}, N_{fin} −Fin Moment Components

δ_r −Rudder Deflection

δ_s −Stern (Elevator) Deflection

2.5. AUV Rigid Body Dynamics

6-DoF equations of the motion for the rigid-body are represented with the below simplified equations in Eq. 17-22 (Prestero, 2001).

$$m[\dot{u} - vr + wq - x_{gb}(q^2 + r^2) + y_{gb}(pq - \dot{r}) + z_{gb}(pr + \dot{q})] = \sum X_{ext} \tag{17}$$

$$m[\dot{v} - wp + ur - y_{gb}(r^2 + p^2) + z_{gb}(qr - \dot{p}) + x_{gb}(qp + \dot{r})] = \sum Y_{ext} \tag{18}$$

$$m[\dot{w} - uq + vp - z_{gb}(p^2 + q^2) + x_{gb}(rp - \dot{q}) + y_{gb}(rq + \dot{p})] = \sum Z_{ext} \tag{19}$$

$$I_{xx}\dot{p} + (I_{zz} - I_{yy})qr + m[y_{gb}(\dot{w} - uq + vp) - z_{gb}(\dot{v} - wp + ur)] = \sum K_{ext} \tag{20}$$

$$I_{yy}\dot{q} + (I_{xx} - I_{zz})rp + m[z_{gb}(\dot{u} - vr + wq) - x_{gb}(\dot{w} - uq + vp)] = \sum M_{ext} \tag{21}$$

$$I_{zz}\dot{r} + (I_{yy} - I_{xx})pq + m[x_{gb}(\dot{v} - wp + ur) - y_{gb}(\dot{u} - vr + wq)] = \sum N_{ext} \tag{22}$$

$\sum X_{ext}, \sum Y_{ext}, \sum Z_{ext}, \sum K_{ext}, \sum M_{ext}, \sum N_{ext}$ −Total External Force and Moment in 6-DoF

Acceleration and angular acceleration are computed using the 6-DoF Equations of Motion. Following the calculation of acceleration, the velocity profile is calculated by applying the integral operation to the acceleration. These calculations are carried at the body-fixed coordinate system.

2.6. AUV Kinematics

Kinematics of the AUV is the study of its position, orientation and speed in order to understand how it moves in underwater. The AUV force, moment, linear velocity, angular rates, euler angles and coordinate systems are represented in Fig. 1.

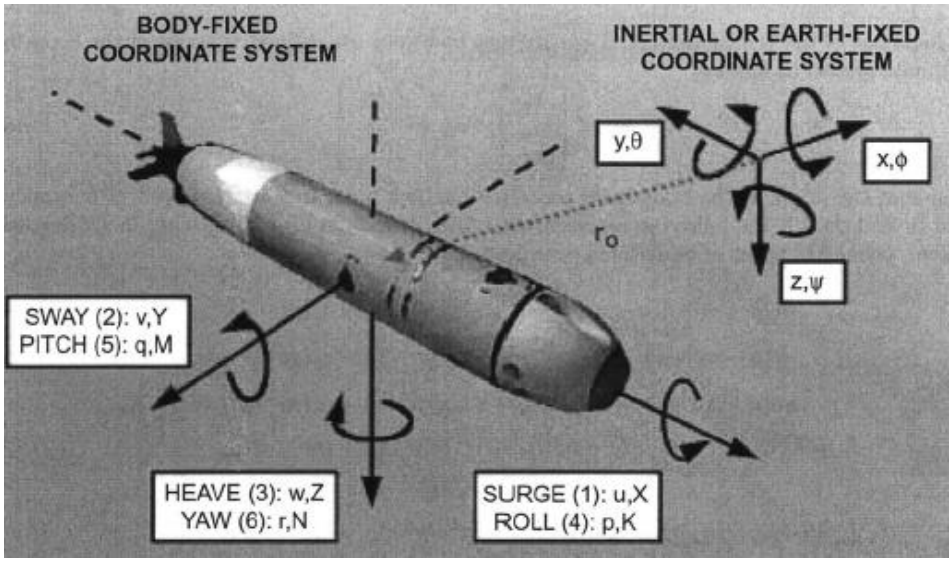

Fig. 1. AUV Coordinate Systems and States

The vehicle's motion in 6-DoF can be specified using the vectors shown in Eq. 23-28 (Prestero, 2001).

$$\eta_1 = [x\ y\ z]^T \tag{23}$$

$$\eta_2 = [\phi\ \theta\ \psi]^T \tag{24}$$

$$v_1 = [u\ v\ w]^T \tag{25}$$

$$v_2 = [p\ q\ r]^T \tag{26}$$

$$\tau_1 = [X\ Y\ Z]^T \tag{27}$$

$$\tau_2 = [K\ M\ N]^T \tag{28}$$

η_1, η_2 –Vehicle's position and orientation with respect to the inertial or earth-fixed reference frame

v_1, v_2 –Vehicle's translational and rotational velocities with respect to the body-fixed reference frame

τ_1, τ_2 –Vehicle's total force and moments with respect to the body-fixed reference frame

Eq. 29 can be used to compute the transformation of translational velocity from the body reference frame to the inertial or earth-fixed reference frame (Prestero, 2001).

$$\begin{bmatrix}\dot{x}\\ \dot{y}\\ \dot{z}\end{bmatrix} = J_1 \begin{bmatrix}u\\ v\\ w\end{bmatrix} \tag{29}$$

J_1 –Transformation Matrix from Body to Earth Frame (defined in Eq. 4)

ϕ, θ, ψ –Euler Angles

u, v, w –Linear Velocities

Eq. 30 can be used to compute the transformation of rotational velocity from the body reference frame to the inertial or earth-fixed reference frame (Prestero, 2001).

$$\begin{bmatrix}\dot{\phi}\\ \dot{\theta}\\ \dot{\psi}\end{bmatrix} = J_2 \begin{bmatrix}p\\ q\\ r\end{bmatrix} \tag{30}$$

J_2 –Transformation Matrix of Rotational Velocity from Body to Earth Frame (defined in Eq. 31)

$\dot{\phi}, \dot{\theta}, \dot{\psi}$ –Euler Angle Derivatives

p, q, r –Rates

$$J_2 = \begin{bmatrix} 1 & sin\phi\ tan\theta & cos\phi\ tan\theta \\ 0 & cos\phi & -sin\phi \\ 0 & sin\phi/cos\theta & cos\phi/cos\theta \end{bmatrix} \tag{31}$$

6-DOF nonlinear dynamic model design process is shared so far. The next step will be the appropriate controller design.

3. Controller Design for AUV Dynamics

The controller design method is nonlinear dynamic inversion which is based on the feedback linearization method. There are two controllers: the pitch plane controller and the yaw plan e controller. Pitch plane controller has two modes: depth and pitch angle controller. Yaw plane controller has two modes: yaw angle and yaw angular rate controller.

The nonlinear state variable form is defined in Eq. 32.

$$\dot{x} = f(x) + g(x)u \tag{32}$$

Error and its derivative is defined in Eq. 33, 34.

$$e = x - x_{ref} \tag{33}$$

$$\dot{e} = \dot{x} - \dot{x}_{ref} \tag{34}$$

Let's define,

$$\dot{e} + K_1 e + K_2 \int e dt = 0 \tag{35}$$

$$\varepsilon = K_1 e + K_2 \int e dt \tag{36}$$

$$\dot{x} = \dot{x}_{ref} - \varepsilon \tag{37}$$

After using Eq. 35-37, control input is represented with the Eq. 38.

$$u = \left[\dot{x}_{ref} - \varepsilon - f(x)\right] g^{-1}(x) \tag{38}$$

3.1. Pitch Plane Controller

Pitch angle and depth control are the two different modes of the pitch plane controller. Fig. 2 shows the pitch plane controller.

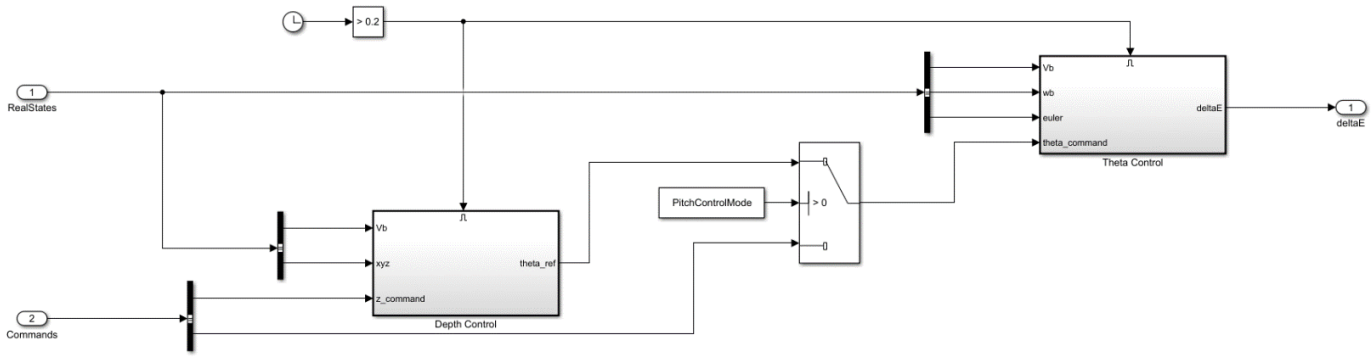

Fig. 2. Pitch Plane Controller

Theta is the inner loop of the pitch plane controller and depth is the outside loop.

To control the depth, a reference depth must be specified as z_{ref}. The θ_{ref} will be determined using the Eq. 39-43 (Kaya, 2024).

$$e = z_{real} - z_{ref} \tag{39}$$

$$\dot{e} + K_1 e + K_2 \int e = 0 \tag{40}$$

$$\dot{z} = \dot{z}_{ref} - K_1 e - K_2 \int e \tag{41}$$

$$V sin\theta = -\dot{z} \tag{42}$$

$$\theta_{ref} = \sin^{-1}(-\frac{\dot{z}}{V}) \tag{43}$$

e −Error

K_1, K_2 −Proportional Gain and Integral Gain

$z, \dot{z}$ −Position-z (Depth) and Position Derivative

z_{real} −AUV Real Depth

z_{ref} −Reference (Desired) Depth for Controller

V −Total Velocity

θ, θ_{ref} −AUV Pitch Angle and Reference Pitch Angle for Controller

The given equation calculates θ_{ref}. The pitch angle controller will use the first and second derivatives of θ_{ref} as input. In the second method, θ_{ref} can be sent directly to the autopilot, as illustrated in the pitch plane controller picture. Autopilot will calculate the necessary δ_e angle to achieve the specified θ_{ref}. Eq. 44-50 shows the process.

$$e = \dot{\theta} - \dot{\theta}_{ref} \tag{44}$$

$$\int e = \theta - \theta_{ref} \tag{45}$$

$$\dot{\theta} = qcos\phi - rsin\phi \tag{46}$$

q, r −Pitch and Yaw Rate

ϕ −Roll Angle

Assume, $\phi = 0$. Then, $\dot{\theta} = q$,

$$\dot{e} + K_1 e + K_2 \int e = 0 \tag{47}$$

$$\left(\ddot{\theta} - \ddot{\theta}_{ref}\right) + K_1\left(\dot{\theta} - \dot{\theta}_{ref}\right) + K_2\left(\theta - \theta_{ref}\right) = 0 \tag{48}$$

$$\ddot{\theta} = \ddot{\theta}_{ref} - K_1\left(\dot{\theta} - \dot{\theta}_{ref}\right) - K_2\left(\theta - \theta_{ref}\right) \tag{49}$$

$$\dot{q} = \ddot{\theta}_{ref} - K_1\left(\dot{\theta} - \dot{\theta}_{ref}\right) - K_2\left(\theta - \theta_{ref}\right) \tag{50}$$

Following this technique, δ_e is determined and transmitted to the system dynamic model. The nonlinear dynamic model calculates the states and sends them to the autopilot again. The system can reach the desired depth or theta angle by applying the controller's δ_e instruction.

3.2. Yaw Plane Controller

Yaw rate and yaw angle controller are the two different modes of the yaw plane controller. Simulation model of the yaw plane controller is given in the Fig. 3.

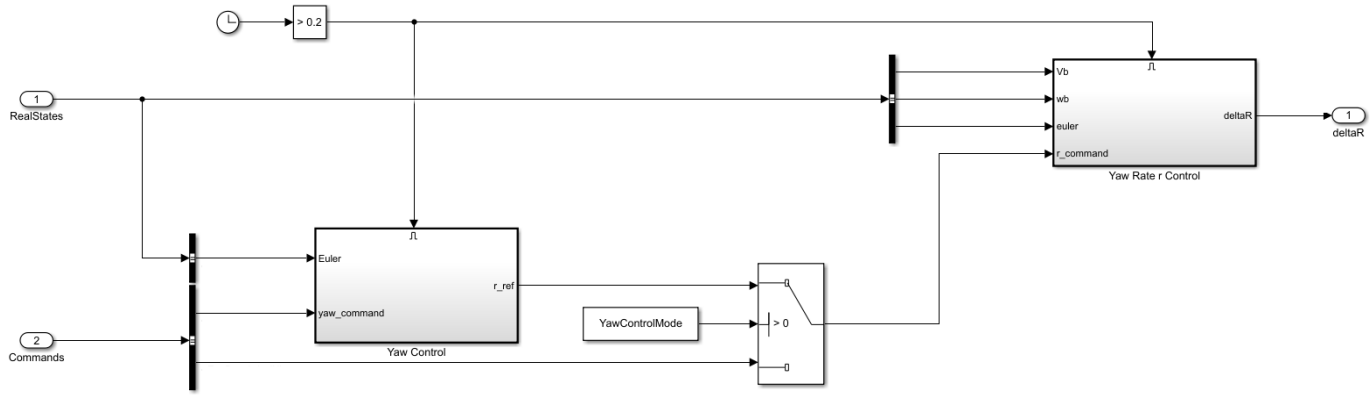

Fig. 3. Yaw Plane Controller

The yaw plane controller has an inner loop that controls the yaw rate and an outside loop that controls the yaw angle.

To control the yaw angle, specify a reference yaw angle ψ_{ref}. Then r_{ref} will be determined using the Eq. 51-54 (Kaya, 2024).

$$e = \psi - \psi_{ref} \tag{51}$$

$$\dot{e} = \dot{\psi} - \dot{\psi}_{ref} \tag{52}$$

$$\dot{e} + K_1 e + K_2 \int e = 0 \tag{53}$$

$$\dot{\psi} = \dot{\psi}_{ref} - K_1 e - K_2 \int e \tag{54}$$

e −Error

K_1, K_2 −Proportional Gain and Integral Gain

$\psi, \dot{\psi}$ −Yaw Angle and Yaw Angle Derivative

ψ_{ref} −Reference (Desired) Yaw Angle for Controller

V −Total Velocity

Eq. 55 shows the conversion of the rotational velocity from the body reference frame to the inertial or earth-fixed reference frame.

$$\dot{\psi} = \left(\frac{sin\phi}{cos\theta}\right) q + \left(\frac{cos\phi}{cos\theta}\right) r \tag{55}$$

q, r −Pitch and Yaw Rate

ϕ, θ −Roll and Pitch Angle

Assume $\phi = 0$, then Eq. 56-57 is formed.

$$\dot{\psi} = \frac{r}{cos\theta} \tag{56}$$

$$r_{ref} = \dot{\psi}\, cos\theta \tag{57}$$

r_{ref} is calculated and the first derivative is fed into the yaw rate controller. In the second option, r_{ref} can be supplied directly to the autopilot, as illustrated in the yaw plane controller picture. Autopilot will compute the necessary δ_r angle to achieve the target r_{ref}. Eq. 58-62 represents the process.

$$e = r - r_{ref} \tag{58}$$

$$\dot{e} = \dot{r} - \dot{r}_{ref} \tag{59}$$

$$\dot{e} + K_1 e + K_2 \int e = 0 \tag{60}$$

$$\dot{r} - \dot{r}_{ref} + K_1 (r - r_{ref}) + K_2 \int (r - r_{ref}) = 0 \tag{61}$$

$$\dot{r} = \dot{r}_{ref} - K_1 (r - r_{ref}) - K_2 \int (r - r_{ref}) \tag{62}$$

Following this technique, δ_r is determined and transmitted to the system dynamic model. The nonlinear dynamic model calculates the states and sends them to the autopilot again. Applying the controller's δ_r command allows the system to achieve the specified yaw angle or rate.

4. Results and Discussion

This section presents some of the controller's results and performance with true states.

The engine model is based on a basic transfer function. The engine model receives an RPM command and responds accordingly. It is used to simulate an RPM changeover. The engine model is shown in Fig. 4.

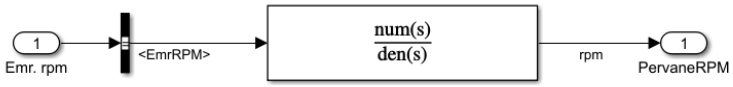

Fig. 4. Engine Model

RPM response for 5000 RPM command is given in the Fig. 5.

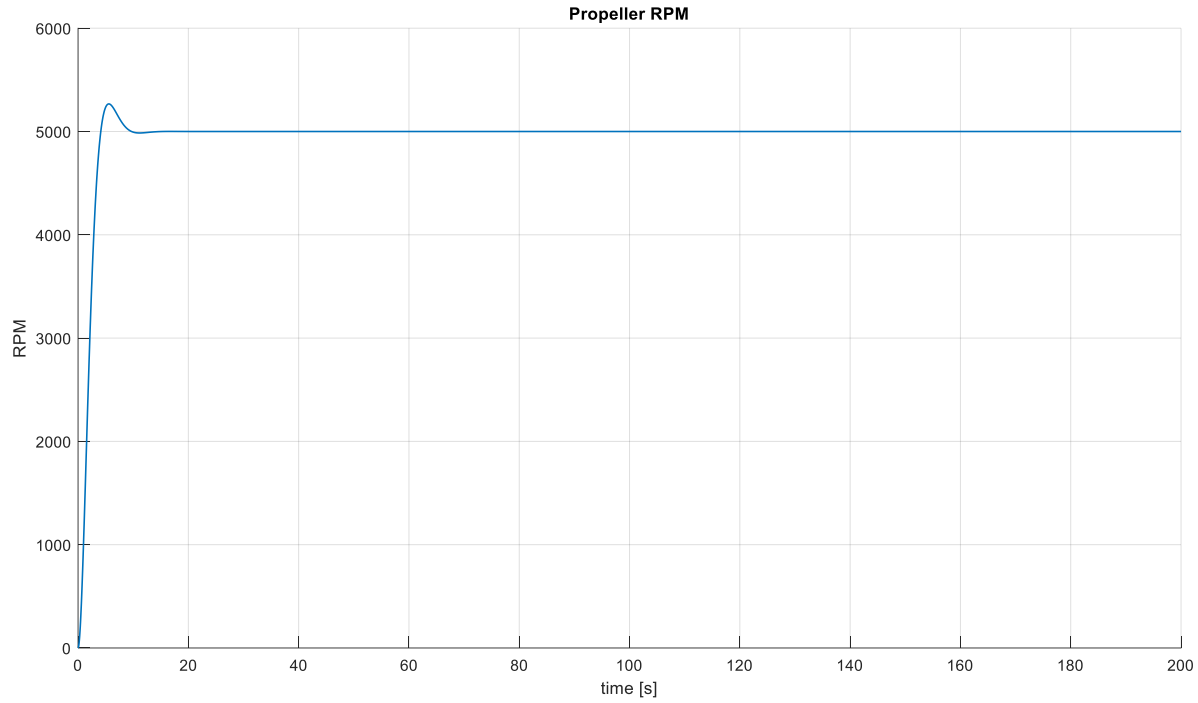

Fig. 5. Propeller RPM Graph

AUV velocity reaches around 5 m/s with this RPM. Graph is given in the Fig. 6.

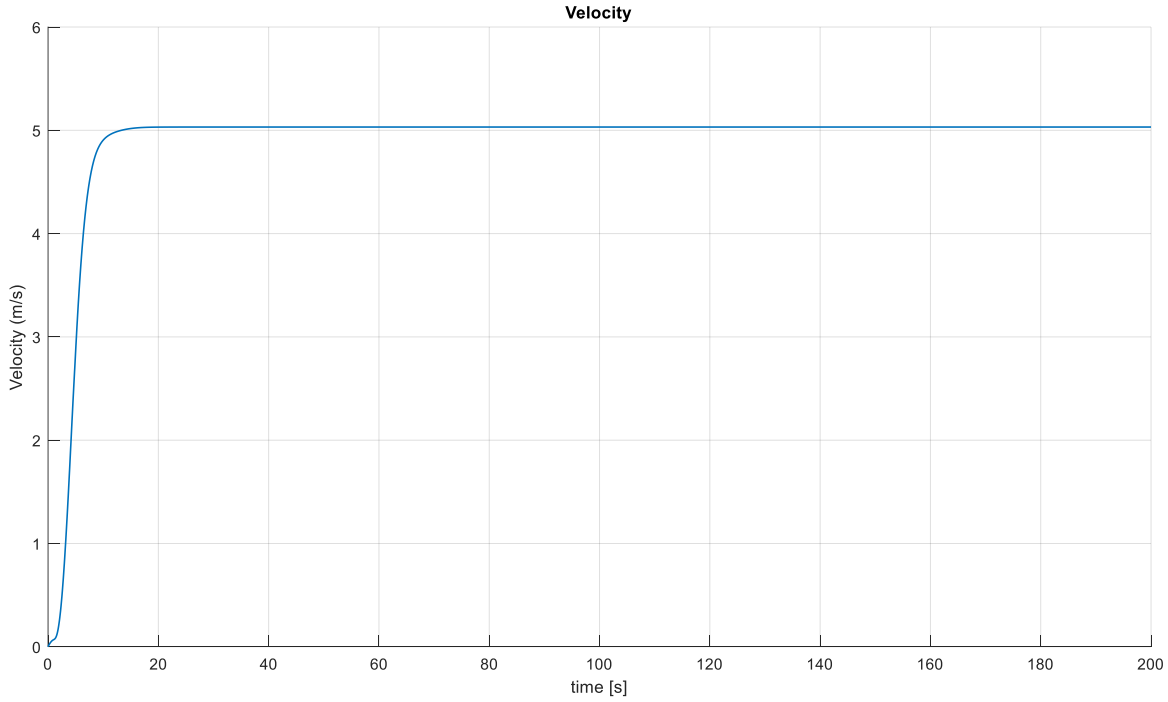

Fig. 6. AUV Velocity Graph

When the AUV moves at this velocity, several commands are issued to the system. Different controller modes are tested. First, the depth control mode is examined. Fig. 7 shows the AUV's command depth as well as its actual depth.

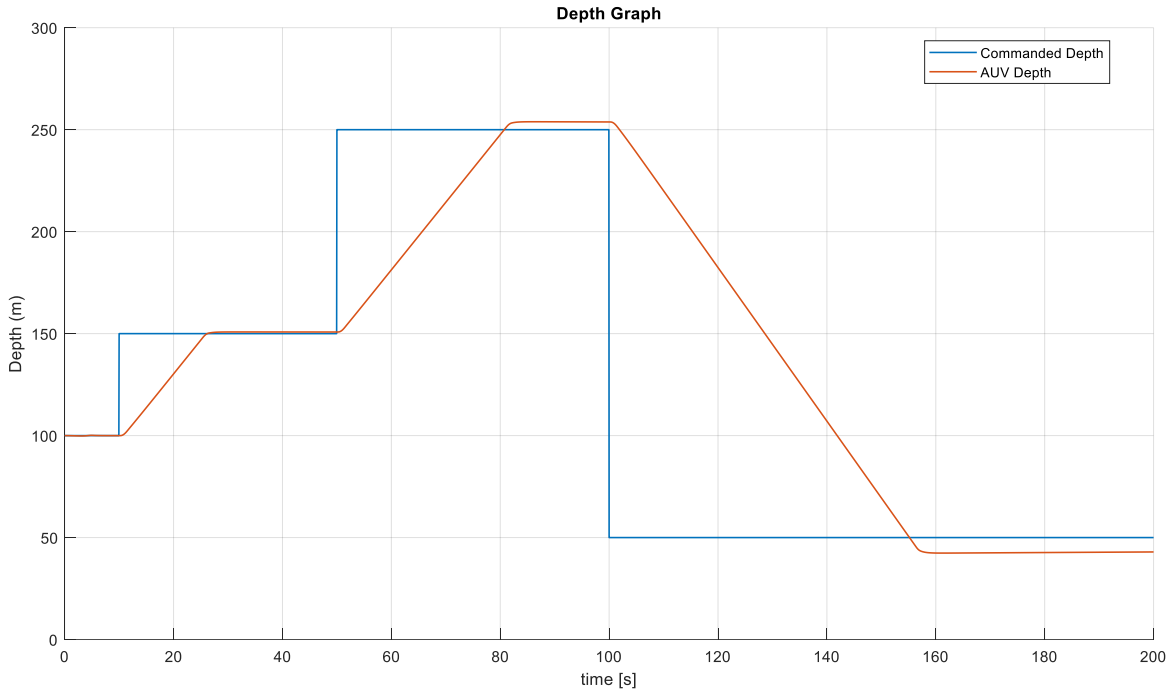

Fig. 7. Commanded Depth vs. AUV Depth Graph

Secondly, theta angle control mode is evaluated. Fig. 8 shows the AUV's commanded and real theta angles.

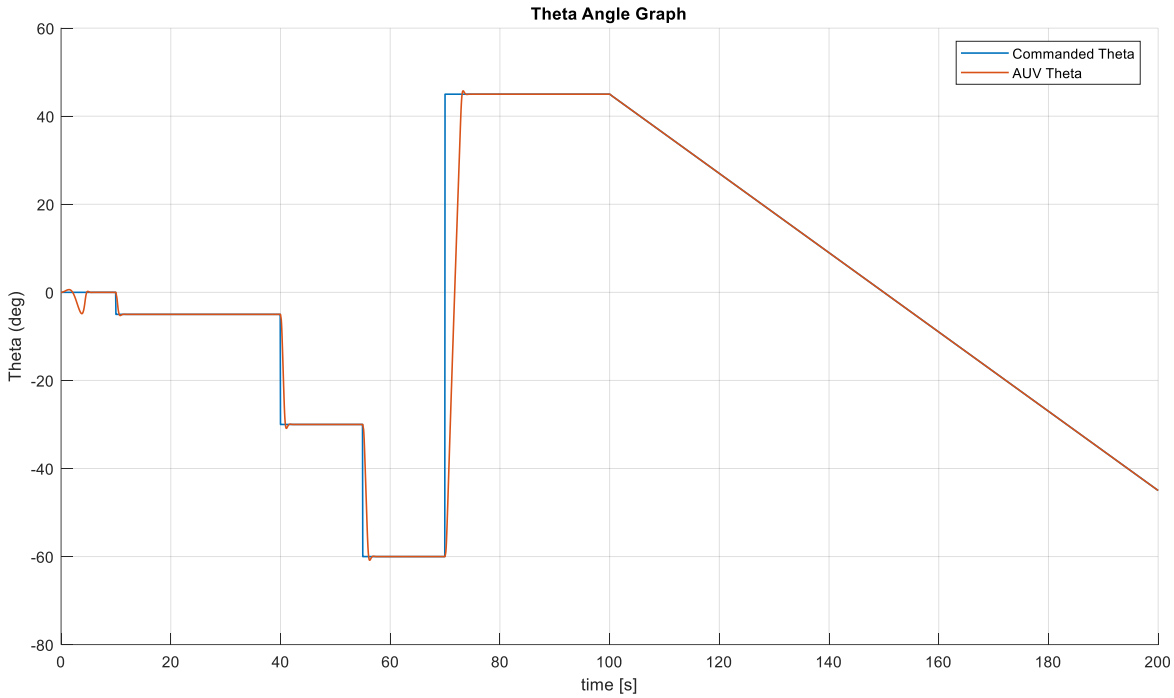

Fig. 8. Commanded Theta vs. AUV Theta Graph

As seen in Fig. 7, 8, the system is capable of executing the appropriate commands in pitch plane. Controller is able to reach the desired the values of theta angle or depth, depending on the pitch plane control mode.

Finally, the yaw controller is tested. The first control mode is yaw angle controller. Fig. 9 depicts the AUV's commanded and actual yaw angles.

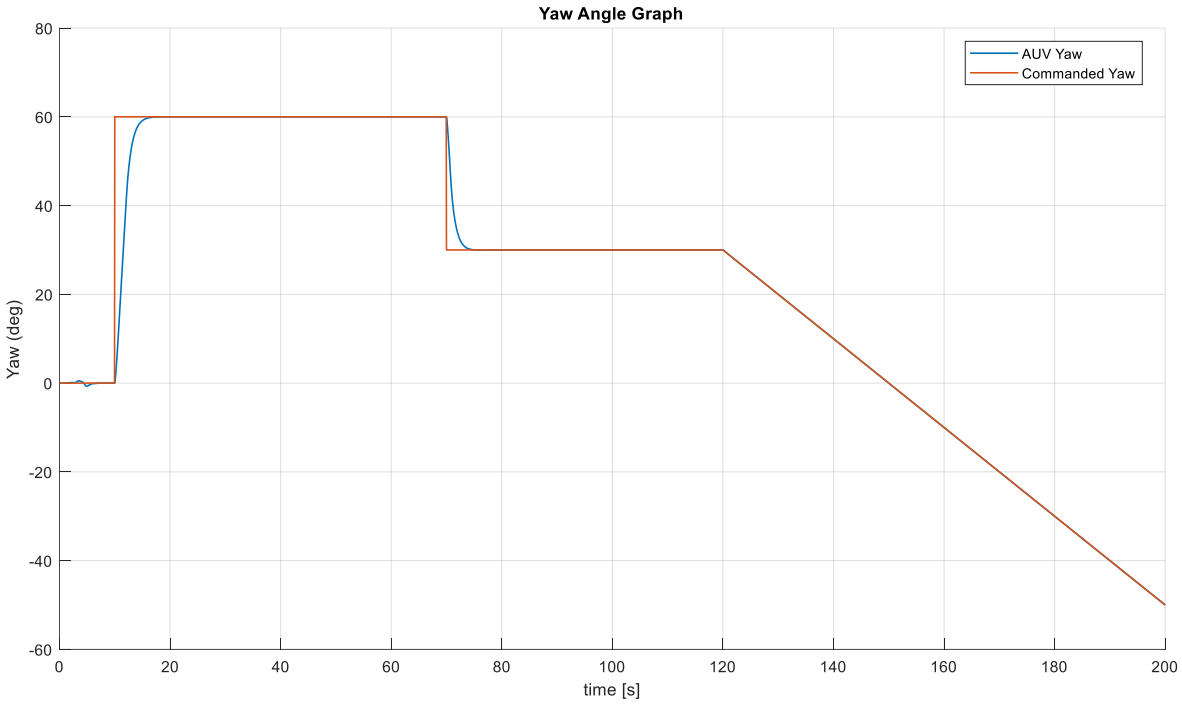

Fig. 9. Commanded Yaw vs. AUV Yaw Graph

Next, the yaw rate controller mode is tested. Fig. 10 shows the system's commanded and true yaw rates.

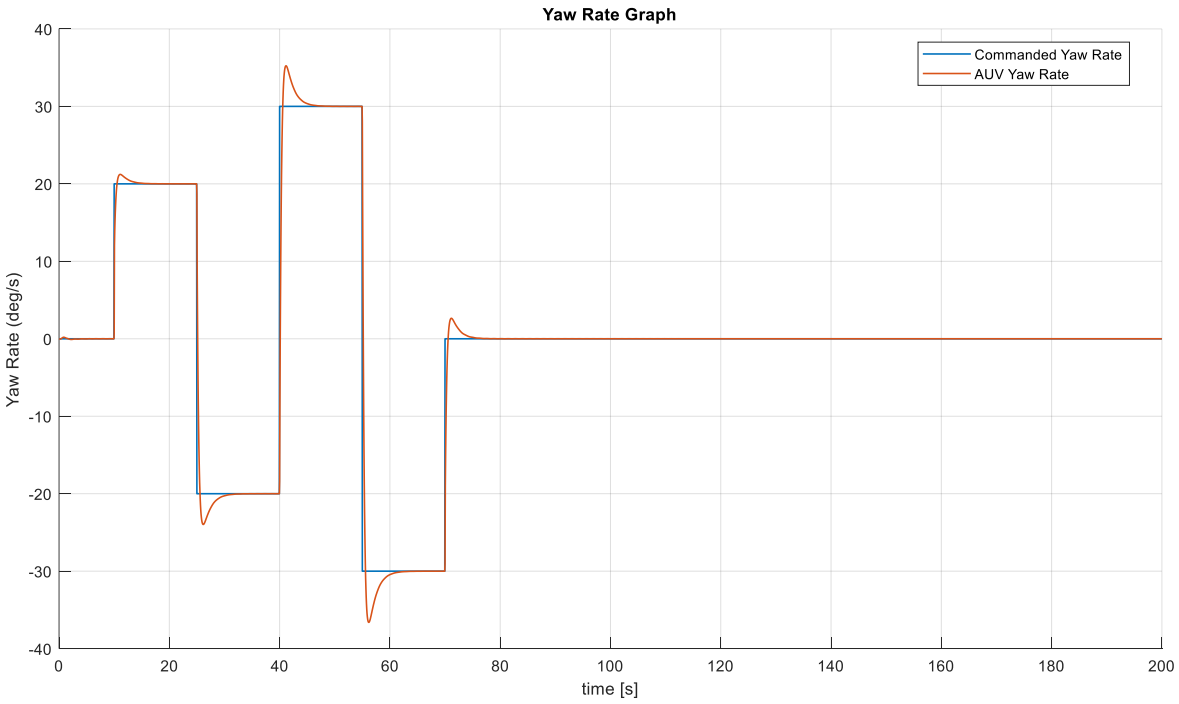

Fig. 10. Commanded Yaw Rate vs. AUV Yaw Rate Graph

As seen in Fig. 9, 10, the controller carries out the desired commands. In the yaw plane, controller is able to successfully reach the desired yaw angle or yaw angular rate, depending on the yaw plane control mode.

5. Conclusions

Autonomous underwater vehicles are being utilized to investigate underwater habitats. This topic is rapidly expanding and has significant implications for research, business and the military. This paper investigates the complex dynamics of nonlinear models with six degrees of freedom (6-DOF) for underwater vehicles. The major goal was to develop an effective control strategy for precise pitch and yaw control utilizing the feedback linearization method.

The 6-DOF dynamic simulation model played an important role in determining how forces and moments affect underwater vehicle movement. Careful consideration of propeller thrust, hydrostatics, hydrodynamics, added mass and control surfaces paved the way for a comprehensive modeling framework. The use of feedback linearization has proven to be an effective solution to problems caused by the nonlinear dynamics that are widespread underwater.

The feedback linearization method was used to convert nonlinear dynamics into a manageable form, making it easier to develop control systems. The proposed technology enhances the mobility and flexibility of autonomous underwater vehicles by providing precise depth and yaw control. This is an important step toward making them more usable in real-world applications.

There are many studies in the underwater vehicles area; however, this research brings up the 6-DoF modelling and controller design topics together. Moreover, this research applies the feedback linearization controller method for the AUVs. This study has made significant progress in helping us understand how to control the state of an underwater vehicle. To ensure that the proposed approaches operate, they should be thoroughly tested in actual underwater fields. Field tests would allow us to learn more about potential difficulties and how effectively the control system performs in various scenarios. Field testing determine whether or not the real-world system dynamics match the simulation model. Simulation models needs to be regularly updated based on field experiments.

Abbreviations

6-DOF	:	6 Degree of Freedom
AUV	:	Autonomous Underwater Vehicle
CG	:	Center of Gravity
CB	:	Center of Buoyancy
m	:	Meter
N	:	Newton
PID	:	Proportional – Integral – Derivative Controller
rad	:	Radian
REMUS	:	Remote Environmental Monitoring Unit
rpm	:	Revolution per Minute
F	:	Force
M	:	Moment
X	:	Force on X Axis
Y	:	Force on Y Axis
Z	:	Force on Z Axis
K	:	Moment around X Axis
M	:	Moment around Y Axis

N : Moment around Z Axis

u,v,w : Velocities at Body Fixed Coordinate Frame

ϕ, θ, ψ : Euler Angles

p,q,r : Angular Velocities (Rates)

References

Abkowitz, M. A. (1964). *Lectures on ship hydrodynamics steering and manoeuvrability*. Hydro-Og Aerodynamisk Laboratorium.

Dougherty, F. & Woolweaver, G. (1990, June 05-06). At-Sea Testing of an Unmanned Underwater Vehicle Flight Control System. *Symposium on Autonomous Underwater Technology*, United States. IEEE. https://doi.org/10.1109/AUV.1990.110438

Edwards, C. & Spurgeon, S. K. (1998). *Sliding mode control: theory and applications*. Taylor & Francis.

Fossen, T. I. (1994). *Guidance and Control of Ocean Vehicles*. John Wiley & Sons.

Fossen, T. I. (2011). *Handbook of Marine Craft Hydrodynamics and Motion Control*. John Wiley & Sons. https://doi.org/10.1002/9781119994138

Hong, E. Y., Soon, H. G. & Chitre, M. (2010, May 24-27). Depth Control of an Autonomous Underwater Vehicle, STARFISH. OCEANS'10 IEEE SYDNEY, Australia. IEEE. https://doi.org/10.1109/OCEANSSYD.2010.5603566

Joshi, S. D. (2016). *Mathematical modeling and robust fault tolerant controller design for autonomous underwater vehicles*.

Kaya, B. B. (2024). *Nonlinear Dynamic Modelling of an Underwater Vehicle, State Estimation and Control.* [Master's thesis, Istanbul Technical University].

Prestero, T. (2001). *Verification of a Six-Degree of Freedom Simulation Model for the REMUS Autonomous Underwater Vehicle*. Massachusetts Institute of Technology.

Shetty, S. G., Subramanian, K. & George, K. (2021, April 23-26). Performance Comparison of Controllers for the Autonomous Underwater Vehicle REMUS 100. *7th International Conference on Control, Automation and Robotics (ICCAR)*, Singapore. IEEE. https://doi.org/10.1109/ICCAR52225.2021.9463492

Slotine, J. J. & Li, W. (1991). *Applied Nonlinear Control*. Prentice Hall.

Stevens, B. L., Lewis, F. L. & Johnson, E. N. (2016). *Aircraft Control and Simulation*. John Wiley & Sons. https://doi.org/10.1002/9781119174882

Zhou, H. & Eustice, R. M. (2014). *Experimental validation of distributed EKF-SLAM on an autonomous underwater vehicle*. IEEE.

National Aviation Academy

International Journal of Transportation Research and Technology

e-ISSN: 3079-6075

DOI: 10.71108/transporttech.vm01is01.03

Research Article

Shipping Towards Decarbonization by Holistic Approach

Mehmet Ziya Sogut*

Piri Reis University, Istanbul, Türkiye

Timescale of article

Received: 31 August 2024
Accepted: 29 November 2024
Published: 24 December 2024

Corresponding author

Mehmet Ziya Sogut
mzsogut@pirireis.edu.tr

Keywords

Shipping, Container Ships, Decarbonization, Efficiencies, Sustainability

Cite this article as:

Sogut, M. Z. (2024). Shipping Towards Decarbonization by Holistic Approach. *International Journal of Transportation Research and Technology*, 1(1), 30-41.
DOI: 10.71108/transporttech.vm01is01.03

Abstract

Despite increasing sectoral demand, maritime transport should improve its ability to manage its fossil fuel-based environmental impacts. In particular, it is important that the International Maritime Organization (IMO) develops regulations in this context and works to support this change in sectoral structures. This study examines the performance of container ships, which are widely used in the sector, with a holistic approach depending on possible consumption patterns. Energy and exergy efficiencies based on the first and second laws of thermodynamics were found to be 39.99% and 22.62% respectively. On the other hand, the improvement rate (IP value) was determined to be 54.26%. At the end of the study, recommendations were developed, in particular on possible action steps towards decarbonization.

1. Introduction

The maritime industry, which accounts for approximately 90% of global trade and economic activity, is acutely aware of its responsibility in addressing climate change and is engaged in a significant transformation to eliminate its environmental impacts. Maritime transport, which has traditionally relied on fossil fuels, is a substantial contributor to global greenhouse gas (GHG) emissions, accounting for an average of 3% of such emissions and being energy intensive (IMO, 2021; Zhuo & Wang, 2022). Efforts to combat climate change, which have developed under the responsibility of sectoral stakeholders, have now gained a new structure with decarbonization targets under the responsibility of the International Maritime Organization (IMO) (IMO, 2021). The maritime sector has a considerable impact on global CO_2 emissions due to its reliance on fossil fuels. In the context of rising demand, fuel consumption in this sector is largely uncontrolled, largely due to the competitive nature of the industry. The primary emission sources in the sector are the combustion of heavy fuel oil (HFO) and marine diesel oil (MDO) in ship engines (Seyam et al., 2023; Sogut, 2024a). In particular, maritime transport is dependent on technologies that have a direct impact on the emission of pollutants beyond CO_2, including sulphur oxides (SOx) and nitrogen oxides (NOx). While these contribute to an increase in global emissions, they also give rise to air quality issues and present a threat to the sustainability of the environment. In this context, the International Maritime Organization (IMO) has established ambitious targets with the objective of reducing greenhouse gas emissions from shipping. Among the key milestones, the objective of achieving a 50% reduction in total annual greenhouse gas emissions by 2050 in comparison to 2008 levels has been identified as a priority target, with the aspiration to achieve zero emissions in the long term (IMO, 2021). These targets have been supported by a number of interim measures, including the introduction of stricter regulations governing the sulphur content of fuels and the implementation of improved energy efficiency standards for newbuilds. Nevertheless, the decarbonization objective, along with all IMO initiatives, has been conceptualized in a more comprehensive manner, thereby facilitating the evolution of a forward-thinking approach. The decarbonization trajectory is beset with challenges, including the high cost of new technologies, the necessity to develop infrastructure (e.g. refueling stations for alternative fuels) and the complexity of retrofitting existing vessels (Ammar & Seddiek, 2023). However, these challenges also present opportunities for innovation, investment and leadership in the sector, given the intensity and conventionality of industry processes and the rapid pace of change. In practice, the maritime sector requires the collaboration of numerous stakeholders, including governments, shipping companies, technology providers and research institutions, to surmount these challenges. The establishment of public-private partnerships and the promotion of international cooperation in advancing the requisite technological developments and policy frameworks provide the fundamental structures for the future sustainable growth of the sector.

The entropy-based approach represents a robust analytical and engineering methodology that can be effectively deployed across a range of disciplines, including thermodynamics, information theory and optimization. It offers a valuable means of evaluating the environmental impact of systems. The concept of entropy, which measures the degree of disorder or uncertainty due to irreversibilities in a system, forms the basis of this approach. In the context of system solutions and applications, the entropy integral approximation algorithm facilitates the generation of efficient results for structural evaluations conducted directly within the system and its interactions with the surrounding environment (Barbieri et al., 2011; Sogut, 2024b). This approach enables the optimization of performance. In general, entropy is understood as a quantitative measure of the level of uncertainty or irreversibility in a system. In thermodynamics, entropy is employed as a quantitative measure of the amount of energy that cannot be harnessed for work due to the presence of irreversibilities within a system. In this regard, it can be regarded as an efficacious instrument, particularly in the context of CO_2 emission regulation pertaining to thermal processes. It is evident that the utilization of existing engine technologies in the maritime sector has the potential to result in a considerable increase in entropy, largely due to the reliance on fossil-based consumption. The primary issue is that it has both environmental implications and potential implications in terms of sectoral responsibilities. In this context, the present study begins with a case study to demonstrate the impact of maritime transport as a sectoral factor. The container example was taken as a basis for evaluation of the potential for entropy-based improvements in the sector, employing an integrated methodology. In particular, this study examines the potential for reducing the irreversibility associated with fossil fuel consumption in terms of power consumption and its environmental consequences.

2. Shipping's Role in Decarbonization

This chapter presents an analysis of the sectoral framework for decarbonization, with a particular focus on the frameworks designed to avoid or reduce overall sectoral carbon dioxide emissions. One of the principal concerns

associated with rising carbon dioxide levels in the maritime sector is the fact that the environmental impact caused by sectoral demands, along with increasing fossil fuel consumption, is on an upward trajectory. Furthermore, there are significant threats such as global warming and climate change, which are leading to rising sea levels and an increase in natural disasters caused by global emissions. The maritime sector, which plays a key role in global logistics, is expected to contribute significantly to greenhouse gas emissions. Therefore, sectoral responsibilities make significant measures valuable, while decarbonization has emerged as an important goal in the sector. As can be seen in Fig. 1, according to Statista, ocean and maritime shipping accounted for 11% of global shipping sector carbon dioxide emissions in 2020.

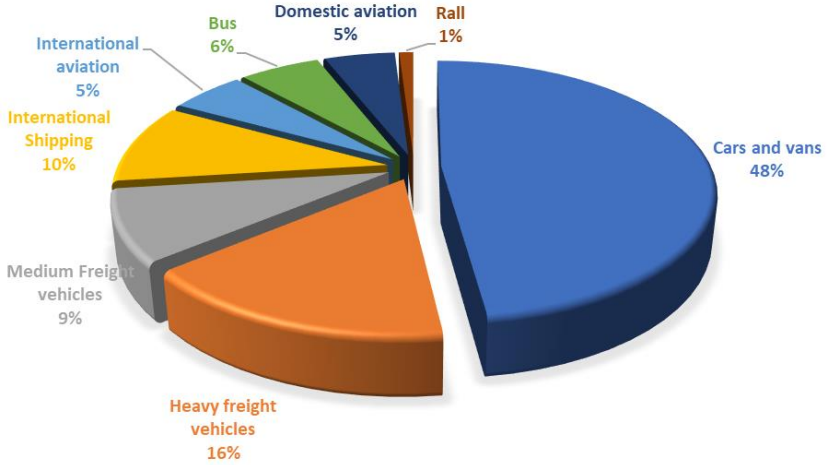

Fig. 1. Distribution of carbon dioxide emission produced by transportation 2022 (Modified from Statista, 2024)

To address this challenge, the maritime sector must embrace a multi-faceted approach to decarbonization. This includes adopting cleaner technologies, improving energy efficiency and exploring alternative fuels (Oloruntobi et al., 2023). Key strategies for reducing emissions in shipping include (Oloruntobi et al., 2023; Koukaki & Tei, 2020; Chuah et al., 2023):

Investing in Innovative Technologies: Advances in technology offer promising solutions for reducing emissions. The development of more efficient engines, the use of renewable energy sources such as wind and solar power and the implementation of electric or hybrid propulsion systems are critical steps toward lowering the carbon footprint of ships.

Enhancing Energy Efficiency: Improving the energy efficiency of ships is essential for reducing fuel consumption and emissions. This can be achieved through measures such as optimizing hull designs, utilizing advanced coatings to reduce drag and implementing energy-saving devices like air lubrication systems.

Adopting Alternative Fuels: Transitioning to alternative fuels like liquefied natural gas (LNG), hydrogen, ammonia and biofuels can significantly cut emissions. These fuels can offer cleaner combustion and lower greenhouse gas emissions compared to traditional marine fuels.

Implementing Operational Measures: Efficient operational practices, such as optimizing routes, reducing speed and better managing cargo loads, can also reduce emissions. These measures can help ships operate more efficiently and minimize their environmental impact.

Regulatory and Market Incentives: Governments and international bodies play a crucial role in supporting decarbonization through regulations and incentives. Policies such as the International Maritime Organization's (IMO) greenhouse gas strategy and carbon pricing mechanisms can drive the industry toward more sustainable practices. By integrating these strategies, the shipping industry can make significant strides toward reducing its carbon footprint and contributing to global decarbonization efforts. The transition to a greener maritime sector is essential for mitigating climate change and ensuring the long-term sustainability of global trade and transport. Decarbonizing the shipping industry is a complex but crucial undertaking, requiring coordinated efforts across technology, operations and policy. Here are the key steps to achieve a more sustainable maritime sector:

Adoption of Cleaner Technologies

Advanced Propulsion Systems: Invest in and implement innovative propulsion technologies, such as electric and

hybrid systems, which reduce reliance on fossil fuels and lower emissions.

Renewable Energy Integration: Utilize renewable energy sources like wind, solar and hydrogen fuel cells to power ships or supplement existing power systems.

Energy Efficiency Improvements

Hull and Propeller Design: Optimize ship hull designs and propeller configurations to reduce drag and enhance fuel efficiency.

Energy-Saving Devices: Install technologies such as air lubrication systems, energy-saving devices and waste heat recovery systems to improve overall energy efficiency.

Smart Navigation Systems: Employ advanced navigation tools and software to optimize routes and reduce fuel consumption.

Alternative Fuels

Liquefied Natural Gas (LNG): Transition to LNG, which burns cleaner than traditional marine fuels and produces fewer emissions.

Hydrogen and Ammonia: Explore hydrogen and ammonia as zero-emission fuels. Both have the potential to significantly reduce greenhouse gas emissions.

Biofuels: Use biofuels derived from renewable sources to reduce reliance on fossil fuels and lower carbon emissions.

Operational Efficiency

Speed Optimization: Implement slow steaming practices to reduce fuel consumption and emissions by operating ships at lower speeds.

Load Management: Optimize cargo loads and improve ballast management to enhance fuel efficiency and minimize emissions.

Voyage Planning: Utilize data analytics and voyage optimization software to plan more efficient routes and reduce unnecessary fuel consumption.

Regulatory Compliance and Innovation

International Regulations: Adhere to international regulations and guidelines, such as those set by the International Maritime Organization (IMO), which aim to reduce greenhouse gas emissions and promote sustainability.

Carbon Pricing and Emission Trading: Engage with carbon pricing mechanisms and emission trading schemes to incentivize the reduction of greenhouse gas emissions and support the development of low-emission technologies.

Investment in Research and Development

Innovative Solutions: Support and fund research into new technologies and practices that can advance decarbonization, such as alternative fuels and energy-efficient technologies.

Collaboration and Partnerships: Collaborate with stakeholders, including governments, research institutions and technology providers, to drive innovation and accelerate the transition to a low-carbon shipping industry.

Training and Awareness

Crew Training: Provide training for crews on new technologies, efficient operational practices and environmental regulations to ensure effective implementation of decarbonization measures.

Industry Awareness: Promote awareness of the importance of decarbonization and encourage industry-wide adoption of sustainable practices.

By systematically implementing these steps, the shipping industry can make significant progress toward reducing its carbon footprint, mitigating the impacts of climate change and contributing to a more sustainable future for global trade and transport.

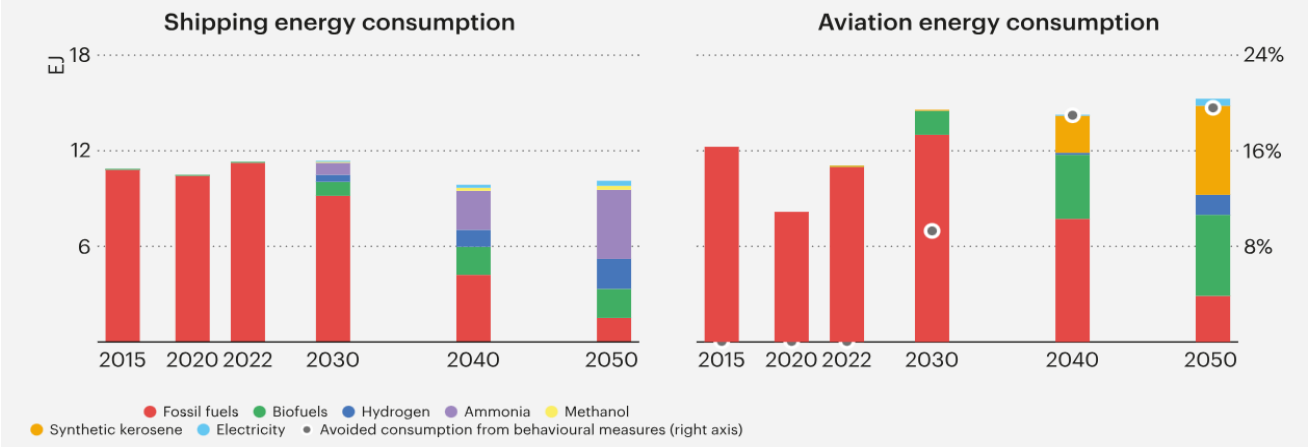

Milestones	2022	2030	2035	2050
Shipping				
International shipping activity (trillion tonne-kilometres)	125	145	165	265
Share in final energy consumption				
Biofuels	0%	8%	13%	19%
Hydrogen	0%	4%	7%	19%
Ammonia	0%	6%	15%	44%
Methanol	0%	1%	1%	3%
Aviation				
International and domestic aviation activity (trillion revenue passenger-kilometres)	6.0	10.9	11.4	16.5
Avoided demand from behavioural measures	0%	9%	14%	20%
Share in final energy consumption				
Biofuels	0%	10%	22%	33%
Synthetic hydrogen-based fuels	0%	1%	4%	37%

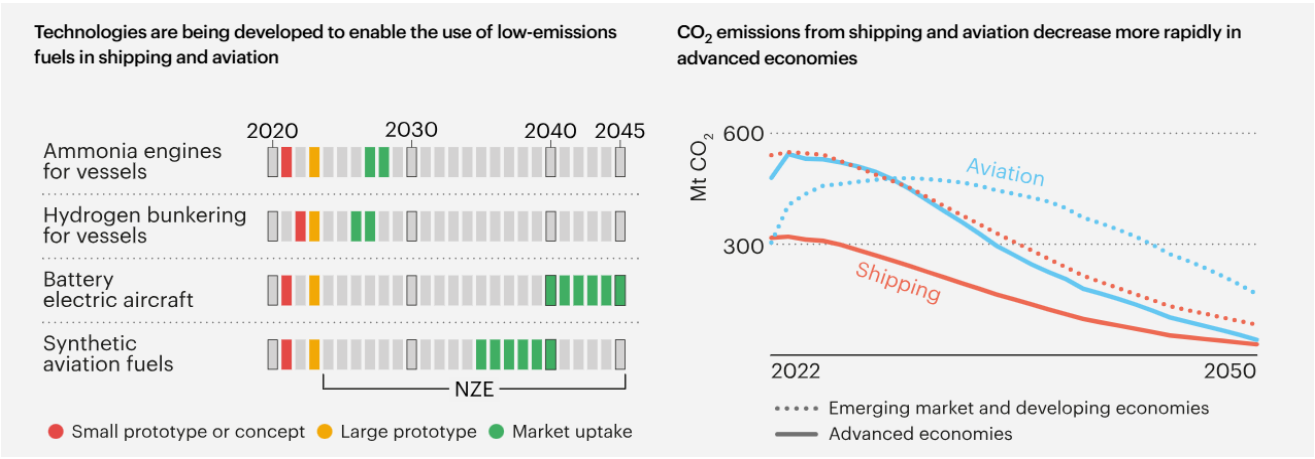

Fig. 2. Emission road of Shipping and Aviation towards 2050 (IEA, 2023)

The aforementioned structural requirements serve as indicators that signal impending change within the transport sector. In particular, the sectoral roles of aviation and maritime transport demonstrate considerable potential for effective action in this regard. In the present era, the instruments that precipitate sectoral transformation directly entail the implementation of structural instruments, particularly those pertaining to low-carbon technologies. The advent of new opportunities, particularly in the domain of energy sustainability, has the potential to facilitate the control and management of CO_2 emissions. Alternative options such as LNG, hydrogen

and ammonia in the maritime sector, along with the proposed sectoral studies on carbon-free fuel preferences, offer promising avenues in this regard. Indeed, the International Energy Agency (IEA) has developed a framework study encompassing both sectors with respect to 2050 targets. According to this report; the projected growth in the consumption of bioenergy, hydrogen and hydrogen-based fuels in the shipping and aviation sectors is set to increase from less than 1% of total energy consumption today to nearly 15% by 2030 and up to 80% by 2050. Furthermore, in order to achieve significant decarbonisation in these two transport modes, enhanced energy efficiency in shipping by 2030 and demand reduction driven by behavioural changes in aviation by 2050 will be essential. The sectoral framework is subjected to a separate analysis in the report, with a breakdown provided in Fig. 2.

3. Holistic Approach for Engineering

A holistic approach (Fig. 3) to engineering entails the integration of diverse perspectives and disciplines, the simplification of the problem domain and the comprehensive addressing of complex problems. In contrast to a narrow focus on technical specifications or isolated components, this approach emphasises the interconnectedness of systems, taking into account how engineering solutions affect and are affected by social, environmental and economic factors. By adopting principles from areas such as systems thinking, sustainability and human-centred design, engineers can develop solutions that not only meet functional requirements but also promote long-term resilience and benefit society as a whole. This broader perspective ensures that engineering projects are not only effective, but also ethical and sustainable and address both current and prospective needs.

Fig. 3. Holistic approach for engineering (Modified from; Torres, 2014)

The holistic approach offers a perspective that directly supports decision-making processes in terms of the holistic effects of thermodynamic systems (Close et al., 2024; Blondel-Canepari et al., 2024). Thermodynamic laws offer a foundational methodology for engineering solutions. The First and Second Laws of Thermodynamics represent the fundamental principles that govern the behaviour of energy in physical systems. The First Law, also known as the Law of Conservation of Energy, postulates that energy cannot be created or destroyed, but rather transformed from one form to another. This law serves to reinforce the fundamental principle that the total energy of an isolated system remains constant. In practical terms, this signifies that the quantity of energy entering a system and the quantity of energy exiting the system must be equal to the variation in the internal energy of the system. This principle is of paramount importance to the comprehension and engineering design of systems where energy transformations are a fundamental aspect of their functionality. To illustrate, in a heat engine, thermal energy is transformed into mechanical work, yet the total amount of energy remains unaltered in accordance with the First Law. The Second Law of Thermodynamics introduces the concept of entropy, which may be defined as a measure of disorder or randomness in a system. The second law of thermodynamics states that in any natural thermodynamic process, the total entropy of a system and its environment always increases

with time. This implies that energy transformations are inherently inefficient, with some of the energy dissipated as heat, which causes entropy to increase. It also emphasises the direction of spontaneous processes, indicating that systems evolve towards greater disorder and equilibrium. The thermodynamic approach guides the design and optimisation of energy systems, improving efficiency and informing understanding of natural phenomena. The analysis of fossil fuel-dependent processes is conducted in relation to mass flow dynamics. These dynamics are examined under steady-state conditions and equilibrium, as described by Cengel and Boles (2014) and Moran et al. (2011). This approach focuses on the energy flow inherent in processes and cycles across all systems. By applying an energy balance to identified energy users, insights can be gained into the environmental consequences of energy use in transportational vehicles.

$$\dot{Q} - \dot{W} + \sum \dot{E}_{in} - \sum \dot{E}_{out} = 0 \tag{1}$$

Where, $\dot{Q}$ and $\dot{W}$ are the net heat and net work produced from boundaries of the system input and output. This structure is directly related to the quantitative values resulting from the defined mass flows. For dead state conditions where energy systems exist, the real extent of possible irreversibility is related to exergy analyses. For such systems and their components, the exergy balance as a function of the dead state temperature for each user behaviour is as follows;

$$\sum(1 - \frac{T_0}{T_k})\dot{Q}_k - \dot{W} + \sum \dot{E}x_{in} - \sum \dot{E}x_{out} - \dot{E}x_{dest} = 0 \tag{2}$$

$\dot{Q}_k$ refers to the heat transfer rate of passing from boundaries of the system, Ex states to the exergy flow of the system passing from boundaries, $\dot{E}x_{dest}$ refers to the exergy destruction of the flow related to seeing the limits of the irreversibility. Flow-induced exergy flow for the system where there is a phisycal processes (ψ);

$$\psi = (h - h_0) - T_0(s - s_0) \tag{3}$$

ψ –Flow exergy (kW)

h –Enthalpy (kJ/kg)

T_0 –Surrounding temperature (K or °C)

s –Entropy (kW/K.kg)

Exergy flow is directly based on the enthalpy (h) and the entropy (s) potentials at the surrounding temperature (T_0) (Cornelissen, 1997). The degree of irreversibility of the system, which refers to the environmental influence in processes, depends directly on the amount of entropy produced. The Gouy-Stodola theorem states that the environmental influence for entropy production is directly due to the irreversibility in the system and depends on the exergy destruction (Moran et al., 2011; Dincer & Rosen, 2012):

$$\dot{E}x_{dest} = T_0\dot{S}_{gen} \tag{4}$$

$\dot{E}x_{dest}$ –Exergy destruction (kW)

T_0 –Surrounding temperature (K)

$\dot{S}_{gen}$ –Entropy generation (kW/K)

All structures consume energy and their environmental performance is a function of their efficiency. In particular, in exergy analysis, the performance of systems depends directly on the effect of the work produced. In fact, the exergy efficiency of a system is defined by the standard exergy efficiency, which is developed based on the data obtained at the inlet and outlet conditions of the flow process. In this context, exergy efficiency is used (Moran et al., 2011);

$$\eta_{Ex} = \frac{\dot{E}x_{out}}{\dot{E}x_{in}} = 1 - \frac{\dot{E}x_{dest}}{\dot{E}x_{in}} \tag{5}$$

η_{Ex} –Exergy Efficiency

$\sum \dot{E}x_{in}$ –Total Exergy input (kW)

$\sum \dot{E}x_{out}$ –Total Exergy output (kW)

$\dot{E}x_{dest}$ –Exergy destruction (kW)

All processes are subject to an assessment in terms of their operational issues and potential for improvement. An important indicator for reducing environmental impact is the potential for improvement in entropy production. Improvement potential for such processes (Van gool, 1997):

$$\dot{IP} = (1 - \eta_{Ex})\left(\sum \dot{Ex}_{in} - \sum \dot{Ex}_{out}\right) \quad (6)$$

IP−Improvement rate (kW)

η_{Ex} −Exergy Efficiency

$\sum \dot{Ex}_{in}$ −Total Exergy input (kW)

$\sum \dot{Ex}_{out}$ −Total Exergy output (kW)

4. Results and Discussion

This study presents an entropy-based model to demonstrate the environmental impact of maritime transport. It takes container transport, which has significant potential in maritime transport, as a basis and assesses the environmental impact and potential for improvement in the sector from a holistic perspective. The data obtained directly points to a proposed potential for the development of decarbonisation. The data used in the study is directly based on the European Union (EU) maritime sector report. It refers to a holistic assessment of the diesel consumption and possible power ranges of the container ships used as reference in the study. The data relating to the container ships used as reference in the study are shown in Fig. 4.

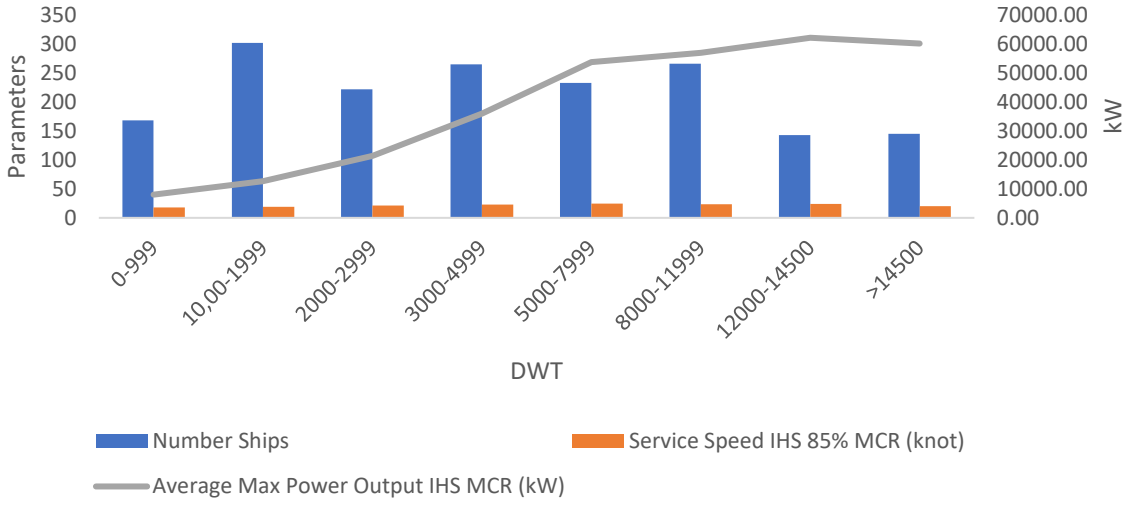

Fig. 4. Data of container

Container ships are divided into eight categories. These distributions can be seen directly as reference values defined for the average power and fuel consumption of the ships. Based on these data, the energy consumption performance of the ships was calculated separately and their energy efficiency was considered separately based on their unit fuel consumption behaviour. The distributions are shown in Fig. 5.

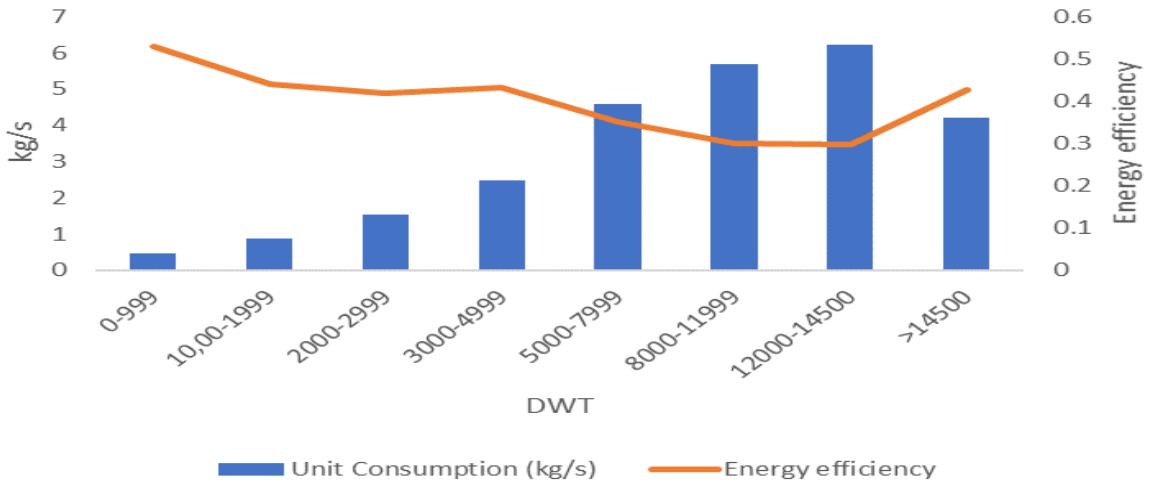

Fig. 5. Energy efficiency for average unit consumption

The average unit consumption of the vessels varies between 0.45 kg/s and 6.2 kg/s, while the efficiency scale shows a variation between approximately 29% and 53%. The most efficient structures are container consumptions in the range 0-999 DWT. The most efficient group within this structure are the ships in the 12000-14000 DWT range. This consumption performance of the vessels was evaluated together with the demand directly related to the engine power. Accordingly, their distribution is shown in Fig. 6.

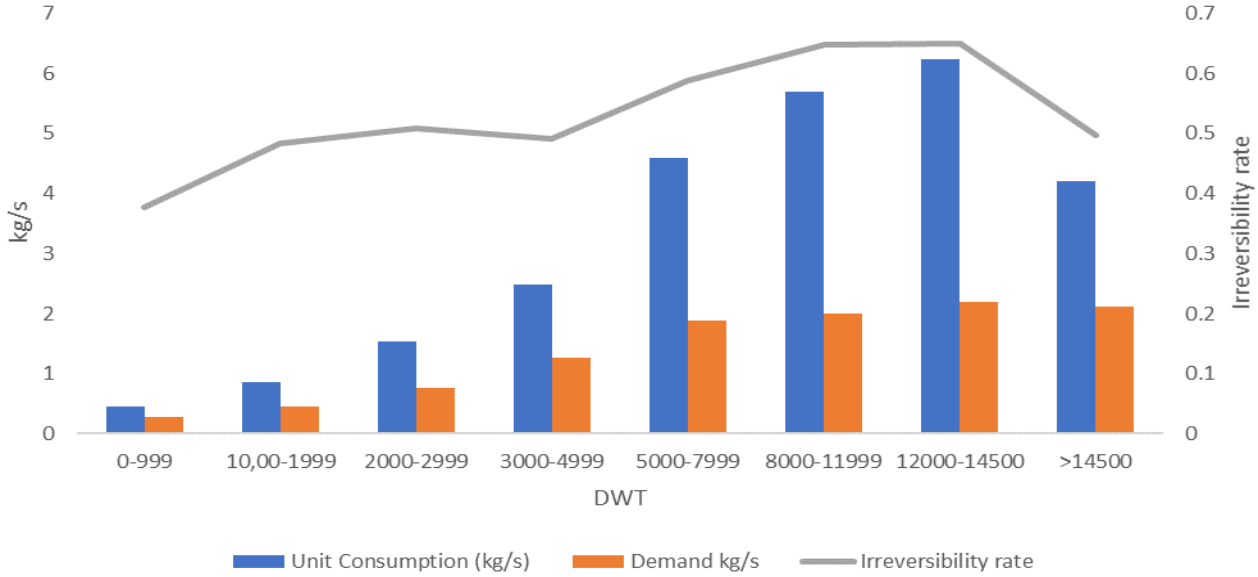

Fig. 6. Demand management of the ships considering irreversibility rate

Irreversibility in ships is the most important problem area that can be defined for process control. The actual energy requirement due to thermal necessity in ships is considered as demand. By comparing the consumption behaviour of the ship with the possible demand, the possible irreversibility rate can be found. While the average consumption for these ships is 3.26 kg/s, the actual consumption demand required by the engines is calculated as 1.37 kg/s. According to this consumption behaviour, the overall irreversibility rate of the ships is found to be approximately 58%. This value is a problem point in terms of consumption behaviour of ships. The consumption behaviour of the ships was evaluated with reference to 25 C ambient and 1 Atm pressure conditions. Accordingly, the exergy performance of the ships is given in Fig. 7.

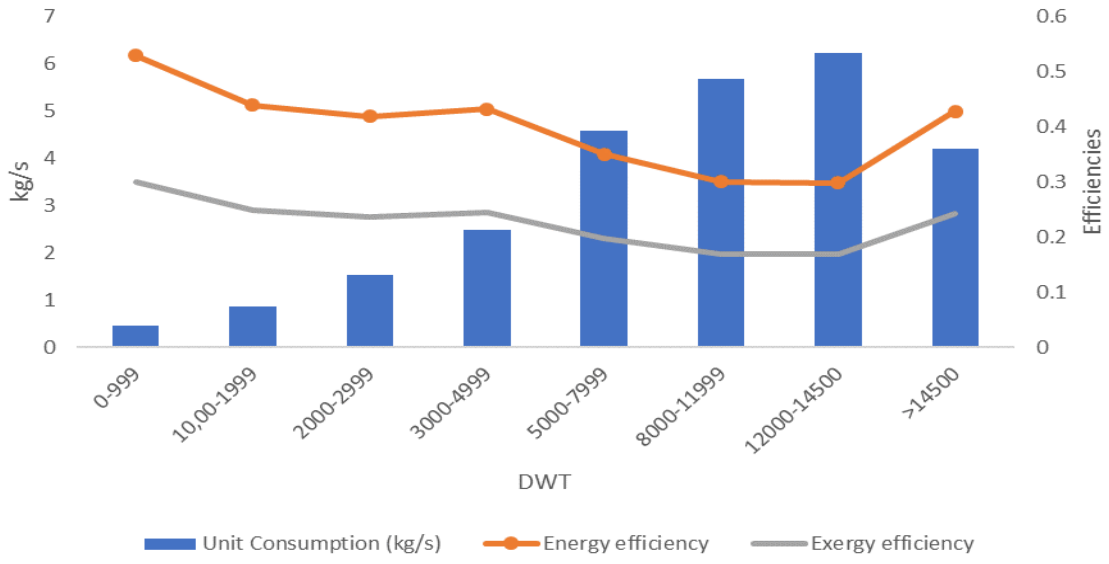

Fig. 7. Efficiencies and unit consumptions

While energy efficiency expresses a quantitative value in terms of thermodynamics, exergy efficiency directly

expresses the quality of irreversibility in the environmental conditions defined for ships. In this respect, the exergy efficiency of ships directly shows a dimension of the maximum work they can produce in the environmental conditions in which they are located. While the average exergy efficiency for the defined structures is 22.62%, it shows that the efficiency range varies between 16.89% and 29.99%. Exergy efficiency can also be seen as a measure of exergy destruction and its rate of evolution. The exergetic parameters for the reference ships are shown in Fig.8.

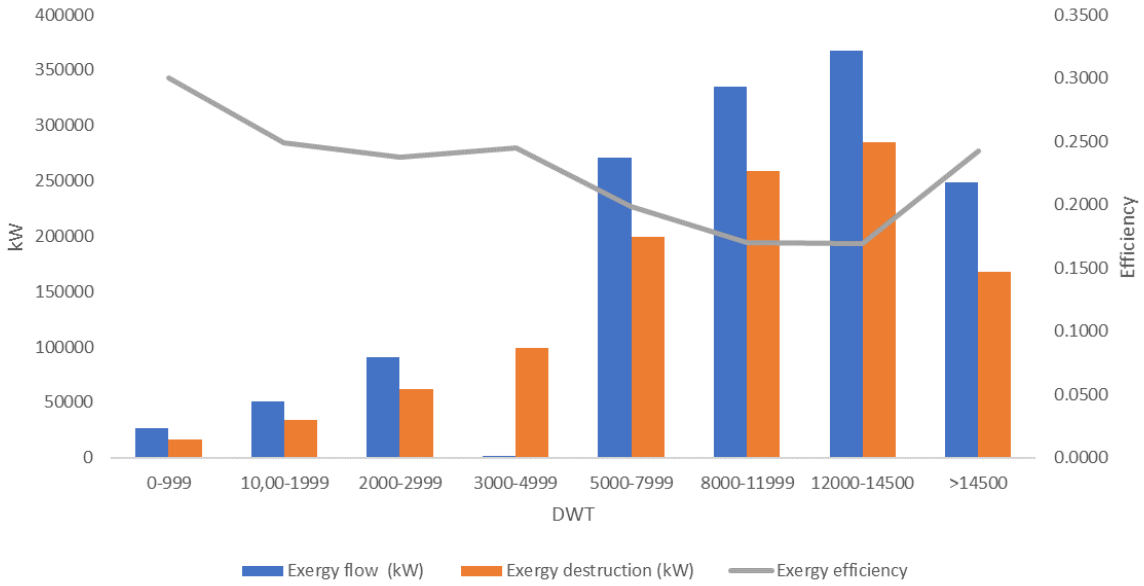

Fig. 8. Exergetic parameters

According to the exergy flows, it can be seen that the linearity of the consumption behaviour has changed, especially for ships above 8000 DWT. This structural effect has a direct impact on ship performance and consumption efficiency. The effect of the consumption behaviour of the ships directly affects the exergy destruction and entropy production in the ships. These consumption perturbations can be due to many reasons together with operational uncontrolled. For this reason, it would be a good choice to control the operational data in terms of process engineering. However, especially the exergy destruction should be considered together with possible improvements in the ships. For this purpose, the Improvement Rate (IP) and its potential effects are shown in Fig. 9.

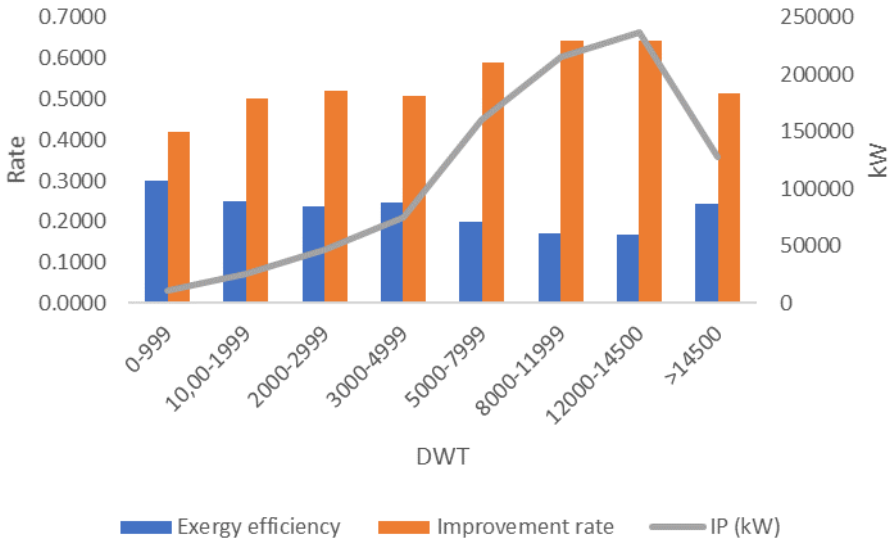

Fig. 9. IP rate of the ships

According to the analyses, the average IP rate for ships was found to be 54.26%. However, the IP rate varies between 42.01% and 64.39%. This value shows how large the irreversibility is for exergy flow. The improvement rate due to exergy flow can be expressed as a rational value for engineering solution. As seen in this study, engine efficiency for container ships shows similar characteristics to literature examples (Tian et al., 2021). This provides information on the evaluation of direct energy performance, especially for diesel engines and their environmental pollution potential due to their irreversibility.

5. Conclusions

This study has been developed primarily to show the impact potential of maritime transport and the energy and exergy analysis of the reference container ships with a holistic approach. In this context, the performance data of the referenced container ships are as follows.

1. The average energy efficiency of the referenced container ships is 39.99.
2. While the average exergy efficiency of the ships is 22.62%, the exergy destruction rate is 77.38.
3. The IP rate due to exergy flow in ships was found to be 54.26% on average.

In this developed approach, it should first be noted that there is an average impact potential of 54.26% for decarbonisation in ships. Process approaches and operational control strategies should primarily be addressed as the reasons for this value. In addition, environmental impact assessments on ships can also be developed as a criterion in this context. In addition to this holistic approach, entropy based environmental impact assessments will provide more realistic results. In particular, the decarbonisation roadmap can be considered as a framework for future studies.

Abbreviations

DWT : Dead Weight Tonnage

IEA : International Energy Agency

IMO : International Maritime Organization

IP : Improvement Potential

References

Ammar, N. R. & Seddiek, I. S. (2023). Hybrid/dual fuel propulsion systems towards decarbonization: Case study container ship. *Ocean Engineering*, 281, Article 114962. https://doi.org/10.1016/j.oceaneng.2023.114962

Barbieri, A. L., De Arruda, G. F., Rodrigues, F. A., Bruno, O. M. & Da Costa, L. F. (2011). An entropy-based approach to automatic image segmentation of satellite images. *Physica A: Statistical Mechanics and its Applications*, 390(3), 512-518. https://doi.org/10.1016/j.physa.2010.10.015

Blondel-Canepari, L., Sarritzu, A. & Pasini, A. (2024). A holistic approach for efficient greener in-space propulsion. *Acta Astronautica*, 223, 435-447. https://doi.org/10.1016/j.actaastro.2024.07.023

Cengel, Y. A. & Boles, M. (2014). *Thermodynamics: an engineering approach* (8th ed.). McGraw-Hill Education.

Chuah, L. F., Mokhtar, K., Ruslan, S. M. M., Abu Bakar, A., Abdullah, M. A., Osman, N. H., Bokhari, A., Mubashir, M. & Show, P. L. (2023). Implementation of the energy efficiency existing ship index and carbon intensity indicator on domestic ship for marine environmental protection. *Environmental Research*, 222, Article 115348. https://doi.org/10.1016/j.envres.2023.115348

Close, J., Barnard, J. E., Chew, Y. M. J. & Perera, S. (2024). A holistic approach to improving safety for battery energy storage systems. *Journal of Energy Chemistry*, 92, 422-439. https://doi.org/10.1016/j.jechem.2024.01.012

Cornelissen, R. L. (1997). *Thermodynamics and sustainable development: the use of exergy analysis and the reduction of irreversibility* [PhD thesis, University of Twente].

Dincer, I. & Rosen, M. A. (2012). *Exergy: Energy, Environment and Sustainable Development*. Elsevier Science.

International Energy Agency (IEA). (2023). *Aviation and shipping*. https://www.iea.org/reports/aviation-and-shipping

International Maritime Organization (IMO). (2021). *International Maritime Organization Fourth Greenhouse Gas Study* 2020. https://www.maritimecyprus.com/wp-content/uploads/2021/03/4th-IMO-GHG-Study-2020.pdf

Moran, M. J., Shapiro, H. N., Boettner, D. D. & Bailey, M. B. (2011). *Fundamentals of engineering thermodynamics*. John Wiley & Sons Inc.

Oloruntobi, O., Mokhtar, K., Gohari, A., Asif, S. & Chuah, L. F. (2023). Sustainable transition towards greener and cleaner seaborne shipping industry: Challenges and opportunities. *Cleaner Engineering and Technology*, 13, Article 100628. https://doi.org/10.1016/j.clet.2023.100628

Seyam, S., Dincer, I. & Agelin-Chaab, M. (2023). A comprehensive assessment of a new hybrid combined marine engine using alternative fuel blends. *Energy*, 283, Article 128488. https://doi.org/10.1016/j.energy.2023.128488

Sogut, M. Z. (2024a). Entropy-based environmental analyses of marine fuel preferences for onboard ships. *Energy*, 305, Article 132260. https://doi.org/10.1016/j.energy.2024.132260

Sogut, M. Z. (2024b). Assessment of entropy-based approach for the environmental impact of the cooling process in clinker production. *International Journal of Exergy*, 44(3/4), 227-243. https://doi.org/10.1504/IJEX.2024.140176

Statista. (2024). *Decarbonization Shipping Industry And Maritime Transport*. https://www.statista.com/statistics/1185535/transport-carbon-dioxide-emissions-breakdown/

Koukaki, T. & Tei, A. (2020). Innovation and maritime transport: A systematic review. *Case Studies on Transport Policy*, 8(3), 700-710. https://doi.org/10.1016/j.cstp.2020.07.009

Tian, Z., Zeng, W., Gu, B., Zang, Y. & Yuan, X. (2021). Energy, exergy, and economic (3E) analysis of an organic Rankine cycle using zeotropic mixtures based on marine engine waste heat and LNG cold energy. *Energy Conversion and Management*, 228, Article 113657. https://doi.org/10.1016/j.enconman.2020.113657

Torres, S. (2014). *Next-Generation MRM: Getting a Big Bang from Breaking Down Traditional Silos*. Talking Logistics.https://talkinglogistics.com/2014/05/15/next-generation-mrm-getting-big-bang-breaking-traditional-silos/

Van Gool, W. (1997). Energy policy: fairy tales and factualities. In O. D. D. Soares, A. M. da Cruz, G. C. Pereira, I. M. Soares & A. J. Reis (Eds.), *Innovation and Technology Strategies and Policies* (pp. 93-105). Springer, Dordrecht. https://doi.org/10.1007/978-0-585-29606-7_6

Zhuo, R. & Wang, H. (2022). Decarbonising Shipping and the Role of LNG: International Law and Policy Trends. In D.S. Olawuyi & E.G. Pereira (Eds.), *The Palgrave Handbook of Natural Gas and Global Energy Transitions* (pp. 319-343). Palgrave Macmillan, Cham. https://doi.org/10.1007/978-3-030-91566-7_13

National Aviation Academy

International Journal of Transportation Research and Technology

e-ISSN: 3079-6075

DOI: 10.71108/transporttech.vm01is01.04

Research Article

Methodology for Assessment of the Technical Condition of Electric Motors and Descriptive Forms of Signals

Huseyngulu Guliyev[1], **Elshan Manafov**[1,2], **Farid Huseynov**[2,3]*

[1]*Azerbaijan Technical University, Baku, Azerbaijan*
[2]*National Aviation Academy, Baku, Azerbaijan*
[3]*Azerbaijan State Oil and Industry University, Baku, Azerbaijan*

Timescale of article

Received: 26 August 2024
Accepted: 05 December 2024
Published: 24 December 2024

Corresponding author

Farid Huseynov
fhuseynov@naa.edu.az

Keywords

Electric motors, Technical condition, Fault types, Diagnostic monitoring, Complex fault, Fuzzy logic

Cite this article as:

Guliyev, H., Manafov, E. & Huseynov, F. (2024). Methodology for Assessment of the Technical Condition of Electric Motors and Descriptive Forms of Signals. *International Journal of Transportation Research and Technology*, 1(1), 42-54.
DOI: 10.71108/transporttech.vm01is01.04

Abstract

Although many different research papers have been conducted on the technical condition monitoring, detection and diagnosis of fast faults in stopping asynchronous motors widely used in transport, industry and household, the creation of a complex monitoring system for this purpose has not been fully resolved. For this purpose, the description and processing methods of various coordinate signals were considered for the construction of complex motor diagnostics and protection systems. It is possible to create an intelligent hybrid model of the fault diagnosis and motor protection system as a result of the grouping of failures of high powered asynchronous motors used in transport with the help of modern sensors. For this, the analog signals received from the sensors should be analyzed, various transformations should be performed on them and the evaluation of the technical condition should be considered based on the obtained final signal.

1. Introduction

The use of electric motors in almost all fields of activity has become the need of the hour: from the utility sector to the most complex industries, the transformation between electrical and mechanical energy is not possible and will not be possible without this type of electric machines. The interdependence between electric motors, the continuity of operation at the transportation, industrial or micro enterprise level, the maintenance of financial profitability and maintenance strategies of any organization, the development of more advanced methods for the detection and diagnostic monitoring of various faults that may occur in motors and this has opened the way for conducting numerous studies in this direction.

Despite numerous researches being conducted in current works on the identification of abnormal modes and protection and technical conditions of electric motors, especially traction motors, the principles, methods and algorithms of the complex approach to the mentioned issues, as well as the issues of realization on a real scale, have not been fully resolved (Merizalde et al., 2017; Stranneby & Walker, 2004).

The aim of the current research work is the real-time diagnosis of faults that may occur in electric motors and the complex grouping of faults and defects that may occur in them to prevent violations of technological activity processes in transport and industry. With the application of modern techniques and technology, the collection of data on the technical condition of electric motors and the monitoring of the condition of these data are of great importance in the correct assessment of the diagnostic condition. To determinei the technical condition of the motors, the informative signals received based on sensors should be processed correctly and certain decisions should be made by performing various analyses on these signals. Due to the processing and analysis of signals, it is possible to determine the technical situation in real-time. Different methods are used for signal analysis and processing, depending on the conditions and the amount of data obtained.

2. Descriptive forms of signals used in the diagnosis of asynchronous motors

Nowadays, a third of the total electricity generated is consumed by electric asynchronous motors, which are applied in various types of activities and industries. Undoubtedly, from the point of view of application, asynchronous motors are more preferable in the field of electric machines. Asynchronous motors, the main workforce of the industry, consume more than 60% of the total electricity produced in the world. Taking into account the variety and scope of application areas, in particular, improving the efficiency of production areas is an urgent issue from the point of view of the timely assessment of the technical condition of motor and their constant maintenance in working conditions to ensure.

Various signal representation forms are utilized in the diagnostics of asynchronous motors. These forms play a crucial role in the analysis and detection of faults within the motor. By analyzing signals in both the time and frequency domains, they provide accurate information regarding different types of faults.
The types of signal representation forms are listed below (Table 1):

- *Time-domain signals*;
- *Frequency-domain signals*;
- *Power spectrum*;
- *Wave packets and short-time fourier transform* (STFT);
- *Hilbert transform and phase analysis.*

Time-Domain Signals. This analysis shows the variation of the signal over time. It is used to directly observe the operational state of the motor and the signs of faults. Signals such as voltage, current, vibration and speed are the primary indicators of this analysis. The key characteristics of time-domain signal analysis are defined by amplitude, mean and RMS values. This method can be employed to detect short-term anomalies and identify rapid changes. For example, during rotor imbalance, an instantaneous increase is observed in the vibration signal.

$$x(t) = \mathrm{A} \cdot sin(\,2\pi f t + \phi) \tag{1}$$

A –Amplitude

F –Frequency

φ –Phase

Frequency-domain signals. In this method, the signal is transformed from the time domain to the frequency domain and the spectral components of the harmonics are analyzed. Fourier Transform (FT) is widely used for this purpose. The key characteristic of frequency-domain signal analysis is the amplitude and phase of the signal at different frequencies. This method can be used to identify sideband frequency components during rotor bar breakage and imbalance. In cases of rotor faults, additional harmonics appear around the 50 Hz frequency.

$$f_s \pm n \cdot f_r \tag{2}$$

f_s −Network frequency

f_r −Rotor slip frequency

n −Harmonic number

Power Spectral Density (PSD). PSD shows the distribution of a signal's power across different frequencies. This method is more suitable for long-term analyses. One of the key features of this method is that the energy value of the signal varies at each frequency. The analysis of the power spectrum is applied in the vibration and noise analysis of motors.

$$PSD(f) = \lim_{T\to\infty} \frac{1}{T} E[|X(f)^2|] \tag{3}$$

$X(f)$ −Fourier transform of the signal

Wave packets and STFT. Wave packets and Short-Time Fourier Transform (STFT) provide time-frequency analysis of the signal. These methods are effective in detecting short-term faults. *Wave packets* are used to localize changes such as vibration and overheating. STFT provides the frequency spectrum of the signal within each time interval. These methods are applied in cases of rotor locking and eccentricity.

Hilbert transform and phase analysis. The Hilbert transform is used to determine the signal's envelope and instantaneous phase. Phase analysis helps detect asynchronous vibration and speed variations. The key feature of this method is the detection of instantaneous amplitude and phase changes. It can be applied to monitor vibration and speed variations.

$$H\{x(t)\} = \frac{1}{\pi} \int_{-\infty}^{\infty} \frac{x(\tau)}{t-\tau} d\tau \tag{4}$$

$H\{x(t)\}$ −Hilbert transform of the signal

Table 1. Comparison of various signal representation forms

Descriptive form	Purpose of use	Method	Field of application
Time Domain	Tracking Instantaneous Changes	Current and Vibration Analysis	Mechanical Coupling, Imbalance
Frequency Domain	Determination of Harmonics	FFT and MCSA	Rotor Bar Breakage
Power Spectral Density (PSD)	Distribution of Power Across Frequency	PSD Analysis	Vibration and Noise Analysis
Time Domain	Tracking Instantaneous Changes	Current and Vibration Analysis	Mechanical Coupling, Imbalance

The use of various signal representation forms in motor diagnostics enables comprehensive analysis. While time-domain analysis is useful for tracking instantaneous changes, frequency-domain analysis accurately identifies the source of faults. Power spectrum, Short-Time Fourier Transform (STFT) and Hilbert Transform play an invaluable role in detecting more complex faults. The combined application of these methods ensures the precise and early detection of motor faults.

Currently, diagnostic monitoring of the technical condition of the motors are carried out by analyzing signals. For this reason, we can start this section mentioned by James Maxwell from a historical point of view and a theoretical basis (Merizalde et al., 2017; Stranneby & Walker, 2004). In his work "Dynamic Theory of the Electromagnetic Field", published in 1864, Maxwell presented a mathematical formula that combines electrical, magnetic and light wave-like behaviour and the energy of wave theories. The subsequent work of other researchers, such as Oliver

Heaviside, made it possible to summarize Maxwell's theory in four equations that demonstrated it more practically. From Maxwell's equations, we can write the equation that expresses the wave nature of the magnetic flux in the air gap, the voltage and current in terms of time and position. The main wave of these periodic sinusoidal signals and their components can be represented by a convergent series of trigonometric functions, i.e.:

$$f(t) = \frac{a_0}{2} + \sum_{n=1}^{\infty} a_n \cos n\,\omega t + \sum_{i=1}^{\infty} b_n \sin n\,\omega t \tag{5}$$

where $\omega = 2\pi \cdot T^{-1}$ and

$$a_0 = \frac{2}{T}\int_0^T f(t)dt;\;\; a_n = \frac{2}{T}\int_0^T f(t)\cos n\,\omega t dt;\;\; b_n = \frac{2}{T}\int_0^T f(t)\sin n\,\omega t dt \tag{6}$$

f –Frequency

T –Period of the signal

In real conditions, the analytical form of the function *f*(*t*) is unknown. *f*(*t*) is specified by a discrete set of equally spaced values (nodal points).

According to the sampling theorem, the number of nodal points of the function *f*(t) with a limited spectrum (N) must be no less than twice the number of the highest harmonic (nm).

When $N=2n_m$, formulas (5)-(6) respectively have the form, where the index (*) determines the estimate:

$$f^*(t) = \sum_{n=1}^{n_m-1}(a_n \cos n\,\omega t + b_n \sin n\,\omega t) + \frac{a_{n_m}}{2}\cos n\,\omega t \tag{7}$$

where

$$a_n^* = \frac{1}{n_m}\sum_{k=1}^{N-1} f(t_k)\cos n\,\omega t_k;\;\; b_n^* = \frac{1}{n_m}\sum_{k=1}^{N-1} f(t_k)\sin n\,\omega t_k \tag{8}$$

If $N>2n_m$ (let's take $N=2(n_m+1)$).

$$f^*(t) = \sum_{n=1}^{n_m}(a_n \cos n\,\omega t + b_n \sin n\,\omega t) \tag{9}$$

where

$$a_n^* = \frac{1}{n_m+1}\sum_{k=1}^{2n_i+1} f(t_k)cosn\omega t_k;\; b_n^* = \frac{1}{n_m+1}\sum_{k=1}^{2n_i+1} f(t_k)\sin n\,\omega t_k \tag{10}$$

The formula is more clear from the point of view of harmonic analysis

$$f^*(t) = \sum_{n=1}^{n_m} A_n \sin(n\omega t + \psi_n) \tag{11}$$

where A_n is the amplitude of the nth harmonic

$$A_n = \sqrt{a_n^2 + b_n^2} \tag{12}$$

ψ_n – n-th harmonic offset angle

$$\psi_n = arctg(a_n/b_n) \tag{13}$$

Note that if we take the standard deviation δ as a criterion for assessing accuracy, i.e.

$$\delta^2 = \frac{1}{2\pi}\int_0^{2\pi}[f(t) - f^*(t)]^2\, dt \tag{14}$$

Then the greatest accuracy of approximation f(t) occurs if the coefficients a_n and b_n are calculated using formula (6).

Representation of the signal on a time scale allows to know some parameters such as amplitude, frequency, phase and conduct modulation. Nevertheless, when it is necessary to know the origin or causes of any abnormality that has arisen, it is preferred to study the frequency domain (Fig. 1) and this is done with the help of Fourier analysis (Merizalde et al., 2017; Boukra & Lebaroud, 2010; Zhang et al., 2011).

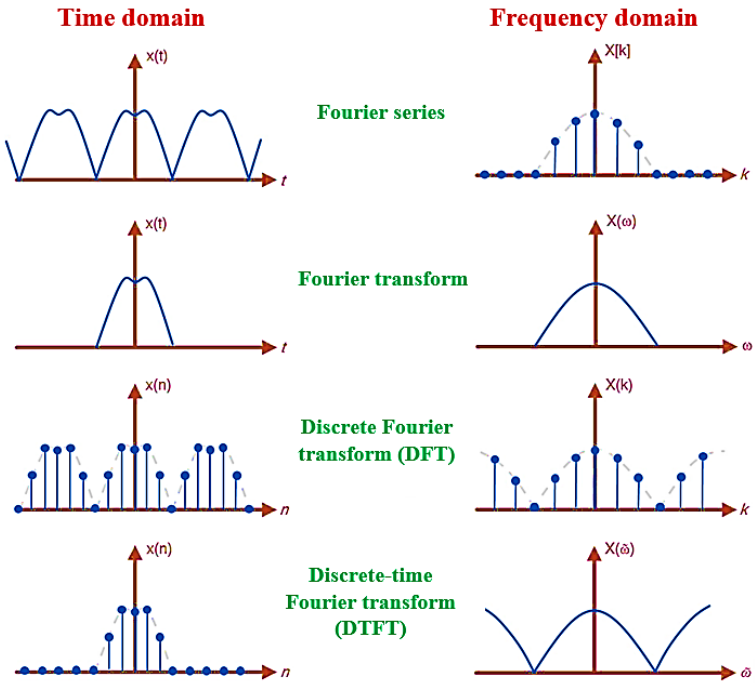

Fig. 1. Signal representations at different scales: time, amplitude, frequency space

According to Hansen, a periodic and continuous signal can be transformed into an aperiodic and discrete signal based on Discrete Fourier Transform (DFT). After exchanging the time and frequency domains, this signal can be converted back into a continuous signal based on the Discrete Time Fourier Transform (DTFT), making the first discrete and the second continuous (Fig. 2).

In its simplest form, the DFT can be written according to. The complex computations performed are proportional to N^2 and $N\log_2 N$ (where N is the number of signal samples) representing the significant quantity. For this reason, in the algorithms used to obtain the DFT, the repetition of operations, the symmetry of the functions with respect to the abscissa axis and the periodicity are significantly used to facilitate and simplify the calculation. This methodology is known as Fast Fourier Transform (FFT). The energy and spectral density are respectively given by:

$$X_N k\frac{\omega_S}{N} = \sum_{n=0}^{N-1} x_N(n)\cdot e^{-j2\pi(\frac{kn}{N})} = \sum_{n=0}^{N-1} x_N(n)\cdot W_N^{kn} \tag{15}$$

$$X_N k\frac{\omega_S}{N} = \sum_{n=0}^{N-1} x_N(n)\cdot W_N^{kn} = \sum_{n=0}^{(\frac{N}{2})-1} x_N(2n)\cdot W_{\frac{N}{2}}^{kn} + W_N^{kn}\sum_{n=0}^{(\frac{N}{2})-1} x_N(2n+1)\cdot W_{\frac{N}{2}}^{kn} \tag{16}$$

$$\sum_{n=-\infty}^{\infty}|x(n)|^2 = \frac{1}{2\pi}\int_{-\pi}^{\pi}|x(n)|^2\,d\omega = \frac{1}{2\pi}\int_{-\pi}^{\pi} S_{xx}\,d\omega \tag{17}$$

$$\varphi_{xx}(\omega) = \sum_{k=-\infty}^{\infty} R_{xx}(K)\cdot e^{-j2\pi(\frac{\omega}{\omega})k} \tag{18}$$

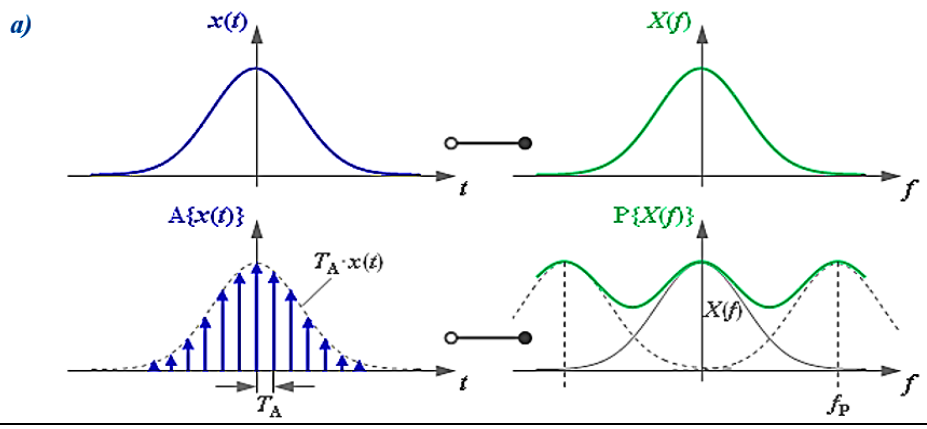

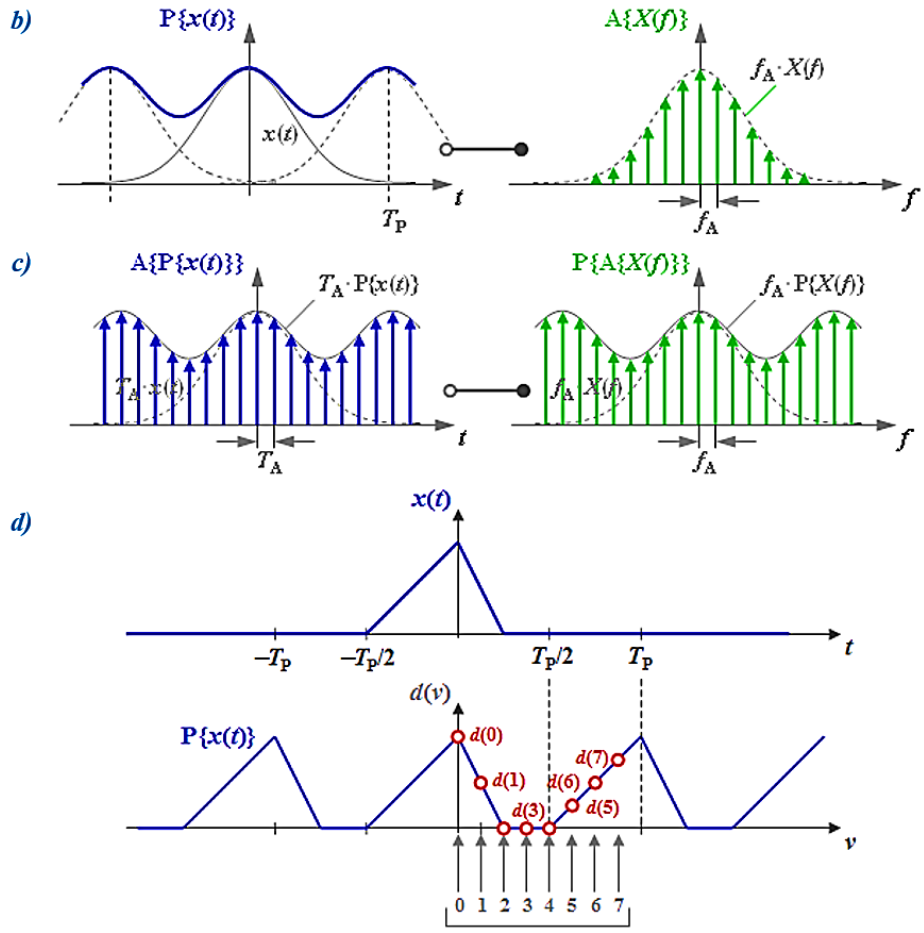

Fig. 2. Signal transformation based on Discrete Time Fourier Transform (DTFT) (A{x(t)}: Signal x(t) after "sampling" → A{...}; P{X(f)}: Spectrum X(f) after "periodification" →P{...}) *a) Time discretization – Periodification in the frequency domain*; *b) Frequency discretization – Periodization in the time domain*; *c) Finite signals of the Discrete Fourier Transform (DFT)*; *d) On assigning of the DFT coefficients*

The DFT is a basic computational tool for analyzing the spectrum of a signal, but the output frequencies are modeled as sums of sinusoids that can be differentiated. Diagnosing the condition by independently analyzing the signal in the time or frequency domain can be improved by using Time-Frequency Representation (TFR). An even more sophisticated toolkit can be obtained by using directly classified TFR in the Doppler uncertainty plane to extract vectors associated with faults. Researchers propose a decision criterion based on "Mahalanobis distance" to safely diagnose broken rotor bars, pads and stator faults (Merizalde et al., 2017; Garcia-Perez et al., 2011; Batista et al., 2016).

Regardless of the methodology used, it is more convenient to use FFT as the main tool for signal analysis in monitoring, detecting and diagnosing faults in asynchronous motors.

The application of the latest wave "Artificial Intelligence" - AI (Artificial Intelligence) technique is preferred in the methodology for diagnosing faults of electric motors. Research should be deepened in the direction of creating such systems that allow making decisions as close as possible to the thinking of the human brain, so that each of the failure can be diagnosed separately and comprehensively evaluated when several failure occur at the same time (Manafov & Huseynov, 2023).

One such system is the theory of "Fuzzy Logic", which serves as an effective tool in the diagnostics and signal analysis of motors. This theory is widely applied to assess the technical condition of electric motors, detect faults and implement preventive measures, as it enables working with uncertainty and imprecise data.

In this context, data on motor vibrations, temperature, noise levels and current fluctuations are analyzed based on fuzzy logic rules. For instance, if vibration levels are high and the current deviates from the norm, it indicates a mechanical problem in the motor. Furthermore, fuzzy systems analyze current and vibration signals to *detect*

faults in the stator or rotor, such as short circuits, insulation failures, or broken rotor bars. *Problems related to load* – such as instability during load conditions or abnormalities in operating modes – are also evaluated using fuzzy logic.

Fuzzy logic plays a crucial role in signal analysis. *In spectral analysis*, spectral components obtained through Fourier or wavelet transforms of vibration or noise signals are fed into the fuzzy logic system. Fuzzy rules then determine whether faults exist within specific frequency ranges. Additionally, "*signal filtering and noise reduction*" are achieved through fuzzy logic-based filtering to minimize external noise and isolate the useful components of the signal. Fuzzy systems accurately identify transition zones between "normal" and "abnormal" conditions in signals.

Fuzzy logic-based systems offer several advantages in determining the technical condition of motors. *Adaptation to uncertain systems* allows the detection of faults in early stages, even when signals are asymmetric or indicators are imprecise. *Real-time monitoring* becomes possible, enabling the tracking of motor performance during startup, loading and normal operation.

Thus, fuzzy logic provides significant benefits in motor diagnostics and signal analysis, as it enables the precise identification of instabilities and early detection of faults in motor operation. These systems not only mimic human expertise but also automate the decision-making process in real time.

In this direction, the diagnosis of faults of electric motors based on the use of Soft Computing paradigms has recently been given place. In this case, the use of fuzzy logic apparatus is more relevant. At the same time, in this case, it is not required to know the exact analytical relationship between the input and output quantities of the diagnostic system and it is enough to approximate this relationship in linguistic language ("if"-"then") (Manafov et al., 2022; Boukra & Lebaroud, 2010; Bellini et al., 2008; Zhang et al., 2011).

$$R_i: if \;\; e = A_i \; and \; \dot{e} = B_i \; then \; u = C_i \tag{19}$$

Where A_i, B_i and C_i - are fuzzy sets; $e, \dot{e}$ – is a signal about the technical condition of the motor and its derivative.

The output signal is determined by minimizing the fuzzy logic output and defuzzifying the center of gravity:

$$u(e,\dot{e}) = \frac{\sum_{i=1}^{n} \overline{C_i} \, min\left(\mu_{A_i}(e), \mu_{B_i}(\dot{e})\right)}{\sum_{i=1}^{n} min\left(\mu_{A_i}(e), \mu_{B_i}(\dot{e})\right)} \tag{20}$$

Where $\mu_i(\cdot)$ –denotes the membership functions of the signals.

When the quantity $\overline{C_i}$ reaches the maximum of C, it represents the quantity u. A triangular representation of the membership function in this model is given in Fig. 3.

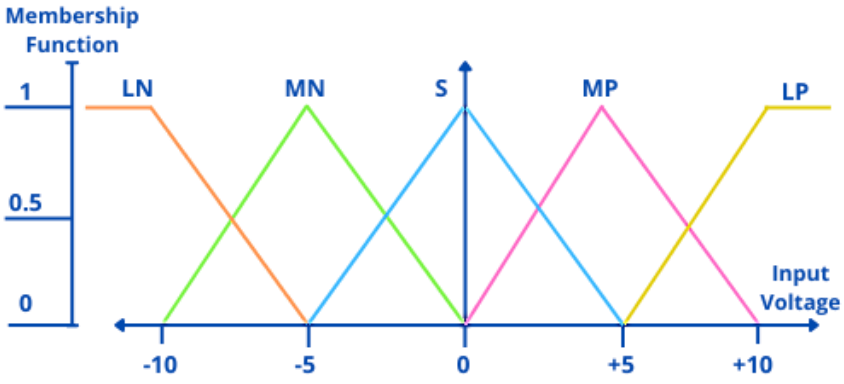

Fig. 3. Normalized triangular membership function

3. Types of failures of asynchronous motors and statistics of their occurrence

Many factors and failures cause the deterioration of the technical condition of the motor. Therefore, faults of electric motors can be classified from different perspectives as shown in table 2. Table 2 shows a preliminary grouping of the environmental factors to which the motor is exposed and which may cause failures. A factor can often belong to more than one group.

Various studies have been conducted in the direction of statistical grouping of faults. Table 3 shows several statistics sorted by source of studies. Although there is no coincidence with the prices, we can observe that the trend is very similar for the included cases. Thus, the failure rates are classified in the following form from the largest to the smallest: bearings, stator and rotor.

Table 2. Factors that cause failures in electric motors

Environmental	Operations	Equipment	Human	Electric power
Temperature	Vibration	Aging	Bad selection of electric motor	Transients due to: Short circuit Fluctuations Resonance Transfers Reconnections Capacitors Insulation Drivers
Moisture	Overload	Quality	Bad use	Voltage drop
Rust	Excessive starts	Design defects	Lack of maintenance	Voltage low
Ventilation	Alignment	Manufacturing defects	Improper maintenance or repairs	Voltage unbalance
Pollution	Resonance of the System		Inappropriate or poor quality parts	Harmonics
Strange Objects	Shaft currents Stator-rotor Friction Partial Discharge(PD)		Lubrication	Defective electrical installation

Table 3. Average cost of faults according to parts of an electric motor

Failure	%
Bearing Related	
Sleeve bearings	16
Antifriction bearings	8
Seals	6
Thrust bearing	5
Oil leakage	3
Other	0.9
Total	41
Stator Related	
Ground insulation	23
Turn insulation	4
Bracing	3
Wedges	1
Frame	1
Core	1
Other	4
Total	37
Rotor Related	
Cage	5
Shaft	2
Core	1
Other	2
Total	10

Taking into account the factors and statistical data that cause the failure of the motors mentioned above, the

development of the algorithm of the monitoring system of their technical condition based on the Soft Computing paradigm is relevant and will be considered in the next research works.

4. Determination of faults related to the main components of the motor based on signal analysis

Determination of bearing-related motor faults based on signal analysis. Bearing failures as statistics show, "bearing" failures in asynchronous motors can cause serious problems, because these failures both reduce the performance of the motor and lead to serious mechanical damage. Signal analysis methods are used to detect bearing failures at an early stage. Below is information about these methods and diagnostic methods.

Types of bearing failures. Wear of the bearing surface - wear caused by friction, causing increased vibrations. Damage to the inner or outer rings - caused by shocks and mechanical pressure. Broken rollers - caused by heavy work or lack of proper lubrication. Lubrication failures - lack of adequate oil increases friction and creates noise in the motor.

Signal analysis methods for cushion fault analysis. Various signal analysis methods are used to determine bearing faults (Table 4).

Vibration analysis. Vibration analysis is one of the most widely used methods for determining bearing failures. Faulty bearings produce unusual vibration frequencies. Analysis in the time domain - increased vibration amplitude and unusual pulses are detected. Harmonic signals are observed at certain frequencies through analysis in the frequency domain - Fourier Transform (FFT). Analysis of defect frequencies - specific characteristic frequencies arise during bearing failures: inner ring defect frequency, outer ring defect frequency, roller transition frequency, rotation frequency.

Noise analysis. During the noise analysis, the sound waves generated as a result of micro cracks or abrasions in the bearing are analyzed. High-frequency sound signals are collected and analyzed through noise sensors. Noise analysis provides sensitive results even in the early stages of faults.

Current signal analysis. Bearing faults cause changes in motor current. Motor Current Signature Analysis (MCSA) - the effect of bearing faults is determined by analyzing the harmonics in the motor current signal. Also, vibration and mechanical pressures cause the appearance of new frequency components in the current spectrum.

Temperature monitoring. As a result of lack of lubrication or mechanical friction, the temperature of the bearing increases. With the help of temperature sensors, temperature changes are monitored and failures are detected at an early stage (Garcia-Perez et al., 2011; Soualhi et al., 2015; Aroui et al., 2007; Thomson & Fenger, 2001).

Table 4. Analysis of bearing failure signals

Failure	Character of signals	Diagnostic method
Inner ring damage	High amplitude harmonics in the frequency spectrum (BPFI)	Vibration and current signal analysis
Outer ring wear	BPFO frequency peaks and high harmonics	FFT analysis
Damage to rollers	BSF peaks in the frequency spectrum	Noise and vibration analysis
Lack of lubrication	Alarms of increased temperature and vibration	Temperature and vibration monitoring

Various measures can be taken to prevent bearing failures. Regular maintenance - regularly check the condition of the bearings and oils. Vibration monitoring system - using sensors to perform continuous vibration analysis. Proper lubrication - proper lubrication materials should be applied to reduce the friction of the bearings. Maintenance of mechanical balance - rotor imbalance can cause bearing failure, so balancing checks must be carried out.

Apparently, bearing failures in induction motors cause both mechanical problems and reduced motor performance. Signal analysis methods, especially vibration and noise analysis, are important for detecting these faults at an early stage.

Determination of stator-related motor faults based on signal analysis. Stator faults in asynchronous motors seriously affect the efficiency and durability of the motor. Problems with the stator windings and insulation can cause phase imbalance, overheating and even burns. Signal analysis methods play an important role in early detection of these faults.

Types of stator faults. Short-circuit in phase windings - short-circuit between windings of the same phase or between different phases. Insulation weakening - the occurrence of electrical leaks due to wear of the insulation material of the windings. Phase unbalance - current differences in different phases bring an uneven load to the motor. Damage from high temperatures - prolonged excessive heat causes melting and damage to bandages.

Signal analysis methods for stator fault analysis. Various signal analysis methods are used to determine stator faults (Table 5).

Motor Current Signal Analysis (MCSA). When a fault occurs in the stator windings, unbalance and harmonic components occur in the phase current. Also, side frequencies appear in the current spectrum. For example, when a winding is short-circuited, additional harmonics appear around the fundamental frequency. The main advantage of such analysis methods is that they allow easy diagnosis without contact. The main components observed in the frequency spectrum during faults: fs - network frequency (for example, 50 Hz); $f_s \pm f_r$ - harmonics depending on the rotor frequency.

Vibration analysis. Failures in the stator windings lead to uneven distribution of the rotor magnetic field and increased vibrations in the motor. Harmonic components in the vibration spectrum are analyzed by FFT (Fourier Transform). Low-frequency vibrations in the motor can indicate winding problems.

Impedance and phase measurement. Impedance differences between phases occur when the phase windings are unbalanced. Based on this, imbalances are determined by analyzing current and voltage phases in different phases.

Temperature monitoring. When the insulation is weakened, the motor overheats. An excessive increase in winding temperature increases the risk of a short circuit in the motor. The wrap temperature is monitored with thermosensors or infrared cameras.

Noise analysis. Micro-short-circuits and faults in the windings produce noise emissions. Noise sensors are placed on the surface of the motor and analyze high-frequency signals.

Table 5. Analysis of stator fault signals

Failure	Character of signals	Diagnostic method
Short circuit in phase winding	Additional harmonics in current spectrum	Unbalanced phases MCSA, Vibration Analysis
Insulation failure	Increased temperature and high frequency noise signals	Temperature and Noise Analysis
Phase unbalance	Current differences between phases	Vibration peaks Current and Vibration Analysis
Overheating of the winding	High temperature and weakening of insulation	Temperature Monitoring

Various measures can be taken to prevent stator faults. *Regular maintenance* - regularly check the insulation condition of the windings. Temperature monitoring - prevent overheating by monitoring the winding temperature. *Phase balance* - ensuring balance between phases and avoiding unbalanced loads. *High-quality insulation materials* - to increase the insulation quality of the windings and use long-lasting materials.

Timely detection and elimination of stator faults of asynchronous motors ensures continuous and reliable operation of the motor. Current signal analysis, vibration analysis, temperature monitoring and noise analysis are effective tools for monitoring motor condition and early detection of potential problems.

Determination of rotor-related motor faults based on signal analysis. The rotor of asynchronous motors is one of the most important parts of the motor and its failures seriously reduce the efficiency of the motor. If rotor faults are not detected in time, they can cause severe mechanical damage or motor shutdown. Signal analysis is

an important diagnostic method to detect rotor faults at an early stage and ensure uninterrupted operation of equipment (Table 6).

Types of rotor faults. *Bar breakage in the rotor cage* - due to the breakage of the bars, the magnetic field becomes weak and uneven. *Locked rotor* - serious mechanical problems occur when the rotor is stuck or does not turn. *Eccentricity* - the location of the rotor outside the center of the stator causes uneven distribution of the magnetic field and vibration. *Rotor distortion and imbalance* - when the rotor is unbalanced, excessive vibration occurs in the motor.

Signal analysis methods for rotor fault analysis. Various signal analysis methods are used to determine rotor faults.

Motor Current Signal Analysis (MCSA). Broken or damaged rotor bars create harmonic components in the motor current. Side frequencies $f_s \pm 2\times f_r$ (harmonics with rotor slip frequency added to mains frequency) are observed. Increased asymmetry and imbalances are determined in the current spectrum during a rotor fault. MCSA allows non-contact rotor fault detection and is particularly effective for cage bar breaks.

Vibration analysis. As a result of rotor imbalance and eccentricity, vibrations in the motor increase. With FFT, harmonics are observed in the vibration spectrum of the rotor rotation frequency. In cases of eccentricity, low-frequency vibration peaks and unusual harmonics appear.

Spectral analysis of rotor faults. Rotor faults produce characteristic harmonics corresponding to the rotation frequency. The main frequencies generated in the spectrum during rotor bar failure are:

$f_s \pm f_r$ - rotor slip frequency, $2\times f_r$ - frequency components corresponding to bar breaks.

Temperature monitoring. As a result of rotor imbalance and mechanical problems, the rotor begins to heat up. The temperature of the rotor is monitored with thermosensors and overheating is detected at an early stage.

Noise analysis. Rotor faults generate noise signals. High-frequency signals are collected and analyzed with the help of noise sensors.

Table 6. Analysis of rotor fault signals

Failure	Character of signals	Diagnostic method
Rotor bar breakage	Harmonics at $f_s \pm 2\times f_r$ in the current spectrum	MCSA (Motor Current Signature Analysis) and vibration analysis
Eccentricity	Harmonics and vibration peaks at rotational frequency	Vibration analysis
Rotor imbalance	High-amplitude vibration and mechanical stress	FFT (Fast Fourier Transform) and temperature monitoring
Mechanical jamming (locking)	Excessive vibration and increased heating	Vibration and temperature analysis

Various measures can be taken to prevent rotor faults: *Rotor balance inspections* - regularly checking the rotor to prevent unbalanced operation of the motor. *Regular vibration analysis* - monitoring vibration levels to detect potential issues at an early stage. *Temperature monitoring* - preventing excessive overheating of the rotor. *Periodic inspection of the rotor cage* - identifying bar breakages at an early stage.

Early detection of rotor faults in asynchronous motors plays a crucial role in enhancing motor reliability and reducing the risk of failures. The signal analysis methods mentioned above are essential tools for monitoring rotor condition and identifying potential problems.

5. Conclusions

Many techniques and methodologies developed for the diagnostic evaluation of electric motors allow for the modelling of potential faults under various motor technical conditions. However, there has been limited research on comprehensive solutions to the investigated faults, which is critical for the development of new motor designs and ensuring uninterrupted operation during their service life.

To enhance traditional diagnostic methods through "soft computing", it is necessary to determine and predict the motor's condition from its equivalent circuit and apply specialized approaches for different types of faults. The development of new modes of transportation further emphasizes the need for reliable operation of electric motors and the timely evaluation of their technical condition under current operating conditions.

The operational challenges of traction asynchronous motors, particularly those used in transportation, increase the probability of faults. Therefore, the methods explored in this study for fault detection through signal analysis can serve as key tools in achieving more precise results when applied comprehensively to traction motors. The research will play an important role in selecting informative parameters for future "intelligent diagnostic systems" for traction motors, contributing to the effective monitoring and maintenance of their performance.

Abbreviations

DFT : Discrete Fourier Transform
DTFT : Discrete Time Fourier Transform
FFT : Fast Fourier Transform
TFR : Time-Frequency Representation
MCSA : Motor Current Signal Analysis
PSD : Power Spectral Density

References

Aroui, T.; Koubaa, Y. & Toumi, A. (2007). Application of feedforward neural network for induction machine rotor faults diagnostics using stator current. *Journal of Electrical Systems*, 3(4), 213–226.

Batista, F., Lamim Filho, P., Pederiva, R. & Silva, V. (2016). An empirical demodulation for electrical fault detection in induction motors. *IEEE Transactions on Instrumentation and Measurement*, 65(3), 559-569. https://doi.org/10.1109/TIM.2015.2509398

Bellini, A.; Filippetti, F.; Tassoni, C. & Capolino, G. (2008). Advances in diagnostic techniques for induction machines. *IEEE Transactions on Industrial Electronics*, 55(12), 4109–4126. https://doi.org/10.1109/TIE.2008.2007527

Boukra, T. & Lebaroud, A. (2010, June 27-30). Classification of induction machine faults *7th International Multi-Conference on Systems, Signals and Devices*. Jordan. IEEE. https://doi.org/10.1109/SSD.2010.5585571

Garcia-Perez, A., Romero-Troncoso, R., Cabal-Yepez, E. & Osornio-Rios, R. (2011). The application of high-resolution spectral analysis for identifying multiple combined faults in induction motors. *IEEE Transactions on Industry Applications*, 58(5), 2002-2010. https://doi.org/10.1109/TIE.2010.2051398

Manafov, E. & Huseynov, F. (2023). Application of artificial neuron networks and fuzzy logic in diagnostic and forecasting the technical condition of traction motors. *Proceedings of the international research, education & training center*, 27(6), 233-239. http://dx.doi.org/10.36962/piretc27062023

Manafov, E., Isgandarov, I. & Huseynov, F. (2022). Investigating the protection system of electric motors based on its main working parameters. *Scientific Journal of Silesian University of Technology. Series Transport*, 115, 63-74. https://doi.org/10.20858/sjsutst.2022.115.5

Merizalde, Y., Hernández-Callejo, L. & Duque-Perez, O. (2017). State of the Art and Trends in the Monitoring, Detection and Diagnosis of Failures in Electric Induction Motors. *Energies*, 10(7), Article 1056. https://doi.org/10.3390/en10071056

Soualhi, A.; Medjaher, K. & Zerhouni, N. (2015). Bearing health monitoring based on Hilbert-Huang transform, support vector machine, and regression. *IEEE Transactions on Instrumentation and Measurement*, 64(1), 52-62. https://doi.org/10.1109/tim.2014.2330494

Stranneby, D. & Walker, W. (2004). *Digital Signal Processing and Applications* (2nd ed.). Elsevier Ltd. https://doi.org/10.1016/B978-0-7506-6344-1.X5000-9

Thomson, W. & Fenger, M. (2001). Current signature analysis to detect induction motor faults. *IEEE Industry Applications Magazine*, 7(4), 26-34. https://doi.org/10.1109/2943.930988

Zhang, P., Du, Y., Habetler, T. & Lu, B. (2011). A survey of condition monitoring and protection methods for medium-voltage induction motors. *IEEE Transactions on Industry Applications*, 47(1), 34-46. https://doi.org/10.1109/TIA.2010.2090839

National Aviation Academy

International Journal of Transportation Research and Technology

e-ISSN: 3079-6075

DOI: 10.71108/transporttech.vm01is01.05

Research Article

Hydrogen Fueled UAV for Wildfire Fighting and Aerial Reconnaissance Coupled with Land Side Hydrogen Mobility

Birol Kilkis*

OSTIM Technical University, Ankara, Türkiye

Timescale of article

Received: 31 August 2024
Accepted: 09 December 2024
Published: 24 December 2024

Corresponding author

Birol Kilkis
birolkilkis@hotmail.com

Keywords

Hydrogen plane, UAV, Forest fire, Reconnaissance, Nearly green hydrogen production, Hovering track vehicle with hydrogen

Cite this article as:

Kilkis, B. (2024). Hydrogen Fueled UAV for Wildfire Fighting and Aerial Reconnaissance Coupled with Land Side Hydrogen Mobility. *International Journal of Transportation Research and Technology*, 1(1), 55-64.
DOI: 10.71108/transporttech.vm01is01.05

Abstract

This paper introduces a new unmanned aerial vehicle system coupled with ground assets, all based on hydrogen fuel, for forest firefighting and rescue missions. A new firefighting index for fire suppression is defined. According to this index, the new system performs about 40% better in terms of heat absorption, range and suppressant to take off weight. The main advantage is that during operational flight the water released from the onboard hydrogen fuel cell supplements the on-board water tank, cooled by an adsorption cycle using the waste heat of the fuel cell. H'g=specific heat hemp nanoparticles also help the heat absorption capacity of water. Oxygen absorption for fuel cells is another attribute. Nearly green hydrogen is produced on the ground base using solar, wind and geothermal energy. The system comprises a mother UAV and several drones, all operating on nearly green hydrogen engines. The mother UAV design incorporates full dedication of AI-based computers for night-time operations and performs risky flight profiles successfully with high-G maneuvers. Mini UAV swarms, mini helicopters and hybrid ground control vehicles complement the fire suppression and rescue missions. Land-side operations are performed by hybrid hydrogen vehicles compromising hovering tracks connected to the air-side operations with a system of systems approach.

1. Introduction

Global warming keeps increasing primarily due to human-induced CO_2 emissions (Kabir et al., 2023). In 2024, global forest fires destroyed or damaged twelve million hectares of forests all over the globe. Consequently, forest fires seem to be one of the reasons why the goals of the Paris Agreement for decarbonization by 2050 will not be achieved on time. Early detection is much more important than fire suppression and limitation. This mission needs satellite imaging but may more effectively be achieved by swarms of UAVs. The latest data on forest fires confirms that they are becoming more widespread, burning at least twice as much tree cover today as they did two decades ago (MacCarthy et al., 2024). Using the University of Maryland data covering the 2001 to 2023 period, the area of forest fires increased by about 5.4% per year. Forest fires are responsible for about six million more hectares of tree cover loss per year than in 2001 (Afshari, 2018). Global warming is the primary cause of forest fires. On the other hand, each acre of forest fire releases about 170-ton equivalent CO_2, comprising methane and nitrous oxide. Trees absorb CO_2 in their body and when burnt, they release them to the environment. On average, twenty-five kg of CO_2 is absorbed by a single mature tree each year (Stancil, 2015). One of the major drivers behind increasing fire activity is dry and high temperatures due to global warming. Each thousand Gton of CO_2 released into the atmosphere causes an increase in the global temperature by 0.45 °C. At the same time, mature forest trees absorb kg of CO_2 annually. This potential is destroyed by each burnt tree. New tree saplings need at least thirty years to attain the same decarbonization potential. Therefore, a seemingly unstoppable vicious cycle between forest fires and global warming exists. This vicious cycle is further accelerated by the fact that warmer air can hold more water vapor. Water vapor is itself a greenhouse gas, which further accelerates the greenhouse effect (EPA, 2024). In this respect, simply relying on water for fire suppression and cooling must be questioned because water vaporizes and mixes with the atmosphere. Therefore, some other means of fire suppression must be sought. Another pressing subject of decision-making is whether ground or air mobility is better for forest fire suppression. When economic concerns are prioritized, land suppression is generally preferred and air suppression is recommended only for the initial stages of fire until the ground assets reach the area (Bushfire CRC & AFAC, 2009). This reasoning is not true because airside assets are effective in all stages of forest fire, provided that they work together with the ground assets.

2. Theory

Recently, UAVs have become familiar with forest fires (Castro et al., 2018). Yet their performance characteristics and effectiveness at many sizes and types are not completely known yet. In this study, a wildfire fighting, rescue and reconnaissance UAV system, which is coupled with landside systems comprising hybrid hovercraft-tracked vehicles, renewable hydrogen production facilities and a control center has been designed. The main objective is to coordinate every step and enhance firefighting with minimum water vapor release. All systems run on nearly green hydrogen. This process is called nearly green because even if onsite solar and wind energy are used, there always occur exergy destructions, which directly translates to nearly avoidable (ΔCO_2) emission responsibilities. Fig. 1 shows this condition for a solar PV, which generates electric power at a modest efficiency, η_{IPV} and rejects the rest of the solar insolation, I_n over the PV cells. This rejection results in local heat island and exergy destruction, E_{Xdes}. The solar PV panel partially replaces demand from thermal power plants, but this replacement is usually less than or equal to the emission responsibility of the solar PV Panel (ΔCO_2).

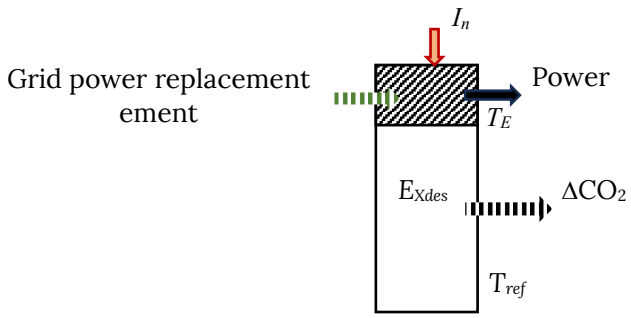

Fig. 1. A solar PV Panel and its ΔCO_2 Emission Responsibility Due to Exergy Destruction, E_{Xdes}

In Eq. 1, the proportionality constant (k) symbolizes the need for offsetting the exergy destruction, E_{Xdes}, by someone, somewhere and by some other means, possibly by using fossil fuels with their exergy destructions, like a boiler.

$$\Delta CO_2 = k \times E_{Xdes} \tag{1}$$

If the major exergy destruction occurs upstream of the useful work obtained, the multiplier (k) is 2.1 kg CO_2/kW-h_{ex}. Otherwise, it is 1.1 kg CO_2/kW-h_{ex}. Another expression for ΔCO_2 is given in Eq. 2, in terms of the Rational Exergy Management Model (REMM) efficiency (ψ_R), which is a measure of exergy imbalance (destruction) between supply and demand. The lower the exergy destruction (better exergy match) is, the higher the (ψ_R) and thus lower the (ΔCO_2). If is above 0.70, the system is 'nearly' green, because the ideal condition (ψ_R = 1) is not possible due to irreversibility.

$$\Delta CO_2 = k \times E_{Xsup} \times (1 - \psi_R) \tag{2}$$

$$\psi_R = 1 - \frac{E_{Xdes}}{E_{Xsup}} \tag{3}$$

Based on commercial solar PV plants in the grid, the formula to determine the limiting ΔCO_2 emission responsibility for one kg of hydrogen gas produced under standardized conditions is given in Eq. 2. The non-zero ΔCO_2 condition shows that completely green hydrogen is not possible, even if all embodiments are ignored. In other words, the definition of nearly-green hydrogen will be practical.

$$\Delta CO_2 \leq k \times \left[\left(1 - \frac{T_{ref}}{T_E}\right) \times \frac{(1-\eta_{IPV})}{\eta_{IT}}\right] \times B > 0 \tag{4}$$

The term (B) is the electrical energy required for electrolysis to generate one kg of hydrogen. According to Antweiler (2020), it is about 40 kW-h_E/kg H_2. With Fig. 1 and Fig. 2., ΔCO_2 can be calculated. T_{ref} is the environment reference temperature, T_E is the temperature of the PV panel frame that loses heat to the environment, η_{IT} represents the transmission losses of the grid. η_{IPV} is the First-Law efficiency of the solar PV panel for electric power generation.

ΔCO_2 = 1.1×[(1-283 K/335 K)×(1-0.2) /0.90] ×40 kW-h_E /kg H_2= 6.07 kg ΔCO_2/kg H_2

From the above calculation, the (η_{IT}) term drops if the PV plant is on site of hydrogen production on the ground side.

Fig. 3. shows the exergy flow bar of hydrogen generation by electrolysis. It is assumed that the waste heat of electrolysis replaces a boiler if that heat is captured and utilized in useful applications like adsorption cooling.

$$\sum_{elect} CO_2 = \Delta CO_{2elect-1} + \Delta CO_{2elect-2} - [CO_2 + \Delta CO]_{boiler} \tag{5}$$

Based on hydrogen energy produced on the land side, the UAV fleet comprises a mother ship (airside command center), firefighting UAV swarms and helicopters, all running on green hydrogen. UAV propulsion and power supply are compared with 1-grid electric UAV, 2-nearly-green grid electric UAV and 3- composite power system UAV, which is presented in this paper.

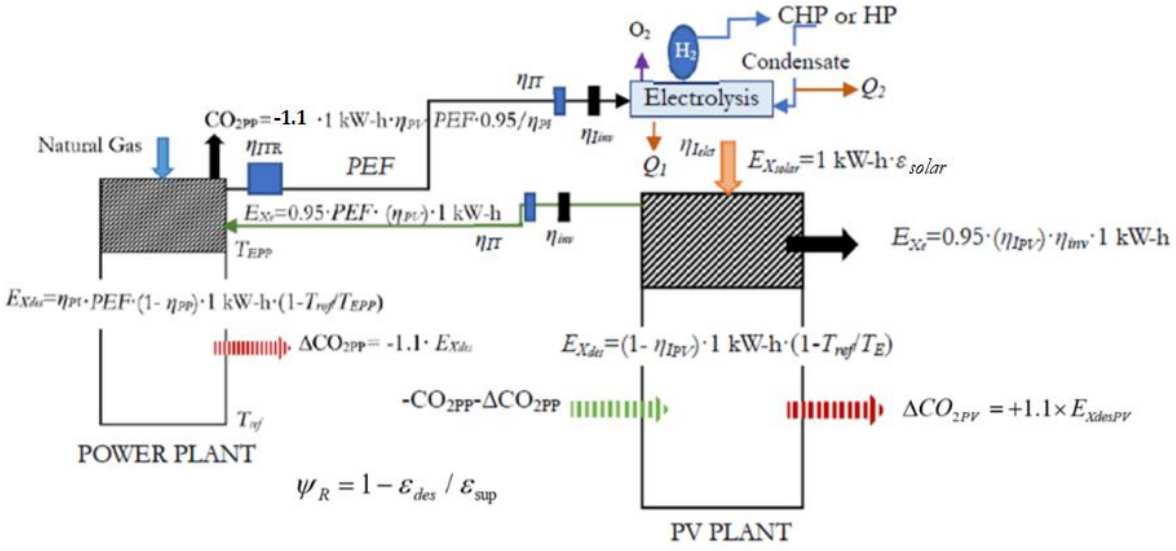

Fig. 2. Emissions Background of Grid-Connected Solar PV Plant and Hydrogen Power Plant

This research has developed a new fire suppression index, *FSI*, for aerial firefighting systems. It involves the range, maximum fire land area that may be covered in one mission, suppressant fill weight to the takeoff weight of the aerial vehicle. The proposed system has an estimated FSI of 60 kW/m of fire suppression capacity. This is about 40% better than other comparable aerial firefighting systems.

$$\text{Fire Supression Index FSI} = \frac{\text{Heat Absorption Rate [kW/m}^3\text{]}}{\left(\frac{1}{\text{Fire Area Covered [m}^2\text{]}} \cdot \frac{\text{Take off Weight}}{\text{Suppressant Weight}}\right)} = 60 \text{ kW/m} \quad (6)$$

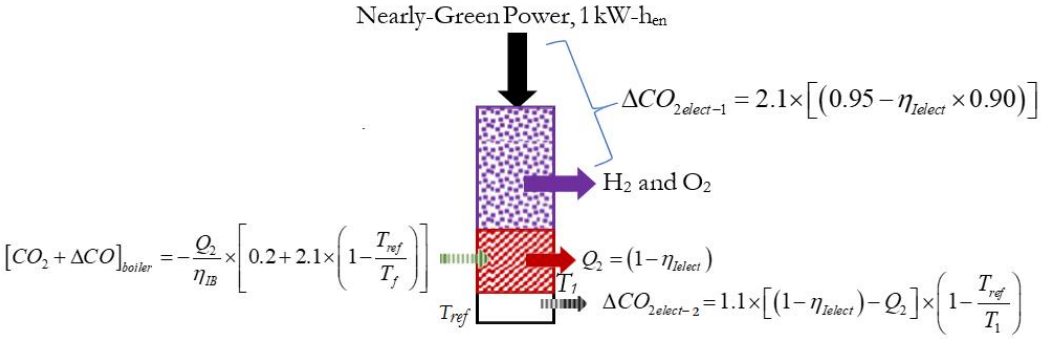

Fig. 3. Exergy Flow Bar and Emissions for Electrolysis

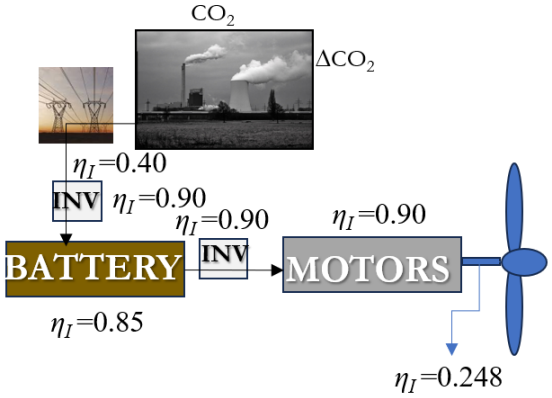

Fig. 4. Fossil Fuel-Grid Electric Driven UAV

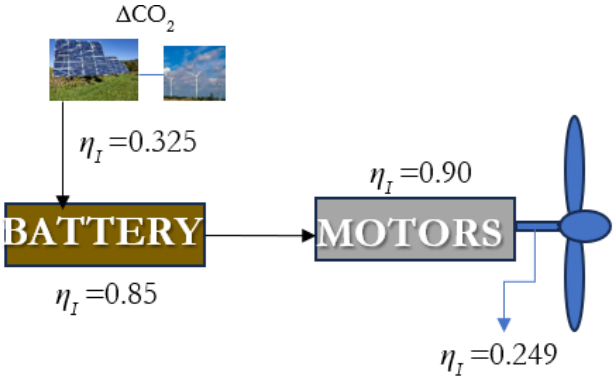

Fig. 5. Nearly Green Grid Electricity UAV

Power plants emit CO_2 as well as ΔCO_2 because they reject the downstream heat (Like in the case of solar PV panels) through the cooling towers, instead of utilizing this thermal power in district energy systems. Depletion of scarce water resources and the greenhouse effect of water vapor are other issues. The overall First Law fuel efficiency from plant to propeller is only 0.248 in this example. In Fig. 5, Power is supplied to the batteries from

renewables in the form of DC power. Onboard batteries deliver DC power to DC motors, this time. The First Law efficiency is not much better, almost the same with Case 1.

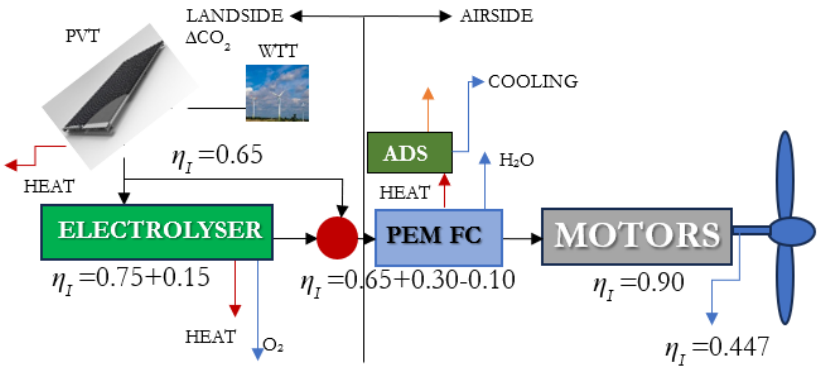

Fig. 6. Alternative 3: Composite Hydrogen Power System UAV

Fig. 6 shows the new hydrogen UAV concept. It consists of two sections. The first section is on the land side where renewable energy systems produce hydrogen gas by water electrolysis and it is stored. The heat and oxygen by-products of this process are used (or stored) for useful purposes on the land side complex. Hydrogen gas in cassette type of tanks is loaded onto the UAV. On the air side (UAV), PEM fuel cells generate power, which drives electric motors. Reject heat of the PEM fuel cell is converted to cold through an onboard adsorption cooling machine to chill the fire extinguishing water tank. The H_20 byproduct supplements the water tank. Thus, the reloading frequency of water from the ground side is reduced giving a better performance. The overall First Law efficiency is higher than the other cases (0.447) and the (ψ_R) value of 0.85 exceeds the limit for green applications but is not equal to one. Case 3 is the best environment-friendly and the best-performing alternative on the drawing board. The remaining task is to optimize the subsystems.

Table 1. Alternative Power Supply Systems to the UAV. kg CO_2 per kW-h electrical energy consumed

Alternative	Overall η_I	ψ_R	CO_2*	ΔCO_2	Total Emissions
1	0.248	0.30	1.3	0.89	2.19
2	0.249	0.45	-	0.40	0.40
3	0.447	0.85	-	0.20	0.20

* Based on a natural-gas combined cycle power plant. Primary Energy Factor (PEF): 2.5.

Table 1 compares the three alternatives in terms of the First Law, the REMM efficiency, ψ_R and CO_2 emission responsibility. See Fig. 4, Fig. 5 and Fig. 6. In Fig. 2, a fossil fuel power plant supplies AC power through the grid. It is inverted to DC through inverters (INV), stored in onboard batteries and then generally re-converted to AC to drive the propellers with electric motors. This table shows that an electric aerial vehicle is responsible for environmental pollution if the power comes from the grid. This responsibility is about six times more than alternative 3 and three times more than alternative 2. It must also be noted that ΔCO_2 even in alternative 3 is greater than zero because of inevitable, irreversible exergy destructions. Following these preliminary results, a compound power supply with green hydrogen UAVs has been designed (Fig. 7).

3. Method

Fig. 7 is a longitudinal cutaway illustration of the mother UAV. This UAV has multiple functions, like air side control of UAV swarms, maintaining the coordination with the land side operations, coordinating with mobile ground control and fire suppression by multiple means, including hydrogen bombing.

The hydrogen UAV receives hydrogen cassettes at the ground station, which generates hydrogen from renewables. All forms of energy are utilized on the land side for hydrogen production. On the UAV, hydrogen is utilized in the PEM fuel cell and electric power and heat are generated, while oxygen in the air is locally consumed (depleting against fire). Water generated in the process is added to the water tank that sprays the water on the fire target. Additives with high specific heat, like hemp, are added in the form of nanoparticles. The water supply from the PEM FC improves the range for firefighting. On the ground, hydrogen-driven mobile units with tracks and air cushions are designed for rescue and onsite monitoring and fire control purposes. See Fig. 8.

This vehicle has deployable skirts such that it can morph into a hovercraft to travel fast over smoother surfaces like plains, lakes, or the sea to harness water, or by folding the skirts up, it may morph into a tracked vehicle over rough terrain and forest land.

One of the important tasks is its early fire detection, personnel transport back and forth, rescue and ambulance missions on the land side. This vehicle can partially generate its own hydrogen supply by raising the propellers mounted on telescopic columns at its stationary position by using the hydro foiling and driving propellers as wind turbines.

Solar PVT systems complement the hydrogen production and heat demand of the vehicle for different purposes. It also absorbs oxygen in the fire area (depletion effect), stores water and delivers it back to the ground station. A compound wildfire detection, fighting, rescue and reconnaissance missions have been designed, based on nearly green hydrogen produced on the land side where the main ground control is built in the potential wildfire areas.

The main control may be decentralized with mobile hydrogen vehicles that can resist wildfires and can be used for close rescue missions. When they are parked in a safe area for near site controls and management, they can also generate green hydrogen. The air side is composed of a mother ship UAV and a swarm of UAVs.

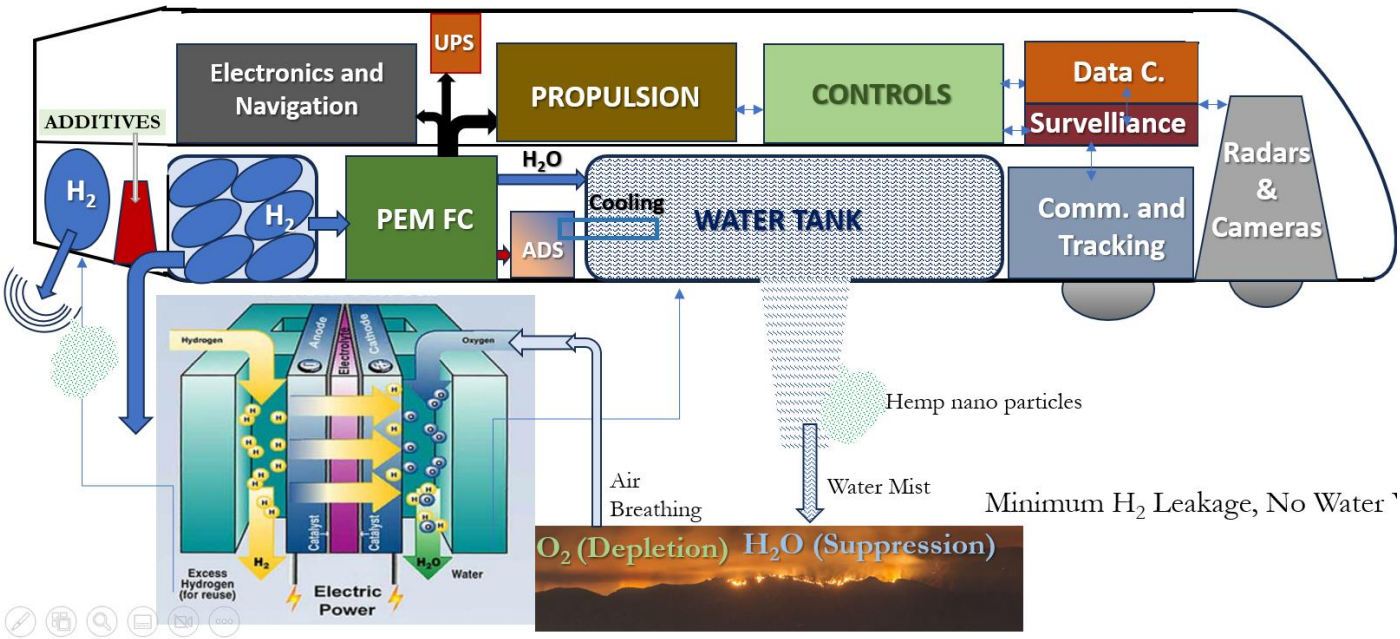

Fig. 7. Air Side of the System: Hydrogen Mothership UAV

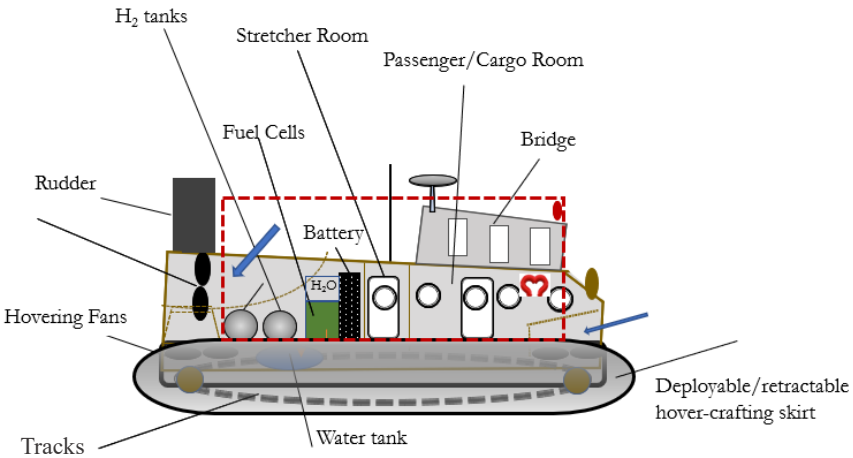

Fig. 8. Ground Side of the System: Hybrid Hydrogen, All Terrain, Amphibious Ground Control, Multitasking Vehicle

4. Results and Discussion

The backbone of the system is the predictive wildfire spread model (Fig. 9), which feeds information simultaneously to the ground control center and the mother UAV on the air side (Kilkis et al., 2021).

This information is dynamically processed and commands are relayed both to ground hydrogen vehicles (Fig. 8) and the swarm UAVs. The Mother ship also functions as the primary aerial fire suppressant (Fig. 7). The concept drawing of the swarm UAV is shown in the upper inset of Fig. 10. These complete the coordination of multiple assets both on the ground side and air side.

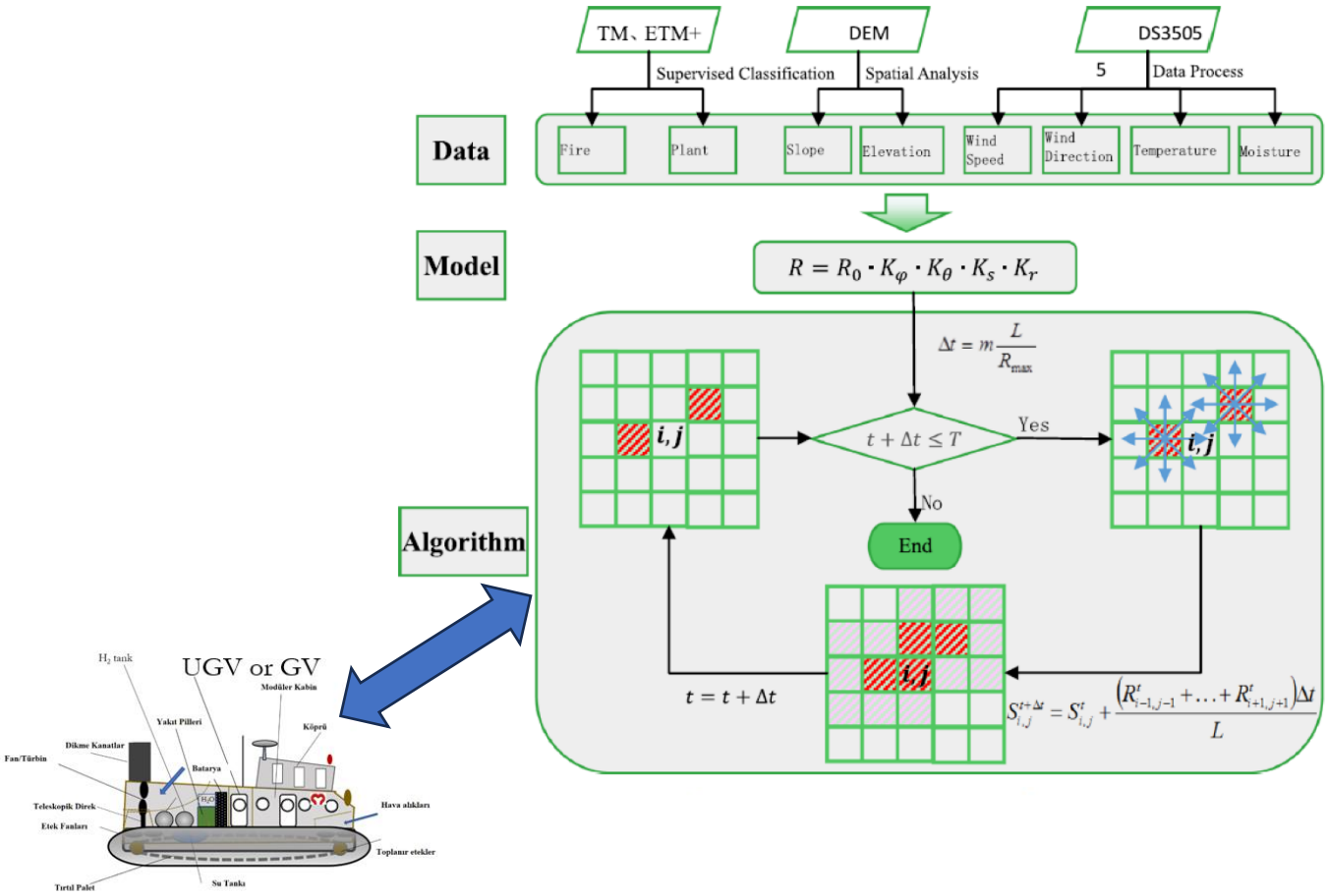

Fig. 9. Overview of Wildfire Spread Model. Mother UAV and Ground Control (Kilkis, 2019; Kilkis et al., 2021; Prakasha et al., 2021)

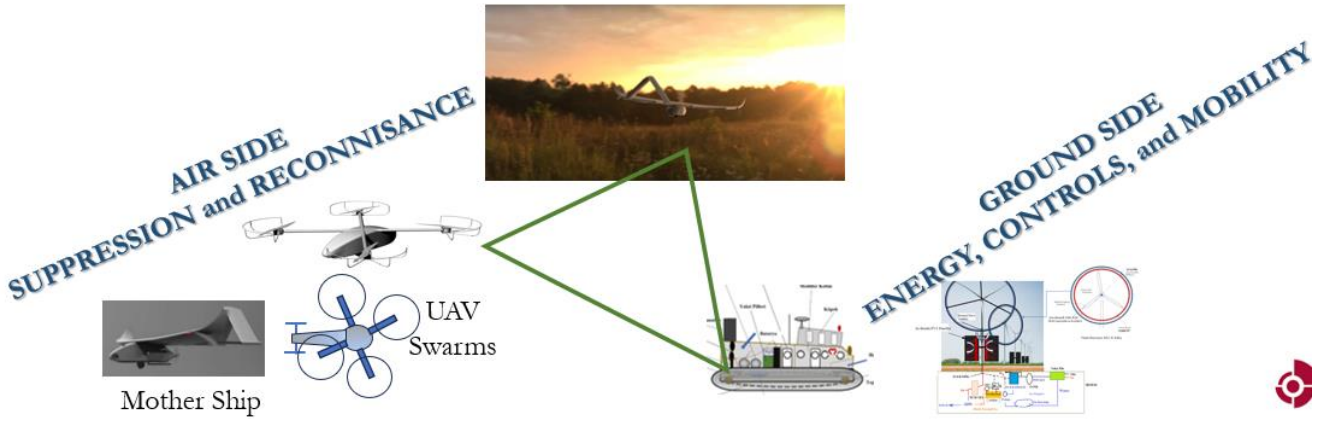

Fig. 10. Compound Firefighting and Rescue Mission Triangle: Coordinated Effort of Multiple Assets

Fig. 10 graphically shows these assets, including novel wind turbines and next-generation solar PVT systems. Usually, global warming-induced forest fires occur in warm and hot climates, which are ideal locations for PVT systems following assets and missions. The following items comprise the primary advantages and functions of these assets:

- Hydrogen UAVs, when fueled by renewables on site, are more energy and exergy-efficient.
- They have longer range and less reloading periods.
- Hydrogen combustion is cleaner than fuel cells but noisier. Therefore, this study replaces hydrogen motors with onboard fuel cells.
- Distributed electric propulsion (DEP) is quieter at take-off and landing but at the cruising flight, it does not help when rescue missions and sonic detection needs most. Therefore, this design relies on double propellers.
- Propeller shrouds are included to reduce noise. Noise is important for landside search and rescue missions.
- How much composites? (Fire susceptibility). This study optimized the use of composites in terms of lightweight versus fire risk (Kilkis et al., 2019).
- Hydrogen on board has multiple functions:
  - Propulsion
  - Fire suppression (with additives still under research)
  - Cooling of suppressant water
  - Acoustic surveillance for rescue. Propellers are at the back, sensors and sophisticated electronics are in the front.
  - Water supply (Extended range, less loading time)
  - Thermal energy is available for ancillaries on board
  - Aerial bombing (last resort)

5. Conclusions

In conclusion, a hybrid, hydrogen-based forest fire fighting and rescue mission has been conceptualized and designed, which is an environment-friendly high-performing integrated system with AI-supported control algorithms. It is expected that this design will contribute to decreasing the damaging effects and monitoring covering all phases starting with the early warning stage to the fire suppression stages. Furthermore, it may give a clue to break the vicious cycle between global warming and forest fires. This system provides minimum hydrogen leakage and no water vapor release. The future work should include detailed design and simulations prior to field tests, targeting an *FSI* of 45.

Abbreviations and Symbols

Latin Symbols

B	: Electrolysis electric power demand, kW-h_E/kg H_2
CO_2	: Direct emission, kg/h or kg/kW-h_{en}
ΔCO_2	: Nearly avoidable CO_2 emission responsibility of a system or process, kg CO_2/kW-h_{ex}
E_X	: Exergy, kW-h_{ex}
E_{Xdes}	: Destroyed exergy, kW-h_{ex}
E_{Xsup}	: Supplied exergy, kW-h_{ex}
FSI	: Fire Supression Index, kW/m
I_n	: Solar insolation, kW/m^2
k	: Unit ΔCO_2 emission factor, kg CO_2/kW-h_{EX}
PEF	: Primary energy factor

Q : Thermal output, kW-h_{en}

T_E : Exit temperature after useful work output, K (See Fig. 1)

T_{ref} : Environment reference temperature, K

Greek Symbols

ε : Unit exergy (According to the Carnot Cycle), kW-h_{ex}/kW-h_{en}

η_I : First Law efficiency

η_{IT} : Grid transmission efficiency

η_{IT} : PV efficiency

η_{IT} : Inverter efficiency

η_{IPP} : Power plant efficiency

ψ_R : REMM Efficiency

Acronyms

ADS : Adsorption Cooling Machine

AI : Artificial Intelligence

CHP : Combined heat and power

DEP : Distributed Electric Propulsion

E, *elect* : Electric (subscript)

EPA : Environmental Protection Agency

FC : Fuel cell

HP : Heat pump

INV : Inverter

PEM : Proton exchange membrane

PV : Solar Photovoltaic Panel

PVT : Solar Photovoltaic-thermal panel

REMM : Rational Exergy Management Model

UAV : Unmanned Aerial Vehicle

WT : Wind Turbine

Subscripts

$_{B,\ boiler}$: Boiler

$_{des}$: Destruction (Exergy)

$_{elect}$: Electric

$_{en}$: Energy

$_{ex}$: Exergy

$_{inv}$: Inverter

$_{pp}$: Power Plant

$_{ref}$: Reference (Temperature)

Acknowledgement

The Author greatly acknowledges the contributions of Şan Kılkış for his diligent work in developing the spatial and functional control algorithm with a novel wildfire spread model for joint operations of land side and air side fire fighting vehicles and equipment.

References

Afshari, R. (2018). *How Much CO_2 is Released When One Hectare of Forest is Burned?* LinkedIn Pulse. https://www.linkedin.com/pulse/how-much-co2-released-when-one-hectare-forest-burned-see-reza-afshari/

Antweiler, W. (2020, September 28). *What Role Does Hydrogen Have in The Future of Electric Mobility?* https://wernerantweiler.ca/blog.php?item=2020-09-28#:~:text=How%20much%20electricity%20is%20needed,kWh%20per%20kg%20of%20hydrogen

Bushfire Cooperative Research Centre (Bushfire CRC) & Australasian Fire and Emergency Service Authorities Council (AFAC). (2009). *Fire Note: Effectiveness and Efficiency of Aerial fire Fighting in Australia*. 50. https://www.afac.com.au/docs/default-source/fire-and-hazard-notes/050.pdf?sfvrsn=12&download=false%3E

Castro, N., Akhloufi, M. A. & Couturier, A. (2018). UAVs for wildland fires. In *conference proceedings of Autonomous Systems: Sensors, Vehicles, Security, and the Internet of Everything*, United States. https://doi.org/10.1117/12.2304834

Environmental Protection Agency (EPA). (2024). *Basics of Climate Change*. https://www.epa.gov/climatechange-science/basics-climate-change#:~:text=Warmer%20air%20holds%20more%20moisture,further%20amplifying%20the%20warming%20effec

Kabir, M., Habiba, Um E., Khan, W., Shah, A., Rahim, S., Rios-Escalante, P. D. L., Farooqi, Z.-U.-R., Ali, L. & Shafiq, M. (2023). Climate change due to increasing concentration of carbon dioxide and its impacts on environment in 21st century; a mini review. *Journal of King Saud University-Science*, 35(5), Article 102693. https://doi.org/10.1016/j.jksus.2023.102693

Kilkis, B., Kilkis, S. & Kilkis, S. (2019). A Simplistic Flight Model for Exergy Embodiment of Composite Materials Towards Nearly-Zero Exergy Aviation. *International Journal of Sustainable Aviation*, 5(1), 19-42. https://doi.org/10.1504/IJSA.2019.099922

Kilkis, San. (2019). *An Investigation into Applying Systems of Systems Methodologies to Aircraft Design*. Guidelines Internship Report (AE 5050). Delft University of Technology.

Kilkis, S., Prakasha, P. S., Naeem, N. & Nagel, B. (2021). A Python Modelling and Simulation Toolkit for Rapid Development of System of Systems Inverse Design (SoSID) Case Studies. *AIAA Aviation 2021 Forum*. https://doi.org/10.2514/6.2021-3000

MacCarthy, J., Richter, J., Tyukavina, S., Waisse, M. & Harris, N. (2024, August 13). *The Latest Data Confirms: Forest Fires Are Getting Worse*. World Resources Institute. https://www.wri.org/insights/global-trends-forest-fires

Prakasha, P. S., Nagel, B., Kilkis, S., Naeem, N. & Ratei, P. (2021). System of Systems Simulation Driven Wildfire Fighting Aircraft Design and Fleet Assessment. *AIAA Aviation 2021 Forum*. https://doi.org/10.2514/6.2021-2455

Stancil, J. M. (2015, March 17). The Power of One Tree-The Very Air We Breathe. *USDA Forest Service*. https://www.usda.gov/about-usda/news/blog/2015/03/17/power-one-tree-very-air-we-breathe

transporttech.org

NATIONAL AVIATION
ACADEMY